Bubble Nucleation in Pulsating Heat Pipes

Blasenentstehung in pulsierenden Wärmerohren

Zur Erlangung des akademischen Grades Doktor-Ingenieur (Dr.-Ing.)
genehmigte Dissertation von Yannick Fabian Frey aus Stuttgart Tag
der Einreichung: 21 April 2024, Tag der Prüfung: 10 July 2024

1. Gutachten: Prof. Dr.-Ing. Peter Stephan
2. Gutachten: Prof. Dr. Marco Marengo
Darmstadt, Technische Universität Darmstadt
Veröffentlichungsjahr der Dissertation auf TUprints: 2024

TECHNISCHE
UNIVERSITÄT
DARMSTADT

Institut für technische
Thermodynamik

Mechanical Engineering
Department

Bubble Nucleation in Pulsating Heat Pipes
Blasenentstehung in pulsierenden Wärmerohren

accepted doctoral thesis by Yannick Fabian Frey

1. Review: Prof. Dr.-Ing. Peter Stephan
2. Review: Prof. Dr. Marco Marengo

Date of submission: 21 April 2024
Date of thesis defense: 10 July 2024

Darmstadt, Technische Universität Darmstadt
Veröffentlichungsjahr der Dissertation auf TUprints: 2024

Bitte zitieren Sie dieses Dokument als:
URN: urn:nbn:de:tuda-tuprints-285990
URL: http://tuprints.ulb.tu-darmstadt.de/id/eprint/28599
DOI: https://doi.org/10.26083/tuprints-000285990

Dieses Dokument wird bereitgestellt von tuprints,
E-Publishing-Service der TU Darmstadt
http://tuprints.ulb.tu-darmstadt.de
tuprints@ulb.tu-darmstadt.de

Dedicated to Katharina Dohn, who always believed in me and supported me.

Erklärungen laut Promotionsordnung

§8 Abs. 1 lit. c PromO

Ich versichere hiermit, dass die elektronische Version meiner Dissertation mit der schriftlichen Version übereinstimmt.

§8 Abs. 1 lit. d PromO

Ich versichere hiermit, dass zu einem vorherigen Zeitpunkt noch keine Promotion versucht wurde. In diesem Fall sind nähere Angaben über Zeitpunkt, Hochschule, Dissertationsthema und Ergebnis dieses Versuchs mitzuteilen.

§9 Abs. 1 PromO

Ich versichere hiermit, dass die vorliegende Dissertation selbstständig und nur unter Verwendung der angegebenen Quellen verfasst wurde.

§9 Abs. 2 PromO

Die Arbeit hat bisher noch nicht zu Prüfungszwecken gedient.

Darmstadt, 21 April 2024

Y. Frey

Acknowledgments

I would like to express my sincere gratitude to my professor and doctoral supervisor Prof. Dr.-Ing. Peter Stephan for his guidance and support! Also big thanks to Prof. Dr. Marco Marengo for serving as a second examiner. This journey would not have been possible without Dr. Marco Lorenz and Dr. Aaron Dörr, who supported me with countless discussions, critical advice, and uplifting words when needed! Special thanks also to Moritz Klingert for his support with measurements! I also wish to thank the many colleagues who took time for valuable technical discussions and moral support. Big thanks to Robert Bosch GmbH for funding my work! My appreciation goes out to my family for their encouragement and belief in me! Lastly, I would like to thank Katharina Dohn for her tremendous understanding and uplifting, and for accepting the many working hours in the last few years!

Abstract

In dieser Arbeit werden experimentelle und numerische Untersuchungen präsentiert, die weiterführende Einblicke in die Funktionsweise eines pulsierenden Wärmerohrs gewähren. Der Schwerpunkt liegt dabei auf dem Zusammenhang zwischen der für Nukleation notwendigen Wandüberhitzung und dem thermischen Widerstand. Daher wurden drei transparente, geometrisch identische, Versuchsaufbauten angefertigt, die sich lediglich durch deren Oberflächenrauigkeit im Verdampferbereich unterscheiden. Diese wurden durch Fräsen sowie Sand- und Glasperlenstrahlen hergestellt. Um die thermische Performance bewerten zu können, wurde der thermische Widerstand zwischen Verdampfer und Kondensator des pulsierenden Wärmerohrs mit R1233zd(E) als Kältemittel gemessen. Geringer Flüssigfüllstand, hohe Wärmeströme, Fluidtemperatur und Oberflächenrauigkeit verringerten dabei den thermischen Widerstand. Der Einfluss der Oberflächenrauigkeit war besonders signifikant bei kleinen Wärmeströmen. Die Oberflächenstruktur im Verdampferbereich wurde durch Aufnahmen mit einem Konfokal-Mikroskop sowie eines neuartigen Auswertealgorithmus charakterisiert, dadurch konnten Blasenradienverteilungen (Kavitätsgrößenverteilungen) aus den Aufnahmen abgeleitet werden. Auf dieser Basis konnten mittlere notwendige Wandüberhitzungen für das Blasensieden für jeden aufgezeichneten Messpunkt anhand der Siedeverzugsgleichung bestimmt werden. Eine neu eingeführte Größe, die relative Nukleationshürde (RNT), konnte somit bestimmt werden. Sie stellt den Quotienten der theoretisch notwendigen Wandüberhitzung zur Temperaturdifferenz dar, die aufgrund von Wärmeleitung in einem inaktiven pulsierenden Wärmerohr verfügbar ist. Es konnte gezeigt werden, dass der thermische Widerstand des pulsierenden Wärmerohrs direkt mit RNT korreliert. Die Korrelation ist für unterschiedliche Wärmeströme, Fluidtemperaturen und Verdampferrauigkeiten gültig. Die Koeffizienten der Korrelation hängen von dem Flüssigfüllstand des pulsierenden Wärmerohrs ab.

Mithilfe einer Hochgeschwindigkeitskamera konnten Aufnahmen der Fluidströmung in den Kanälen des Verdampferbereichs aufgezeichnet werden. In Kombination mit einem neuartigen Blasendetektions- und Tracking-Algorithmus konnten somit mittlere Blasenentstehungsraten (Anzahl neu entstandener Blasen pro Sekunde) im Verdampferbereich

in den untersuchten Zeitintervallen bestimmt werden. Bei einem Flüssigkeitsfüllstand von 70% wurde ein Zusammenhang zwischen der Blasenentstehungsrate und RNT entdeckt. Die maximale Blasenentstehungsrate tritt bei RNT=0,3 auf. Für große RNT-Werte oder gegen RNT=0 nähert sich die Blasenentstehungsrate null an. Für RNT>0,3 lässt sich dieser Trend dadurch erklären, dass ein höherer RNT-Wert zu einer geringeren Wahrscheinlichkeit für Blasenbildung und damit zu einer niedrigeren Blasenentstehungsrate führt. In den experimentellen Untersuchungen konnte jedoch nicht quantitativ bestimmt werden, wie der Abfall der Blasenentstehungsrate gegen RNT=0 zu erklären ist. Beobachtungen des Strömungsverhaltens legen jedoch nahe, dass sich für niedrige RNT-Werte weniger Flüssigphase im Verdampfer befindet. Da Blasen nur entstehen können, wenn Flüssigphase im Verdampfer vorhanden ist, entstehen hier weniger Blasen, obwohl RNT reduziert wird.

Um weitere Einblicke in das Verhalten eines pulsierenden Wärmerohrs zu bekommen, wurden daraufhin 1D-Simulationen durchgeführt. Um ein korrektes physikalisches Verständnis anhand der Simulationen ableiten zu können, mussten diese zunächst mittels Versuchsdaten im entsprechenden Parameterbereich validiert werden. Daher wurden die Randbedingungen aus den durchgeführten Versuchen in den Simulationen rekonstruiert. Die Simulation zeigte dabei für 70% Flüssigkeitsfüllstand ausreichend genaue Ergebnisse für den thermischen Widerstand bei Variationen des Wärmestroms, der Fluidtemperatur und der Oberflächenrauigkeit. Andere Füllstände lieferten jedoch keine ausreichende Genauigkeit in der Simulation, daher wurden für die weiterführende Analyse der Simulationsergebnisse nur Berechnungen bei 70% Füllstand verwendet. Anhand der Simulationsdaten konnte aufgezeigt werden, dass die Wärmeübergangskoeffizienten zwischen der Kanalwand und dem Fluid, die Oszillationsfrequenz der Strömung, sowie der Anteil an Flüssigphase im Verdampferbereich von RNT abhängen. Dies stärkt die Plausibilität der experimentell ermittelten Korrelation. Unter der Annahme, dass Blasen nur entstehen können, wenn Flüssigphase im Verdampfer vorhanden ist, konnten die simulativ ermittelten Flüssigphasenanteile im Verdampfer genutzt werden, um die Blasenentstehungsraten in den Versuchen quantitativ zu erklären.

Zusammenfassend konnte gezeigt werden, dass die für das Blasensieden notwendige Wandüberhitzung einen großen Einfluss auf die Leistung eines pulsierenden Wärmerohrs hat. Um die Korrelation auch für verschiedene Kanalgeometrien nutzen zu können, wurde sie anhand von Simulationsdaten empirisch erweitert, sodass der Auslegungsprozess für ein pulsierendes Wärmerohr vereinfacht werden kann. Dazu wurden Simulationen bei unterschiedlichen Verdampferlängen und unterschiedlicher Anzahl an Kanälen durchgeführt. Anhand der Gesamtkanallänge im Verdampferbereich wurde eine modifizierte Korrelation eingeführt.

Abstract

In this work, experimental, and numerical investigations are presented that aim to allow further insights into the operational mechanisms of pulsating heat pipes. The focus is on the link between necessary wall superheat for bubble nucleation and thermal resistance. Therefore, three transparent experimental setups were manufactured for testing that were geometrically identical but had different evaporator roughness manufactured by milling, sand blasting, and glass bead blasting techniques. The overall thermal resistance between evaporator and condenser was measured with R1233zd(E) as a working fluid and used for the evaluation of thermal performance. The results showed that decreasing filling ratio, increasing heat flow, operating temperature, and evaporator roughness influenced the thermal resistance beneficially. The influence of surface roughness was most pronounced for low heat flow. From confocal measurements of the evaporator surface structure and a newly introduced evaluation algorithm, bubble radius (cavity size) distribution profiles could be estimated for each surface structure. This allowed to apply the pool boiling nucleation equation to calculate theoretical required wall superheats for nucleation for each data point of the measurements. Based on the results, a relative nucleation threshold (RNT) was introduced that represents the quotient of theoretical required wall superheat for nucleation to the temperature difference from evaporator to condenser available due to thermal conduction in an inactive PHP. It was found that the thermal resistance of the PHP correlates directly with RNT, and that the correlation is valid for multiple heat flow, surface roughness values, and operating temperatures. The coefficients of the correlation depended on the filling ratio.

Using a high-speed camera, the flow inside the channels of the evaporator section was recorded. In combination with an optical bubble detection and motion tracking algorithm, average bubble nucleation rates (number of bubble generations per second) in the evaporator area for the analyzed time intervals were derived. The data at 70% filling ratio showed a connection between RNT and the bubble nucleation rate. The maximum bubble nucleation rate was located at an RNT value of 0.3. At RNT close to zero and high values of RNT, the bubble nucleation rate was approaching zero. For RNT$>$0.3, the behavior could be explained as higher RNT values lead to a lower probability of bubble

nucleation and, thus, a reduced bubble nucleation rate. The decrease in nucleation rate from RNT 0.3 to RNT zero could not be quantitatively explained by the experiments. Flow observations suggested that low values of RNT cause a decrease of liquid mass in the evaporator. As bubbles can only be nucleated if liquid is present, the bubble nucleation rate is decreased here, even though RNT is also reduced.

Subsequently, 1D-simulations of the PHP were conducted to gain further insights. To obtain correct physical understanding of PHP function from the simulations, they had to first be validated in the intended parameter range. Consequently, the experimental setups were reconstructed in the simulations. It could be shown that the simulation yielded accurate thermal resistances at 70% filling ratio and various condenser temperatures, heat flow, and surface roughness values. However, at lower filling ratios the simulation did not produce accurate results. Therefore, only simulations at 70% filling ratio were further analyzed. It could be shown that heat transfer coefficients between the fluid and the channel walls, the flow oscillation frequencies, and the liquid mass fractions inside the evaporator area correlated directly with RNT, strengthening the plausibility of the correlation found in the experiments. By presuming that bubbles can only be nucleated, if liquid is present within the evaporator, the liquid mass fractions found in the simulations allowed to quantitatively explain the bubble nucleation rates in the experiments.

Compendiously, it could be shown that the required wall superheat for nucleation has a major influence on the PHP performance. To allow for the use of the correlation with different channel geometries, the correlation was empirically extended by further simulation data to provide a feasible PHP design tool. For this, simulations with various numbers of channels and evaporator lengths were conducted and a modified version of the correlation was introduced, accounting for the total channel length within the evaporator area.

Contents

1 Introduction

Due to rapid advancement in the fields of automotive electrification, autonomous driving, IoT etc., cooling of electronics becomes increasingly important. In the field of computer electronics, miniaturization of chips is an ongoing process. According to Intel [1], the number of transistors on a chip doubles every 18 months, leading to a doubled power dissipation every 36 months. The automotive industry is shifting inexorably from combustion engine to electric drives, mostly powered by batteries [2]. The inverter in the electric drive train is one of the key components with very high demands for effective cooling. As the cost for semiconductor surface area highly influences the overall cost of an inverter, chip size is reduced to a minimum [3]. With constant demand of electric power, this leads to higher heat flux densities in the chips for automotive inverters as well as many other electronics [4, 5].

Conventional cooling methods such as natural or forced convection cooling, that were so far often used for electronics, reach their limitations with current cooling demands [4, 5]. Even if technically possible, simple forced convection cooling would result in very high fan power and, thus, high energy effort for cooling. While striving for higher overall efficiency, the need for low energy consumption in cooling also becomes increasingly important [5]. Wherever low energy consumption, improved acoustics, or effective heat transportation are necessary, passive two-phase cooling devices should be considered as heat spreaders [6].

Several main types of passive two-phase cooling systems are known from literature and industry. Among the most prominent is the heat pipe. Heat pipes are typically made of copper (and sometimes aluminum) tubes with grooves, wicks, or a porous structure on the inside wall. Figure 1.1 shows the working principle of a heat pipe. The pipe is filled with a working fluid (often water) and sealed hermetically. On the hot side, working fluid evaporates and vapor travels through the pipe to the cold side. Here, condensation takes place and the liquid fluid is transported back to the hot side by capillary forces in the wick [7].

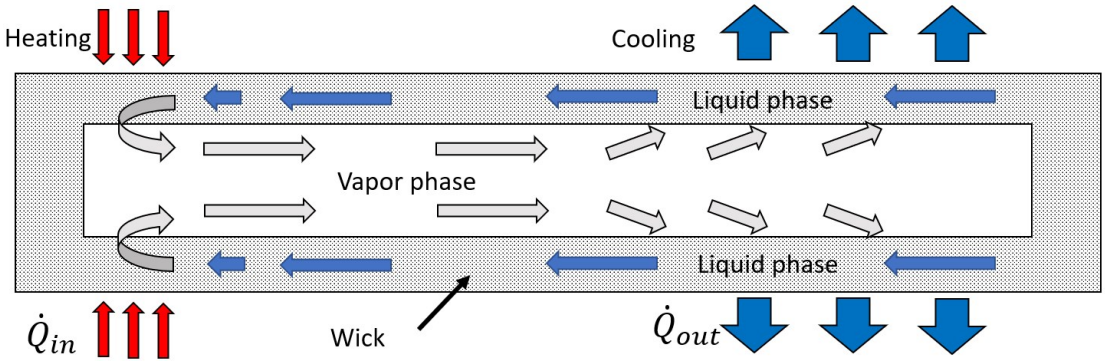

Figure 1.1: Functional principle of a heat pipe

Vapor chambers are similar in function to heat pipes, but the setup is flat rather than circular. They typically also have a wick structure. From a small fraction of the surface, where the heat source is located, evaporation takes place and the vapor spreads across the full surface of the device. Condensation at the cold sections of the surface and transport through capillary forces back to the heated section close the circle. Vapor chambers are typically used as a heat spreader from a small to a very large area in the same plane [8].

In a two-phase thermosiphon the device is set up vertically with the evaporator located below the condenser section. Figure 1.2 shows the schematic setup. Evaporation generates vapor at the heated bottom which rises to the cold condenser section above. When fluid condenses at the top, gravitational force pulls the liquid phase back down to the evaporator section. Therefore, no wick structure is needed [9].

Two-phase devices mainly differ from each other by their method of liquid transportation from the condenser to the evaporator zone. While heat pipes and vapor chambers use capillary forces, a thermosiphon uses gravitational force. The ”Two Phase Thermal Solution Guide” published by Boyd [6] recommends the use of heat pipes mainly for transport of heat for long distances and if the integration of multiple heat pipes does not impose a problem. Vapor chambers are advised to be used mainly for heat spreading and thermosiphons if the gravitational orientation of the cooling solution is fixed in the vertical bottom-heated orientation.

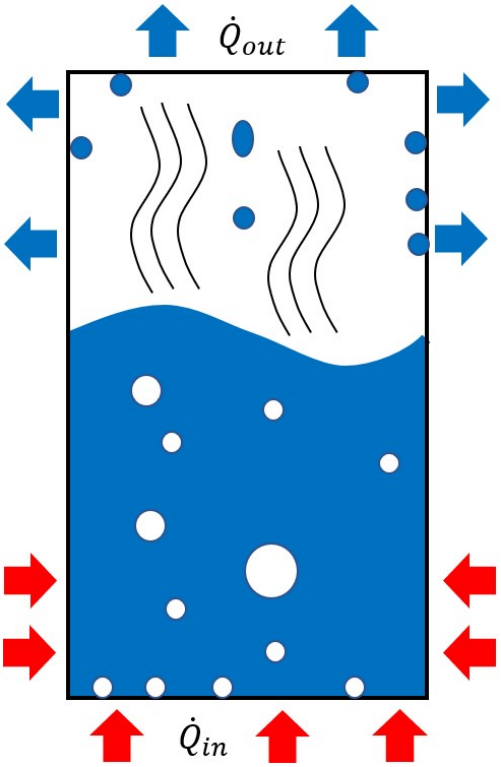

Figure 1.2: Functional principle of a thermosiphon

Pulsating Heat Pipes (PHP are rather new two-phase cooling devices that use pressure gradients induced by evaporation and condensation for maintaining a self-sustained oscillating flow within capillary tubes (figure 1.3. As the transport of liquid phase to the evaporator occurs due to pressure gradients, no wick structure and in most cases no gravitational force are needed. This leads to many advantages of PHPs compared to competing technologies. Firstly, the lack of wick structure is an advantage in manufacturing and enables cost effective solutions. Additionally, the meandering channel structure can easily be integrated into applications and offers high flexibility in design. For example, the number of channels can be adapted to fit the size of the application [10]. PHPs also allow to effectively cover long distances and large areas. Next to copper, multiple construction materials can be used as a wall material in PHPs. Aluminum is a prime candidate due to its low density, high thermal conductivity, and low price [5].

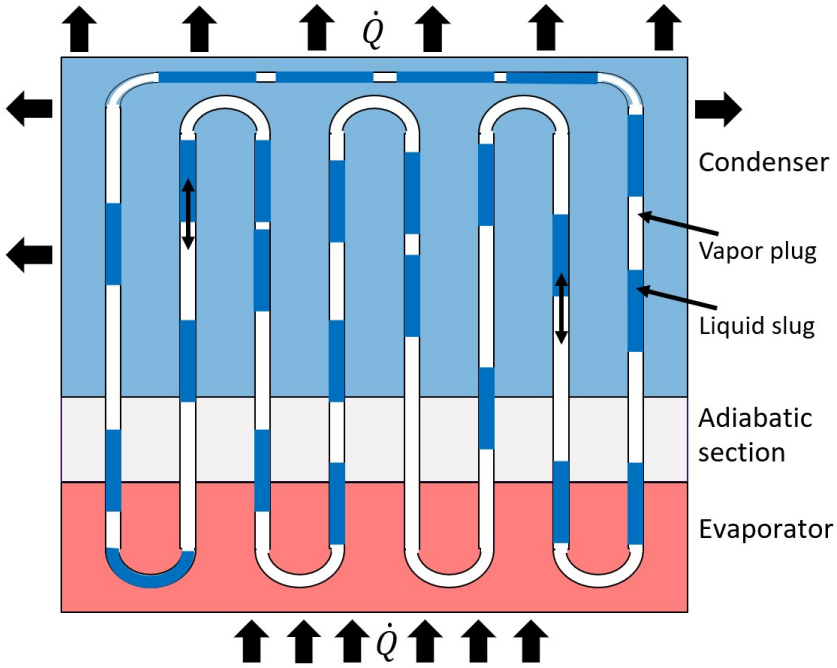

Figure 1.3: Functional principle of a pulsating heat pipe

Despite a lot of ongoing research, the working principle of a PHP is not yet fully understood and more research on the thermo-hydraulic coupling is necessary to fully exploit their technological opportunities and potential for improvement [5]. Consequently, this work aims to enlarge the fundamental understanding of the phenomena relevant for PHP operation. In an experimental approach, important influencing factors were identified. As the surface structure of the channel walls has been mostly neglected in previous research, a focus point is on the influence of the wall roughness on the flow regime and thermal performance of a PHP. A correlation was found that links the thermal performance of a PHP to the bubble nucleation threshold. A numerical study is conducted, aiming to create additional insights on the importance of bubble nucleation threshold in a PHP.

2 Literature review

This chapter summarizes the current status of research in the field of pulsating heat pipes from published literature. Next to the functional principle (section 2.1), the operational aspects (section 2.2) are explained. This includes geometrical and operational influencing parameters on pulsating heat pipe behavior. As this work intends to generate more understanding of PHP operation, the current modelling and simulation approaches are also presented (section 2.3).

2.1 Functional principle of pulsating heat pipes

Pulsating heat pipes usually consist of a meandering channel, as can be seen in figure 1.3. The channel alternates between the cold side where the heat is removed from the fluid (condenser) and the hot side where heat is transferred to the fluid (evaporator). In between the two, an adiabatic section may be present where no heat transfer to the surroundings occurs. In a closed-loop pulsating heat pipe as depicted in figure 1.3, the outer channels located at the left and right edge of the setup are connected. In an open-loop PHP this connection does not exist. However, most research [11] indicates that closed-loop PHPs exhibit better thermal performance. Therefore, this work focusses on closed-loop PHPs.

Firstly, the channel of the PHP is evacuated and, subsequently, filled with a working fluid. The channel is partially filled with liquid phase and the remaining volume is filled with vapor phase of the same working fluid. The volumetric ratio of liquid phase to the full channel volume is called filling ratio (FR). Heat flow to the evaporator increases the evaporator wall temperature. At a certain temperature difference between condenser and evaporator, local evaporation occurs in one or multiple channel sections located within the evaporator section. This causes local pressure increase and, consequently, a pressure gradient along the channel. The pressure gradient drives the liquid slugs and causes them to move along the channel. Vapor entering the condenser section starts to condense, which results in local pressure decrease, also causing pressure gradients in the channel. Overall,

the pressure gradients lead to an oscillating motion of the vapor bubbles and liquid slugs.

For a closed-loop PHP, the oscillating motion can be superimposed by a circulating motion [11]. Generally, the oscillation frequency increases with increasing heat flow [12]. The motion of the liquid slugs also causes liquid convection and, thus, heat transfer between the tube walls and the liquid slugs. This way, sensible heat is transported in the PHP next to the latent heat transported by the evaporation and condensation of vapor plugs [13].

The meandering channel can be created in multiple ways. Based on prior publications, two main design variants are known so far: The first option is to bend a tube back and forth and to connect the ends [14, 4]. The second option is to mill the channel layout into a flat metal plate, typically copper or aluminum. The milled channel plate is closed by attaching a cover plate [4, 15].

Because of the structural advantages of a PHP compared to other two-phase cooling solutions, it can be used in multiple applications. Lu and Li [16] successfully investigated a PHP for rack cooling in an IT system. Abad [17] described the effective use of a PHP in a thermal desalination system. Various other applications can be found, where a PHP was used in a heat exchanger [18, 19]. Alizadeh [20] numerically studied the use of a PHP for cooling of photovoltaic cells while Roslan and Hassim [21] proved the effective use of a PHP in photovoltaic cells in a real-life environment. The technology can further be used for cooling LEDs [5] and for thermal management of batteries in electric vehicles [22]. Mito et al. [23] even proved that PHPs can be used in extremely low temperature applications. PHPs in cryogenic applications use hydrogen, neon, or nitrogen as working fluids and operate in a temperature range of 18 to 84 K.

2.2 Operational aspects

One of the primary design variables of a PHP is the channel's hydraulic diameter. According to Qu et al. [24] the diameter D of a PHP should be in the range of

$$0.7\sqrt{\frac{\sigma}{g(\rho_{liq}-\rho_{vap})}} \leq D \leq 2\sqrt{\frac{\sigma}{g(\rho_{liq}-\rho_{vap})}}, \tag{2.1}$$

where σ and ρ_{liq} are the surface tension and the density of the liquid phase, respectively. g is the gravitational acceleration and ρ_{vap} is the saturated vapor density. Larger diameters typically enhance the thermal performance of a PHP due to lower dissipation losses [25]. The shape of the channel's cross section also influences the PHP behavior. From publications, mainly circular or rectangular cross sections are known. Square channels exhibit improved liquid transportation in the corners due to capillary forces and, thus,

enhanced evaporation in PHPs. However, it can also be observed that square channels are more prone to dry-out in horizontal PHPs [4]. Dryout is a condition where the slug-plug flow that is necessary for PHP operation is stopped and the entire evaporator fills with vapor. In this condition, the PHP ceases to operate [26].

Researchers [5] currently agree that the number of turns of a PHP impacts the maximum heat flow it can handle and its thermal performance. A high number of turns allows for better operation in orientations other than vertical with the evaporator at the bottom. Research [10] indicates that there exists a critical number of turns over which a PHP can operate independently of orientation with consistent thermal performance. However, the value of this critical number of turns is still under discussion. Several other parameters could influence the threshold for orientation independent operation. In addition to the number of turns, other parameters of the channel layout also seem to influence the thermal performance. Among them are the lengths of the evaporator, adiabatic, and condenser section [5].

Next to the channel layout itself, the filling ratio (defined as the volumetric fraction of liquid phase within the channel) also influences the thermal performance. Low filling ratio is typically more prone to dry-out as not enough liquid is pumped through the evaporator. High filling ratios reduce the amount of vapor present in the PHP, limiting the pumping effect as less compressible fluid is present. Most setups allow for oscillations in a range between 20% and 80% filling ratio. Typically, an intermediate filling ratio can be found with an optimal thermal performance. The optimal filling ratio depends on many parameters and is different for each setup [11].

The orientation of a PHP to gravity additionally influences the thermal performance. For most PHPs, the optimal orientation is vertical with the evaporator located at the bottom. In this case, gravity assists the return of liquid phase to the evaporator and, therefore, enhances the oscillating motion [10]. Lowering the inclination angle towards a horizontal position or even vertical top-heated orientation usually deteriorates the thermal behavior. However, this effect is not fully understood yet. Some research indicates that a specific optimal inclination angle can be found that depends on the operational temperature [27]. For PHPs with a high number of turns, the orientation does not seem to influence the thermal performance [11].

The heat flow in the evaporator section enables evaporation and is, therefore, the source of the oscillating motion of the fluid. Consequently, a minimum heat flow is required for a PHP to operate. If the minimum heat flow is exceeded, a further increase in heat flow typically leads to a decrease in thermal resistance [28, 10]. Researchers so far assume that the amount of sensible heat transported is low for low heat flow rates. The ratio of sensible heat increases with increasing heat flow [11, 10]. The increase in sensible heat transported is due to an increased flow velocity at higher heat flow [29].

The choice of working fluid is crucial for a PHP. Several properties of the working fluid affect the PHP performance. High viscosity increases the frictional losses of the flow and leads to higher thermal resistance. High surface tension stabilizes the slug-plug flow regime and, therefore, allows for the use of larger channel diameters. This is especially valuable in horizontal or vertical top-heated orientation. High specific heat capacity enhances the transport of sensible heat and is, therefore, favorable [11]. Low latent heat of vaporization enables easy evaporation, especially at low heat input. The oscillating motion is, therefore, enhanced and the thermal resistance lower. For high heat loads, a higher latent heat of vaporization tends to improve the thermal resistance as more latent heat can be transported. Higher thermal conductivity of a fluid also seems to be favorable [30].

Fluid properties depend on the fluid's temperature. Therefore, a change in the temperature level affects a PHP's performance. Kim et al. [31] have shown that higher fluid temperatures lead to an improved PHP performance within the temperature range and for the fluids investigated in their study. They attributed the changes to a change in the gradient dp/dT of the vapor pressure curve. A steeper vapor pressure curve generates more pressure difference for a given temperature increase and, therefore, offers greater stimulation of the oscillating motion. Early research in the field of PHPs usually focused on water, ethanol, acetone, and methanol as working fluids. More recently, several refrigerants were investigated [5]. Among them are R134a, R600a [32, 33], R245fa [34], and FC-72 [35]. Several researchers investigated the effects of nano-fluids [36], self-rewetting fluids [37], and surfactants [38] on the thermal behavior of a PHP.

Multiple techniques were investigated to enhance the performance of a PHP. Betancur et al. [39] tested the effect of alternating superhydrophobic and hydrophilic channels. However, the enhancement method proved to be unsuccessful. Tseng et al. [40] used varying channel diameters to differ the flow resistance of neighboring channels. This proved to enhance the thermal resistance and led to improved start-up. Ebrahimi et al. [15] studied interconnecting channels between two neighboring channels. The interconnections were placed at an angle that favored the flow in one direction and hindered the flow in the other direction. Therefore, a circulating flow was fostered. The interconnections showed to improve the thermal performance. Thompson [41] utilized a check valve to promote circulatory flow and, thus, was able to reduce the thermal resistance of a PHP. Different manifold configurations of the flow returns were investigated by Agostini [42].

2.3 Simulation approaches

The intensified research in the field of PHPs is due to its high potential for various applications. However, to successfully design PHPs for products within reasonable time, a reliable prediction method for PHP performance is a prerequisite, as it can speed up the design iterations considerably. Several works were published where multi-dimensional simulations were attempted for PHPs. Pouryoussefi and Zhang [43] modelled a 2-bend PHP with a 2D mesh in Ansys. Similar to other investigations, they used the Volume of Fluid (VoF) method. Pachghare and Mahalle [44] conducted a 3D simulation in Star CCM+ and Vo et al. [45] in Ansys Fluent. Both used VoF and simulated only a single loop of a PHP. They each compared their results with experimental data and found good agreement.

3D-CFD simulations of PHPs have several advantages. Primarily, they can cover multiple flow regimes (for example, annular flow next to slug-plug flow). Therefore, they can be very useful in understanding the working principle of a PHP. Though ultimately successful in some cases, multi-dimensional simulations of PHPs are very time consuming and come at a high computational effort, often to only compute a small fraction of the full channel length. Due to their transient nature, high flow velocities, and long channels, PHPs require large meshes and very small time steps, combined with a long simulation time. Therefore, multi-dimensional simulations cannot be easily used in a design process and much less in an optimization process of PHPs [46, 13].

To obtain simulation results at low computational effort, simpler mathematical models were introduced such as the models by Peng and Hongbin [47] or Yoon and Kim [48]. By using a 1D-grid with only one cell across the channel diameter, several 1D-modeling approaches were introduced. One example is the model proposed by Nikolayev [49]. Nikolayev assumed the liquid film thickness of a Taylor bubble to be constant. He applied a film evaporation and condensation (FEC) model that allows for sections of a Taylor bubble to dry-out during evaporation and other sections of the same bubble to still comprise a liquid film of a predefined thickness.

1D-models were consequently improved by accounting for more physical effects or improving the modelling of single phenomena. As of today, the state-of-the-art 1D modelling approach for PHPs comprises the Three-Zone-Model introduced by D'Entremont and Thome [50]. The model separates the channel in three different zones: liquid slug, elongated bubble with liquid film, and dry region without a liquid film. Several physical key effects must be considered:

Liquid slugs deposit a liquid film on the tube walls at their trailing edge. The initial thickness of the film can be modelled depending on the slug's velocity and fluid properties. Thermal conduction occurs inside the tube walls. Between the moving liquid slugs and the

tube walls, convectional heat exchange transfers heat from the evaporator tube walls into the liquid and from the liquid to the condenser section. Depending on the film thickness and fluid properties, heat is exchanged between the tube walls and vapor bubbles by film evaporation and condensation. In a dry region with no liquid film, almost no heat transfer is possible, therefore, it is usually neglected. The motion of the bubbles and liquid slugs is subject to rapid velocity and direction changes. Forces acting on the liquid slugs are pressure gradients, gravitational force, and frictional losses. The frictional losses are modelled differently for straight and bent tube sections. Knowing the forces acting on the liquid slugs and their masses, the kinetics of the system are solved with Newton's Second Law. Additional effects that need to be considered are bubble coalescence and bubble nucleation. Though some of the effects are modelled slightly differently by researchers, they agree that the specified phenomena have to be considered [46, 13].

3 Research approach and goals of this thesis

Several researchers investigated the importance of bubble generation in PHPs. Senjaya and Inoue [51] conducted numerical studies that compared the oscillations of a PHP with and without bubble generation. They observed that bubble generation causes a high local pressure increase and is, therefore, a driving force on the neighboring liquid slug's motion. Consequently, the frequency and amplitude of the oscillations in the simulations with bubble generation were much higher than in the simulations without bubble generation. In another work, they investigated dry-out phenomena and noticed that in the simulations without bubble generation, the PHP went into dry-out, while the bubble generation in the other simulations maintained the oscillations and dry-out was avoided [52]. Similar observations were made by Nekrashevych and Nikolayev [53, 46]. In their numerical studies, bubble generation was necessary to obtain a long-term, stable PHP operation when a thermally conductive wall material was used. The numerical works about bubble generation all indicate that it is a major driving force in the oscillating flow and crucial for understanding PHP behavior.

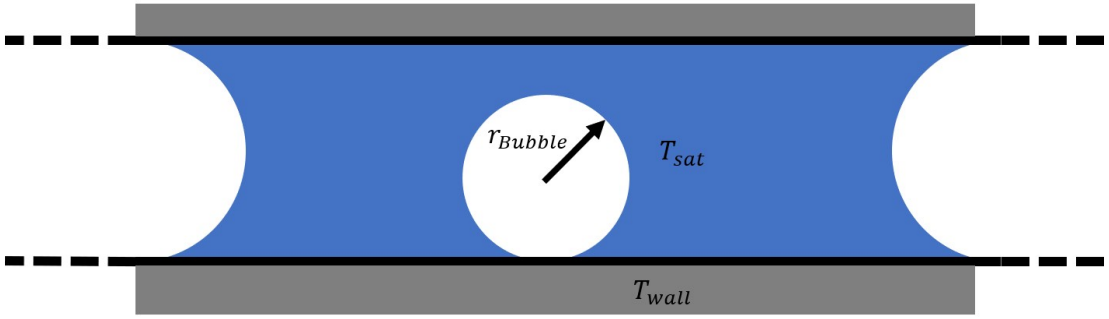

Figure 3.1: Bubble nucleation in a liquid slug

In the 1D-model of Aubin et al. [13], a universal modeling of bubble nucleation is used

that does not require predefined nucleation sites. It is assumed that if the temperature difference between the tube wall (T_{wall}) and the fluid's saturation temperature (T_{sat}), called wall superheat, locally exceeds a certain limit, a bubble is generated (figure 3.1). The threshold value is derived from the pool boiling nucleation equation and referred to in this work as nucleation threshold. The required wall superheat for nucleation (nucleation threshold) $\Delta T_{nucleation}$ is calculated by

$$\Delta T_{nucleation} = T_{wall} - T_{sat} = \frac{2 T_{sat} \sigma}{h_E \rho_{sat} r_{Bubble}}. \tag{3.1}$$

It needs to be equal to or smaller than the actual wall superheat for a bubble to be nucleated. The actual wall superheat is defined as the difference between wall temperature T_{wall} and fluid saturation temperature T_{sat}. The threshold value is calculated by the term on the right-hand side, where σ is the surface tension of the liquid phase, ρ_{sat} is the saturated vapor density, h_E is the latent heat of vaporization, and r_{Bubble} is the bubble radius [13].

Most investigations study the influence of bubble nucleation only numerically. As bubble nucleation cannot be eliminated in an experimental setup, it is much more difficult to quantitatively study its influence.

For a MEMS-based silicon micro-PHP, Sun et al. [54] analyzed the flow behavior with a high-speed camera. Operating conditions, in which the necessary wall superheat (according to the pool boiling nucleation equation) is low were favorable for the PHP. Their qualitative flow observations revealed the importance of bubble nucleation and they suggested to enlarge surface cavities to improve PHP performance.

Helical micro-grooves were used by Cai et al. [55] to increase the size of surface cavities within a PHP channel. They compared this modified PHP to a PHP without micro-grooves. Both PHPs were filled with water. The micro-grooves improved PHP performance in both vertical bottom-heated and horizontal orientation. As an explanation, two effects are named: Firstly, larger surface cavities aggravate bubble nucleation. Secondly, the micro-grooves enable liquid transport from the condenser to the evaporator due to capillary transport, similar as in standard heat pipes. This adds to the liquid transport due to pressure gradients in a PHP. The two effects that improve PHP performance could not be separated clearly and no flow visualization was performed. Therefore, the effect of bubble nucleation could not be investigated individually. Measurements in horizontal orientation showed a significantly increased dry-out limit for the PHP with micro-grooves. This suggests that the dominant effect was capillary transport improvement.

Flow visualization is a key factor in understanding a PHP's function. Qu et al. [56] investigated a PHP with a porous wick structure at the channel walls. In the flow visualization, they qualitatively observed an increased bubble nucleation rate in the PHP that was equipped with a wick structure compared to an identical PHP without a wick structure.

The thermal measurements showed that the wick structure led to an easier start-up and lower thermal resistance. At very high heat flux, no intensive bubble nucleation occurred in either of the PHPs. The pore size of the wick structure was in a range of multiple 10 μm. Therefore, capillary transport of liquid from condenser to evaporator also played a significant role here. However, the flow visualization proved that enlarged surface cavities can lead to a higher number of nucleated bubbles.

Betancur et al. [57] modified the inner channel surface using different sandpaper grit sizes. They produced a PHP with a rough channel surface in the evaporator area and a smoother surface in the adiabatic and condenser zone. They compared the results with a PHP that did not exhibit a rougher evaporator surface. With various filling ratios of water, they conducted experiments and calculated thermal resistances for each boundary condition. At low filling ratios, the rougher PHP exhibited a lower thermal resistance compared to the smooth PHP. At 50% filling ratio, both PHPs performed comparably. The smooth PHP performed superiorly at high filling ratios. The nucleation behavior was expected by the authors to be enhanced in the rough evaporator area. They expected changes in zones of pure liquid slug, the meniscus region, and the elongated bubble (liquid film) region. The theoretically required wall superheat for nucleation based on given average surface roughness values for the water filled PHP was, however, in the range of approximately 300 K for the rougher PHP and exceeded 3000 K for the smooth PHP. During the experiments, no wall superheat in this range was reached and the calculated wall superheats even exceed the thermodynamic limits of homogeneous nucleation. Bubble nucleation was, therefore, limited to statistical spikes of the surface roughness and channel edges of the rectangular channel cross-section. No significant change to bubble nucleation behavior on the full channel surfaces could, therefore, have been achieved. The measured improvement achieved with the rougher PHP was mainly at low filling ratios. According to Sun et al. [54], the major driving force of a PHP at low filling ratios is liquid film evaporation and not bubble nucleation. Liquid film evaporation was enhanced in the experiments with the rough PHP (conducted by Betancur et al. [57]) due to microscopic surface increase. Therefore, the measured thermal benefits of a rougher evaporator can be assigned to this effect rather than the effect of increased disturbances due to bubble nucleation. No flow visualization was available in the experiments. Therefore, the actual bubble nucleation rates and changes to flow behavior were not investigated.

The goal in the presented research work is to investigate the influence of required wall superheat on the behavior of a PHP. The nucleation threshold as defined in equation 3.1 was, therefore, modified in experimental setups to quantitatively investigate the influence of the changes on the overall thermal behavior of the PHP. The nucleation threshold can be varied by using a different fluid or by changing the operational temperature, as the fluid properties change with temperature. However, by changing only the fluid or the

temperature, different phenomena such as viscous friction are also influenced. Therefore, it is necessary to additionally change the bubble radius r_{Bubble} in the experiments, as this property only influences the bubble nucleation threshold. The bubble radius depends on the size of each local surface cavity. Each cavity fits a bubble of a certain radius. By influencing the surface roughness via sand or glass bead blasting, the local surface cavities are enlarged in the experiments. As there exist multiple sizes of cavities on a real surface, it is also the goal of this work to derive representative nucleation thresholds that allow to link the actual behavior in the PHP to real surface structures. Flow visualization is used to analyze bubble nucleation rates and consistently link changes in thermal resistance to changes in flow. A 1D-simulation is used to gain further insights into the behavior of the PHP.

4 Experimental setup and procedures

In chapter 4, the experimental setup and procedures are presented. In section 4.1, the physical dimensioning and design, heating and cooling, and surface analysis of the test setups are shown. The preparations of the experiments, including the cleaning and filling procedures, are also explained. The measurement equipment used is introduced in section 4.2. The explanation of the experimental setup is completed by showing the setup of the highspeed camera recordings done through the glass window of the transparent test setups in section 4.3. The experimental procedures are split into two separate parts: Firstly, the method of evaluating bubble nucleation rates from the highspeed video recordings is explained in section 4.3, followed by the explanation of the thermal characterization in section 4.4, and finally the measurement error and error propagation estimations in section 4.5 [58].

4.1 Test setups

The overall design goal for the test setups is to vary the bubble nucleation threshold. In addition to influencing the nucleation threshold by changing the fluid temperature, PHP test setups with different evaporator roughness are b uilt. In total, three geometrically identical test setups are built. The first has a smooth milled channel s urface. The second has a rough sandblasted evaporator section. The third has an evaporator section with an intermediate surface roughness created by glass bead blasting.

To find a suitable channel geometry, the Bond criterium is used to estimate the maximum hydraulic channel diameter, also referred to as critical diameter. The critical diameter D_{crit}, defined by Khandekar [59], is calculated by

$$D_{crit} = 2\sqrt{\frac{\sigma}{g(\rho_{liq} - \rho_{vap})}}, \tag{4.1}$$

where σ is the surface tension and g is the gravitational acceleration with a value of $9.81 \mathrm{m/s^2}$. ρ_{liq} and ρ_{vap} are the fluid densities of the liquid and saturated vapor phase.

For the experiments, the refrigerant R1233zd(E) is chosen due to its low global warming potential value of 5 [60]. To calculate the critical diameter for the chosen refrigerant, temperature dependent fluid properties are needed. For the surface tension σ of R1233zd(E), Konduo [61] has presented an estimation equation based on experimental data. σ is calculated by

$$\sigma = 0.06195(1 - T_{fluid}/438.75K)^{1.277}[N/m]. \tag{4.2}$$

The densities are published by Mondejar [62]. Subsequently, figure 4.1 shows the critical diameter calculated for R1233zd(E) according to equation 4.1. The critical diameter is above 1.7 mm in the intended operating range of 0°C to 80°C. As the influence of gravity on the behavior of the PHP decreases with decreasing diameters [14, p. 116], a hydraulic diameter of 1 mm is chosen for the experimental setup to keep a distance to the critical value of 1.7 mm at 80°C. The channel cross section is rectangular with 1 mm width and 1 mm depth.

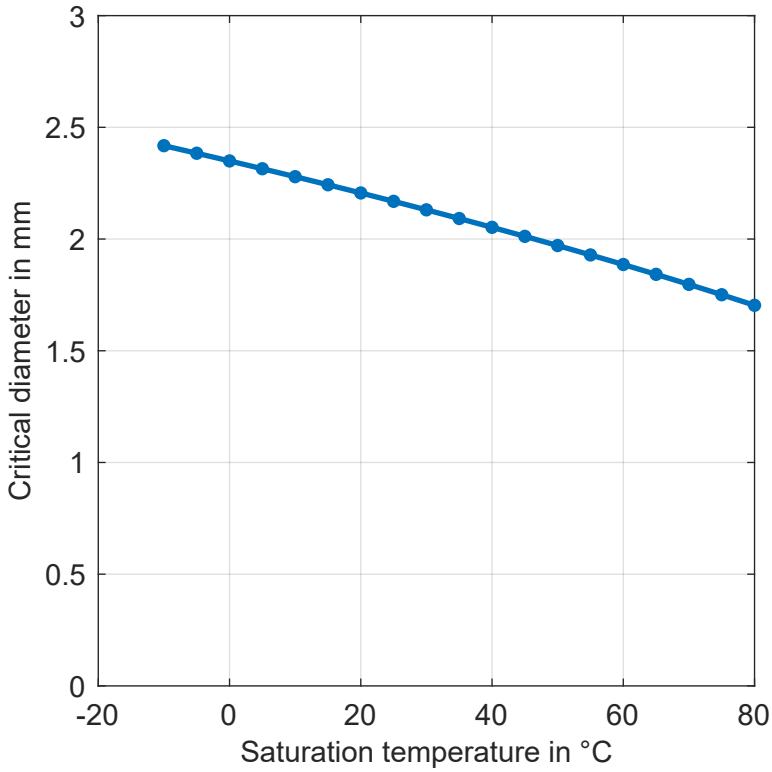

Figure 4.1: Critical diameter of R1233zd(E)

A further design aspect is the number of turns of the PHP. According to Khandekar [14, p. 118], a higher number of turns leads to an increased level of flow disturbances. Therefore, the number of turns in this study is kept relatively low at 6 to better visually distinguish the influence of bubble nucleation on the flow pattern and thermal performance.

4.1.1 Mechanical setup

To enable visual access to the channels, a flat plate design with a glass cover plate is chosen for the PHP. The full schematic setup can be seen in figure 4 .2. An aluminum plate with a thickness of 3 mm is used for the plate, referred to as the baseplate. The channels are milled into the baseplate and closed by covering the baseplate with a glass plate. Baseplate and glass plate (with a sealing O-ring in between) are pressed together by frames made of stainless steel. The frames are pulled towards each other by a flange. The screws of the flange are not shown in the figure.

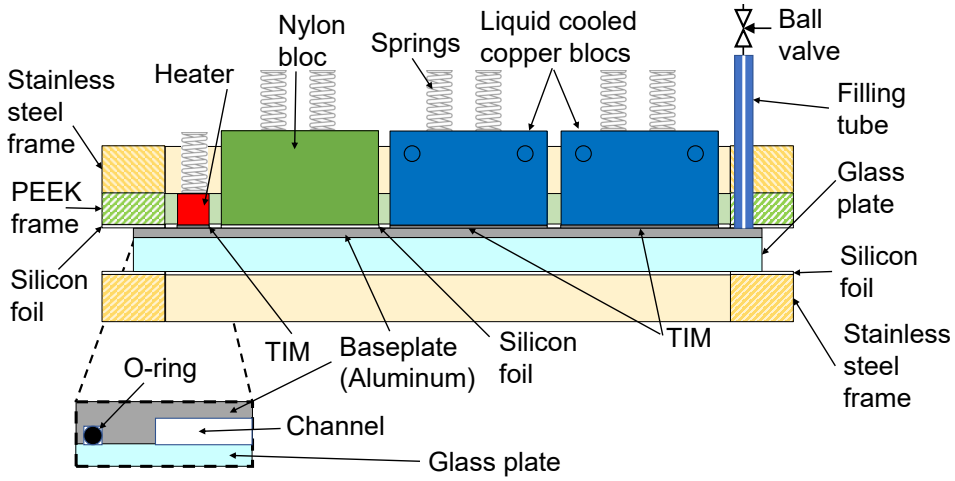

Figure 4.2: Schematic drawing of the full setup

To ensure thermal insulation between the baseplate and the frame, there is a plastic (PEEK frame in between. Between the PEEK frame and the baseplate is a 1 mm silicon foil to counterbalance manufacturing tolerances and ensure homogeneous compression at the O-ring seal. It also provides extra thermal insulation. A silicon foil can also be found between the glass plate and the lower steel frame. The thermal boundary conditions are applied on the back of the baseplate, where no channels are located. A heater is on the left side and two copper coolers are on the right side. In between, a nylon block

keeps the adiabatic zone insulated. Heater and coolers are contacted to the baseplate with a thermal interface material (TIM). The TIM (Leader Tech TGF60) has a nominal thermal conductivity of 6 W/(mK) [63] and a thickness of 0.5 mm. The nylon block is separated from the baseplate by a silicon foil. The heater, nylon block, and copper coolers are pressed onto the baseplate with a spring system (figure 4.2). The springs create a contact pressure of 3 bar. On the right side of figure 4.2, the filling tube can be seen. It is screwed into the upper stainless steel frame and is, therefore, pressed onto the baseplate. An O-ring seal is located between the baseplate and the filling tube. The filling tube is closed at the top side by a Swagelok ball valve. By closing the ball valve, the PHP is hermitically sealed.

The channel structure of the baseplate, comprising a meandering channel with 6 turns and 12 parallel channels, can be seen in figure 4.3. The channel area is surrounded by a wider groove that is holding an O-ring. The O-ring seals the aluminum plate against the glass plate that is pressed on top of the baseplate. The meandering channel structure has a return loop on the right side that connects the outer most channels. The return loop has a small channel towards the right. This section is called the filling channel and connects the channels with the filling port.

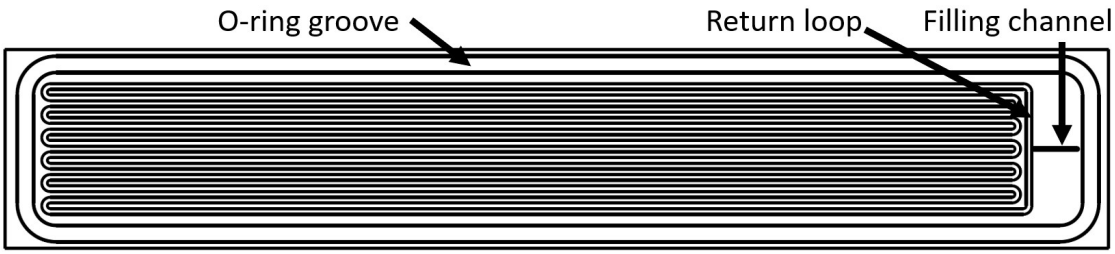

Figure 4.3: Baseplate top view

Figure 4.4 shows the channel side of the baseplate, including the thermal zones: evaporator, adiabatic, and condenser zone. The evaporator zone is heated with the resistance heater shown in figure 4 .2. The heater has a size of 10 mm by 24 m m. Therefore, the evaporator zone comprises an area of 2.4 cm^2. The condenser section comprises two liquid cooled copper blocks. Each copper block cools an area of 50 mm by 24 mm. Thus, the total condenser area is 100 mm by 24 mm. As there are two coolers, the condenser zone can be split into two sections: condenser zone 1 and 2. The adiabatic zone covers an area of 60 mm by 24 mm.

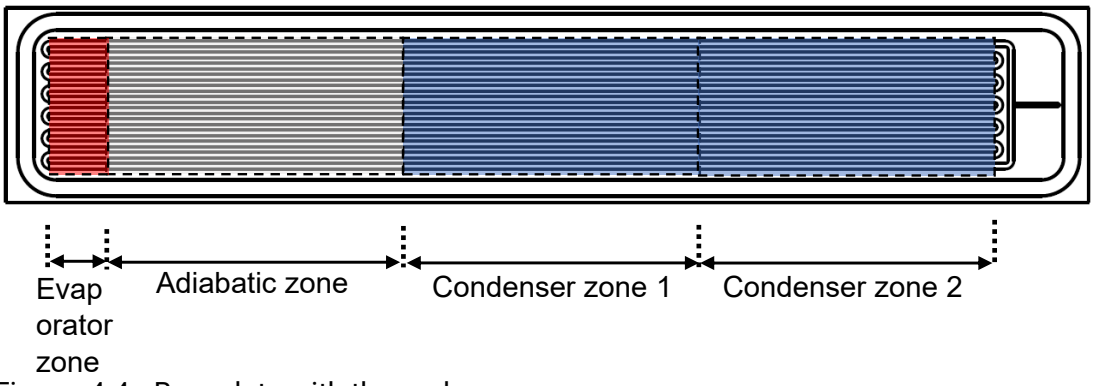

Figure 4.4: Baseplate with thermal zones

Figure 4.5 shows a detailed view of the evaporator end of the PHP with the channel layout. The channel pattern is rasterized. It exhibits one channel every 2 mm. This implies that the turns have an average bent radius of 1 mm. The geometrical details of the O-ring groove can also be found in this drawing. Full engineering drawings of the baseplate with all relevant dimensions can be found in appendix 10.1 (Fig. 10.8).

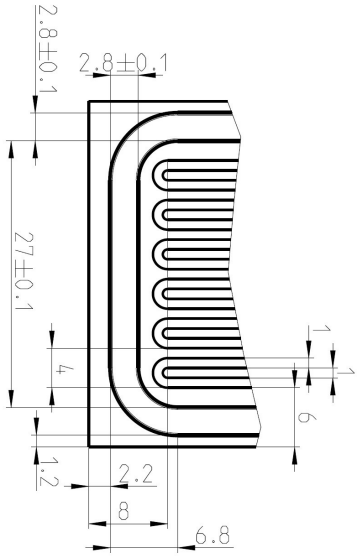

Figure 4.5: Detail of evaporator end of the PHP

Figure 4.6 shows the end of the condenser zone (right side) of the channel layout. The

geometry of the filling channel and return loop are depicted. The filling channel has a cross section of 0.5 mm by 0.5 mm and is, thus, considerably smaller than the main channels. Hence, the influence of the filling channel on the flow behavior is kept to a minimum. The filling channel leads to a through hole that connects the front (channel structure) of the baseplate with the back. The hole grants access to the channel structure from the filling port that is located at the back of the baseplate.

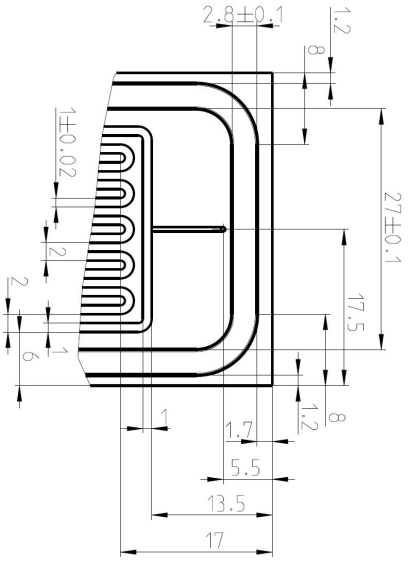

Figure 4.6: Detail of condenser end of the PHP with filling channel

Figure 4.7a shows the back side of the baseplate where no channels are located. Instead, there are long grooves along the baseplate, where thermocouples can be installed. At the condenser end of the PHP, a circular O-ring groove holds the O-ring seal between the filling tube and the baseplate. All O-ring seals are FKM seals of 2 mm thickness. A cross-sectional view of the assembly with the baseplate, the glass plate, the filling tube, and the O-ring seals can be found in figure 4.7b.

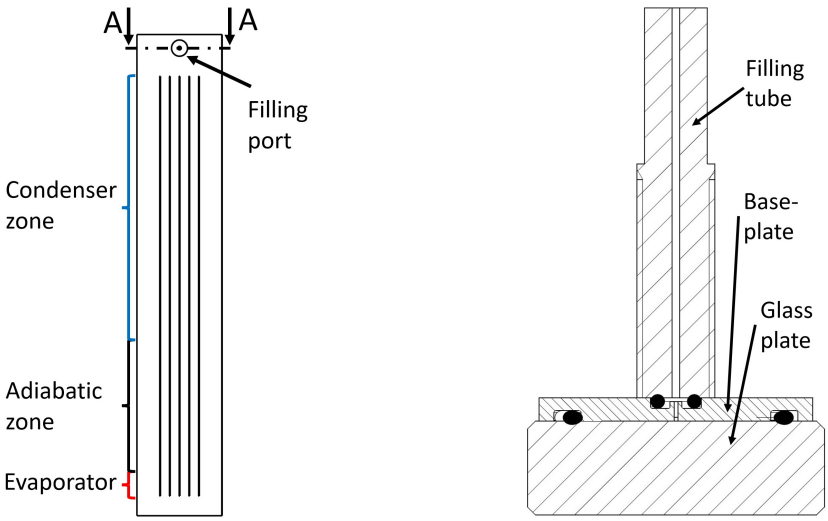

(a) Location of cross-section view (b) Cross-section view A-A of filling port

Figure 4.7: Cross-section view of filling port assembly

For the evaporator zone, a specialized resistance heater was designed to fit the needs of the experiments. The heater is shown in figure 4.8. It consists of an electrically conductive meander made of stainless steel. The meander has very small gaps between the meander lines and has, therefore, a homogeneous heat flux density. It is made from a stainless-steel sheet metal with a thickness of 0.05 mm that is glued onto a block of PEEK plastic with a high temperature glue. This equips the heater assembly with a very low thermal capacity, enabling steep temperature gradients in heating.

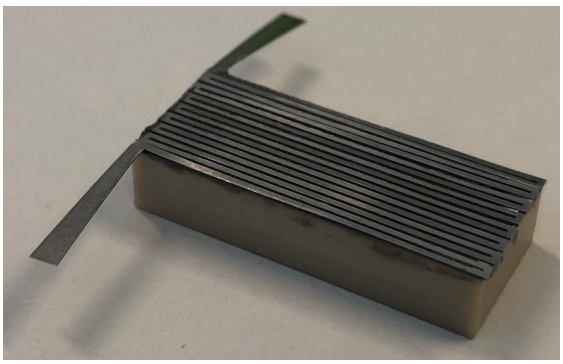

Figure 4.8: Electrical heater

The coolers are made of copper blocks with channels inside. Four copper tubes are connected to the cooler for coolant supply. The cross section of the cooler can be seen in figure 4.9. All channels are in a parallel circuit and receive coolant at equal inlet temperatures. The baseplate and frame assembly, including the heater and the coolers placed on top of the baseplate, can be seen in figure 4.10. The coolant flow directions inside the coolers are indicated. The setup operates in a counterflow mode where the direction of coolant flow opposes the heat transfer direction in the baseplate. The view also shows the filling tube at the back of the baseplate. The adiabatic zone is left clear here for better visibility and only a few screws are attached to the stainless-steel frame. The final setup uses all screw positions for a homogeneous compression.

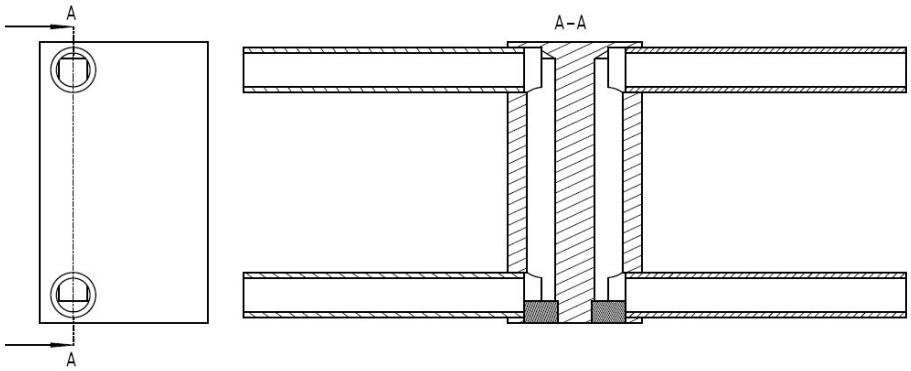

Figure 4.9: Cross-section view of copper cooler with pipes attached

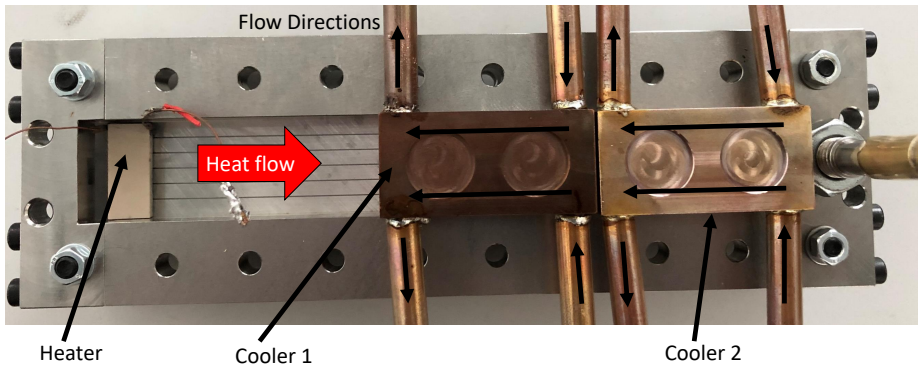

Figure 4.10: Assembly with heater and cooler (including flow directions), without peripheral components

Figure 4.11 shows a view of the assembled test setup from the top. The channels are clearly visible through the glass plate, thus, enabling flow observation. The backside of the test setup is covered in thermal insulation (Armaflex) of minimum 40 mm thickness to minimize thermal losses to the environment.

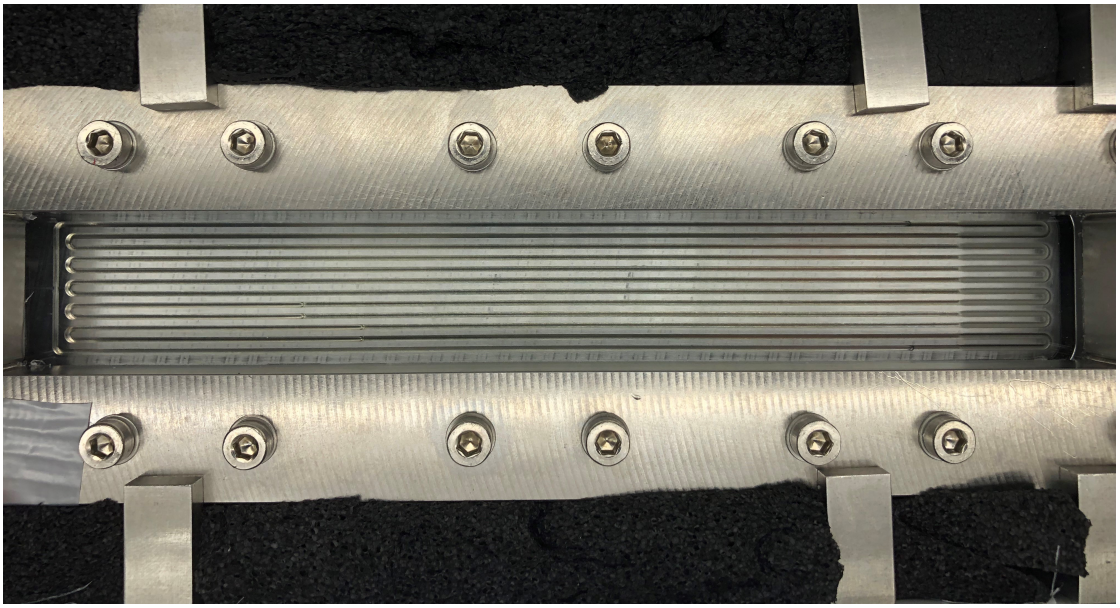

Figure 4.11: Top view of fully assembled PHP test setup

4.1.2 Surface treatment and characterization

To create three geometrically identical test setups with varying channel surface roughness, different surface treatments are needed. Table 4.1 gives an overview on the treatments that were used for each setup. Test setup 1 has the smoothest surface; the channels are milled with no further treatment. Setups 2 and 3 also have milled channels, but the surface structures in the evaporator sections were influenced afterwards by sand blasting and glass bead blasting, respectively. For both setups, only the evaporator area was treated. The remaining channel segments were left out and, therefore, exhibit the original surface structure from the milling process. The blasting area is slightly larger than the evaporator area (15 mm by 24 mm instead of 10 mm by 24 mm) to ensure a homogeneous surface structure within the evaporator area. The blasted area with respect to the evaporator section (red) can be seen in figure 4 .12. The top surface segments of the baseplate in between the channels were covered with a protective templet in the blasting process and,

therefore, remain smooth. The general parameters for the blasting techniques can be found in table 4.1. This results in a rather high roughness in the evaporator section of setup 2. Test setup 3 has a medium roughness in the evaporator section.

Parameter	Test setup 1	Test setup 2	Test setup 3
Technology	Milling	Milling + sand blasting	Milling + glass bead blasting
Blasting material	None	Sand	Glass beads
Blasting distance	None	10 cm	10 cm
Blasting pressure (absolute)	None	4 bar	1.7 bar
Blasting duration	None	20 s	20 s

Table 4.1: Overview of surface treatment parameters for all test setups

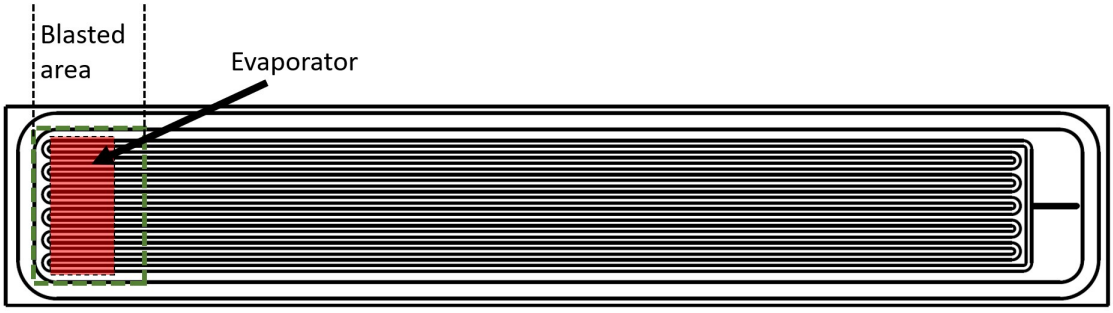

Figure 4.12: Blasted areas of test setups 2 and 3

The surface treatment via blasting is only reproducible if the blasting material is characterized sufficiently. Therefore, various analysis were done on the two different blasting materials. Firstly, the particle size distribution was analyzed with a laser diffraction particle size analyzer. The device used for the measurements was a Malvern Mastersizer Hydro 2000S. The results can be seen in figure 4.13. The sand blasting material used for setup 2 has a large average particle size of 131 μm. The size ranges from around 50 μm to 350 μm, with 50% of the particles being smaller than 139 μm and 90% smaller than 217 μm. The glass bead blasting material used for setup 3 has a narrower size range and a lower average size of 87 μm. 50% of the particles were smaller than 90 μm and 90% of the particles were smaller than 123 μm.

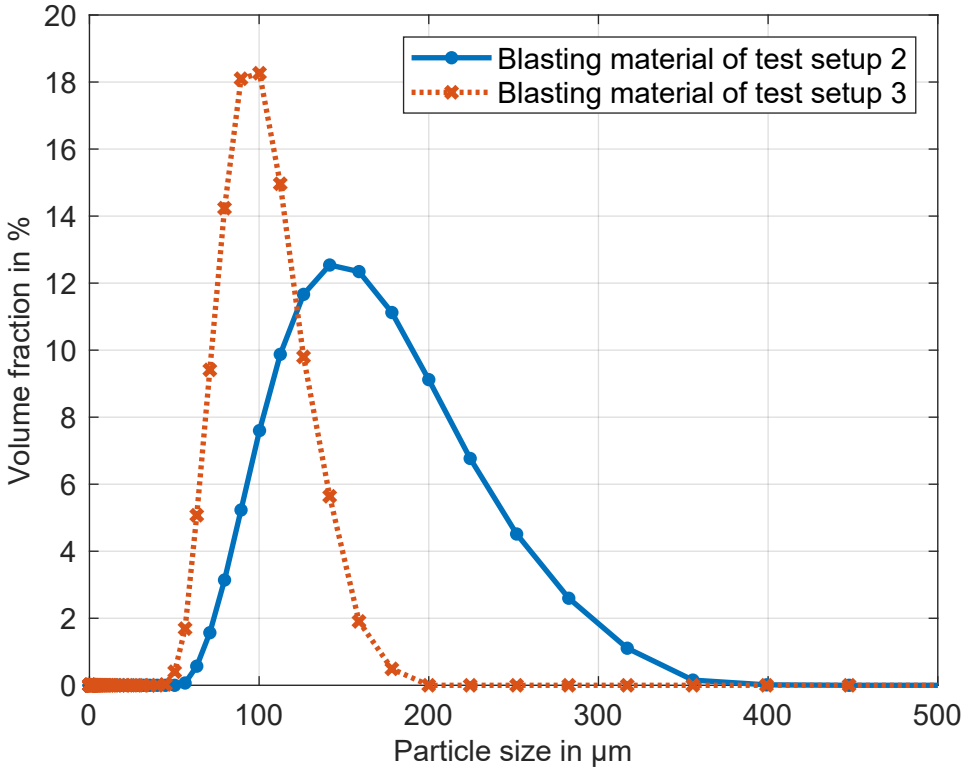

Figure 4.13: Particle size distribution of blasting material

Images of the blasting material were made with a scanning electron microscope (SEM) to get an impression of the particle shapes. The device used to create the images was a FEI Quattro S. Figure 4.14 shows the image of the sand blasting material used for setup 2. The particles have an angular appearance with sharp edges. The image also verifies the impression gained from the particle size distribution; the size of the particles varies in a wide range. Figure 4.15 shows the image taken of the glass bead blasting material used for setup 3. It reveals uniformly shaped spherical particles of roughly the same size, often agglutinated with smaller sized spherical particles. Lastly, the chemical properties of the blasting material were investigated using energy dispersive spectroscopy (Oxford Instruments System AZTec). It revealed the atomic main components of the sand blasting material used for test setup 2 to be aluminum, silicon, and oxygen. Therefore, the material is mainly a mixture of aluminum oxide and silicon oxide. The main component of the glass bead material used for setup 3 is silicon oxide.

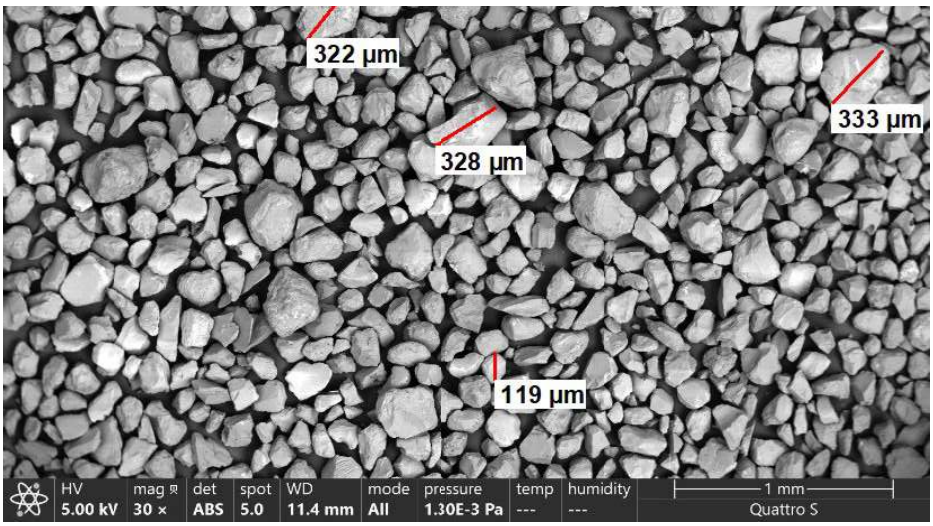

Figure 4.14: SEM-image of blasting material used for test setup 2

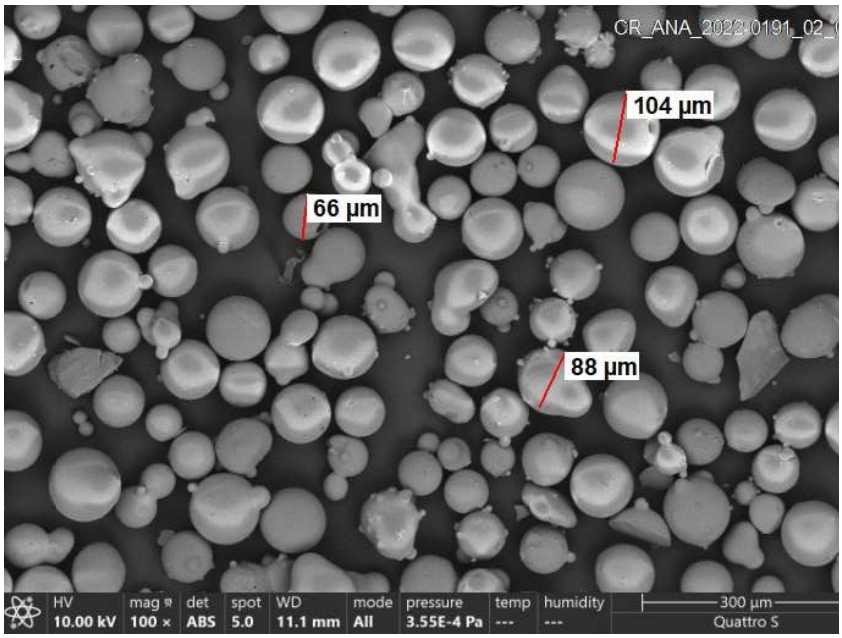

Figure 4.15: SEM-image of blasting material used for test setup 3

To evaluate the surface structure and roughness of each setup's channel surface, a surface profile measurement was done. A confocal was used to create 3D scans of small surface fractions of the channel ground. Hans-Joachim Jordan et al. [64] published the measurement principle. The confocal used is a Nanofocus μ surf c with a 320 L optical module that has a measurement area of 320 μm by 320 μm. It has a resolution of 512 by 512 pixels. Because the roughness might be inhomogeneous, several measurement points are needed to get a good average value. The first setup has no sand blasted area. Instead, the channels are only milled. Ten measurement points for surface evaluation are recorded across the full channel layout. Figure 4.16 shows the positions of all ten measurement points of setup 1. For setups 2 and 3, twenty measurement points are recorded, as can be seen in figure 4.17. Six of them (1-6) are located in the milled main section of the setup's channels that are not further treated. They were used to ensure constant surface properties in all milled regions for all test setups. Fourteen (7-20) are located within the sand/ glass bead blasted zone to characterize the evaporator surface roughness.

Figure 4.16: Surface measurement positions of test setup 1

Figure 4.17: Surface measurement positions of test setups 2 and 3

Each measurement position reveals the local 3D surface profile. Because of reflections, single defective measurement points exist within a surface profile. This is solved by low pass filtering the data. Example surface profiles after low pass filtering can be seen in figure 4.18 for each test setup. The profile of test setup 1 is recorded at measurement position 1. It shows a typical milled surface structure with curved micro grooves created by the front milling process with an end milling cutter. The z-component of the profile is mainly in the range between -0.5 μm and +0.5 μm. The profile of test setup 2 shown here is recorded at measurement position fifteen and, thus, located within the sandblasted area. The profile is clearly distinguishable from the profile of setup 1, because the z-component is in a range between -15 μm and +10 μm. It is, therefore, a lot rougher in comparison. The sand blasting process has left many micro cavities that create an overall ragged profile.

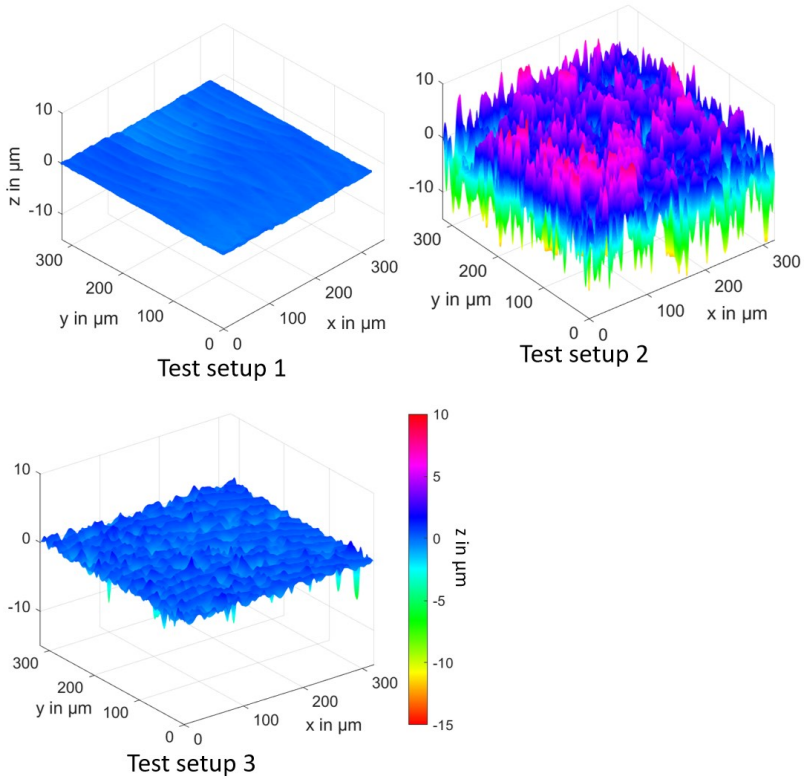

Figure 4.18: 3D surface plots of all test setups (lowpass filtered)

Lastly, the surface scan of test setup 3 shows the profile in the glass bead blasted area. The profile was recorded at measurement position fifteen. The z-component exhibits

values between the ranges of the two previous surface profiles and is mainly between -4 μm and +2 μm. Due to reduced blasting pressure, there are fewer deep cavities compared to the sand blasted area of setup 2, but a ragged profile is still visible here. More detailed versions of each surface scan can be seen in appendix 10.1 (figures 10.1, 10.2, 10.3).

The roughness of the three test setups is best compared in cross-sectional cuts of the 3D profiles. The cuts are visible in the x-z-plane and are located at a y-position of 100 μ m in the 3D profiles. The cuts through all three profiles are compared in figure 4.19. The profiles of setups 2 and 3 were both located within the treated evaporator area, so they were influenced by the sand blasting and glass bead blasting process, respectively. Setup 1 has a very smooth surface, as there are hardly any variations in the z-component visible in the diagram. Setup 2 has the roughest surface and setup 3 an intermediate surface roughness.

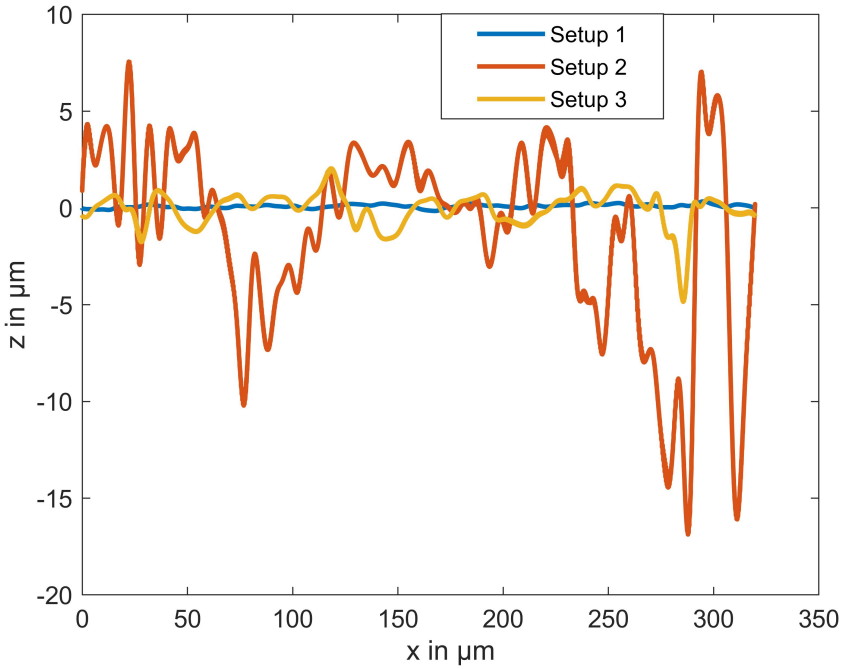

Figure 4.19: comparison of 2D surface cross section plots (lowpass filtered)

There are many ways to classify a surface structure and its roughness. Most commonly used are the arithmetic average roughness Ra, the root mean square roughness Rq, and the ten point height Rz as described by Rao [65]. All of them, however, cannot sufficiently describe the influence of the surface structure on the bubble nucleation b ehavior. Therefore,

a more suitable representative value for the surface roughness that characterizes its nucleation behavior is defined. The evaluation is based on a 3D surface profile. In figure 4.20, the same surface profile as shown in figure 10.1 can be seen in a 2D top view. The z-values of the surface are displayed by color here. Firstly, the newly developed algorithm finds all the local minima and maxima of the profile. They are also displayed in figure 4.20: Minima are depicted as red dots and maxima as blue dots. All the minima represent cavities where bubbles are potentially nucleated. The size of the cavities is an important factor for bubble nucleation because it determines the size that a bubble can reach within the local microstructure. Therefore, the maximum possible bubble radius for each local cavity must be estimated within the 3D profile.

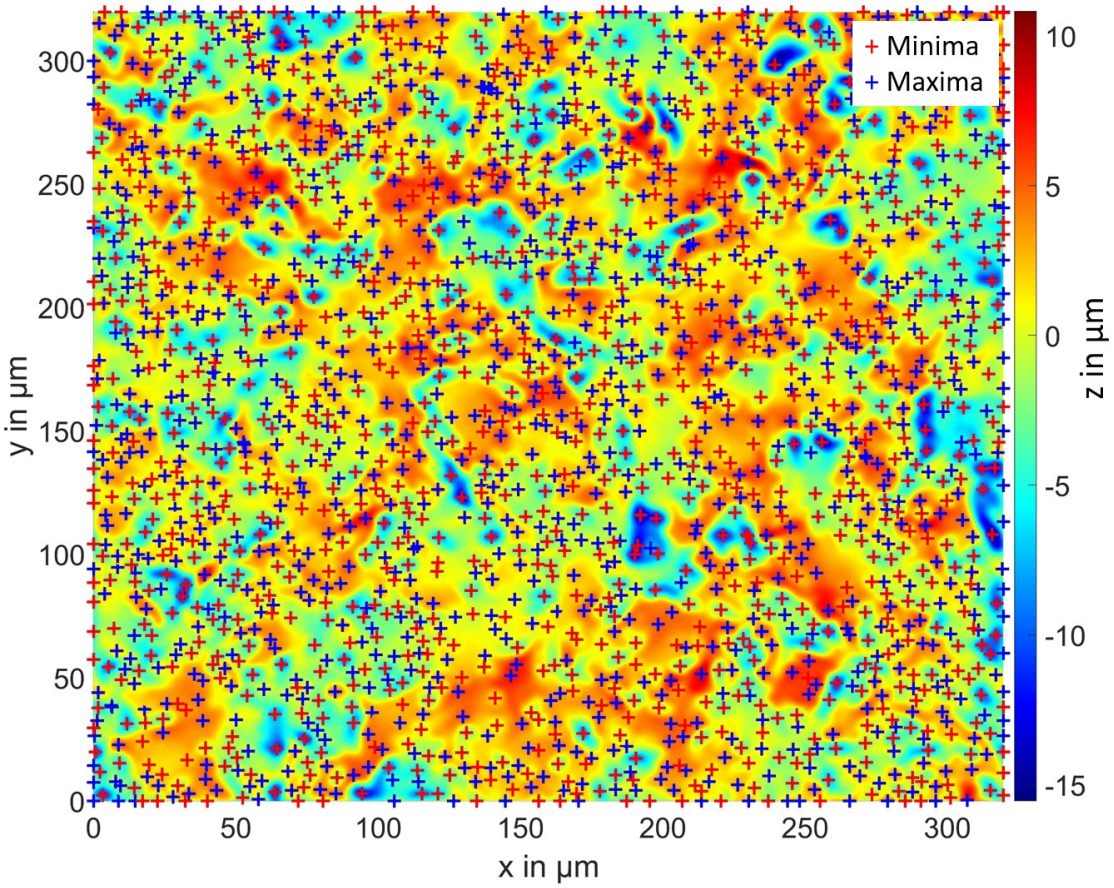

Figure 4.20: Local surface minima and maxima (test setup 2)

To explain the local evaluation process for the maximum bubble radius of a single cavity, the 3D surface profile is displayed as a local cross-sectional view in figure 4.21. The measured surface profile, the local minimum (red dot), and the local maxima (blue dots) are visible here. The algorithm firstly detects the nearest maximum to the minimum (or cavity) under investigation. For this, two dimensions are considered: The horizontal distance in the x-y plane and the vertical distance (the difference in the z-component). In this case, the smallest distance is the horizontal distance from the minimum to the left maximum, labelled as h1 in the plot. The minimum distance, either horizontally or vertically, is limiting the maximum expansion of the bubble that is formed in this cavity. Therefore, the maximum bubble radius is defined as the minimum of horizontal and vertical distance to the nearest local maximum. This algorithm is a simplification, as to determine the real radius of a bubble within a surface cavity, the contact angle between the refrigerant and the wall would have to be considered. However, the measurement of this contact angle is very challenging (due to very low angles) and could, therefore, not be done for this study. The simplification was assumed to yield sufficiently approximate results.

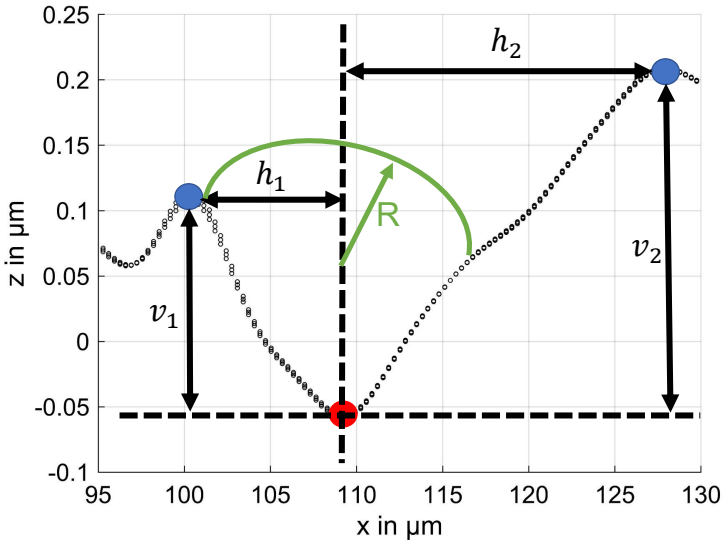

Figure 4.21: Local bubble radius evaluation method

The surface evaluation yields a maximum bubble radius for each cavity, or local minimum. For a full profile, this results in a number of cavities with each an assigned bubble radius. A bubble radius distribution can, thus, be identified for each surface p rofile. An example

bubble radius distribution of the surface within the evaporator is shown for each test setup in figure 4.22. The radius was discretized into intervals with a length of 0.1 μm. To display the distribution profile, the number of cavities within a radius interval was counted, yielding a number of occurrences that is displayed in figure 4.22. The distribution of setup 1 shows small bubble radii that are generally below 1 μm, with a peak of occurrences at 0.045 μm. The bubble radius is mainly limited by the difference in the z-component, which also applies to the other two setups. Test setup 2 has bubble radii up to 12 μm. Most bubble radii are found around 5 μm with a peak at 5.6 μm. Setup 3 has bubble radii up to 7 μm with most of them below 2 μm. The distribution has a peak at 1 μm.

A bubble radius distribution curve offers helpful information to characterize the surface with regard to bubble nucleation. However, distribution curves for several measurement points for each setup are not easy to handle and cannot be used in correlations. Therefore, an arithmetic average bubble radius is determined for each distribution profile. For one test setup, the average bubble radii of several measurement points are averaged to a single bubble radius value for the test setup.

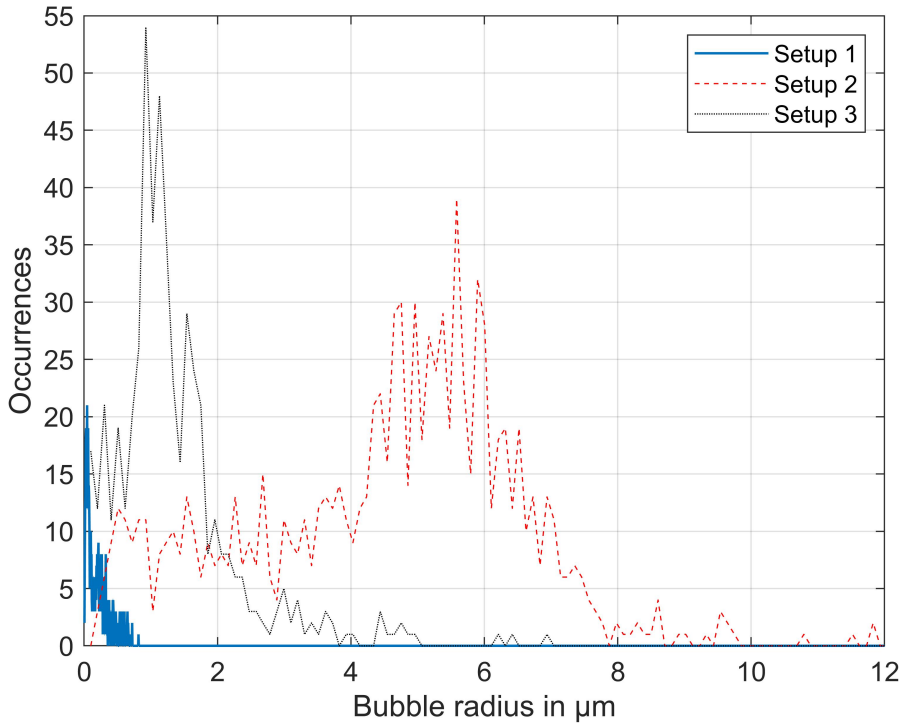

Figure 4.22: Bubble radius distributions (radius interval: 0.1 μm)

As setup 1 has a homogenous milled channel surface, all measurement points are used for averaging. Setups 2 and 3 have a treated evaporator section. Therefore, only the measurement positions located within the treated zone are used for the average value. This yields an average bubble radius value for each setup's evaporator section. The results are listed in table 4.2. The results also support the previous observations: setup 1 has the smoothest, setup 2 the roughest, and setup 3 an intermediate surface roughness.

	Test setup 1	Test setup 2	Tet setup 3
Technology	Milling	Milling + sand blasting	Milling + glass bead blasting
Average bubble radius	0.21 μm	4.54 μm	1.26 μm

Table 4.2: Overview of average bubble radii of all test setups

4.1.3 Preparation of experiments

After manufacturing of the baseplates with milling and sand or glass bead blasting, the assembly of the components is prepared. The components baseplate, glass plate, O-rings, filling tube, and ball valve are in direct contact with the refrigerant. Contamination of the refrigerant by remaining particles or oil on these components must be avoided. Therefore, these components need to be as clean as possible before assembly. Deposits of coolant and oil from manufacturing and particles from sand/ glass bead blasting need to be removed. Therefore, a standardized cleaning procedure was established for all components in direct contact with refrigerant:

1) Removing dust and blasting material with compressed air.

2) Cleaning in acetone ultrasonic bath for 10 min.

3) Cleaning in distilled water ultrasonic bath for 10 min.

4) Cleaning in isopropanol ultrasonic bath for 10 min.

5) Cleaning in distilled water ultrasonic bath for 10 min.

6) Drying in nitrogen flow.

The only exception is that for cleaning of the O-rings in step 2 isopropanol is used instead of acetone to avoid embrittlement of the O-rings. The assembly follows directly after the cleaning and drying to avoid any particle contamination. After assembly, the setups were evacuated to remove any moisture that could have been introduced by the surrounding air during assembly. The moisture removal was done by evacuating the PHPs for two hours, followed by a nitrogen flush of the inner volume. The process was repeated three times. Then, the PHPs were evacuated for three days.

Before filling the PHPs with refrigerant, a leak test was done. This consisted of a vacuum leak test and a pressure leak test. An example pressure measurement curve for vacuum leak testing can be seen in figure 4.23a. The average pressure rise per 24 hours was determined over the full measurement time of around 2 days. For the pressure testing, the PHP was filled with nitrogen to the intended test pressure. The test pressure was defined as the refrigerant vapor pressure at 55°C. This was the expected maximum refrigerant temperature for a condenser temperature of 40°C (intended operating range). The test pressure is, therefore, 3.5 bar. As can be seen in figure 4.23b, the pressure decreased slightly over time. Displayed in the diagram is only a time interval of 12 hours to make the temperature and associated pressure changes visible. Nevertheless, for the full pressure test, a time interval of around three days was recorded and an average value for the pressure loss per 24 hours was calculated.

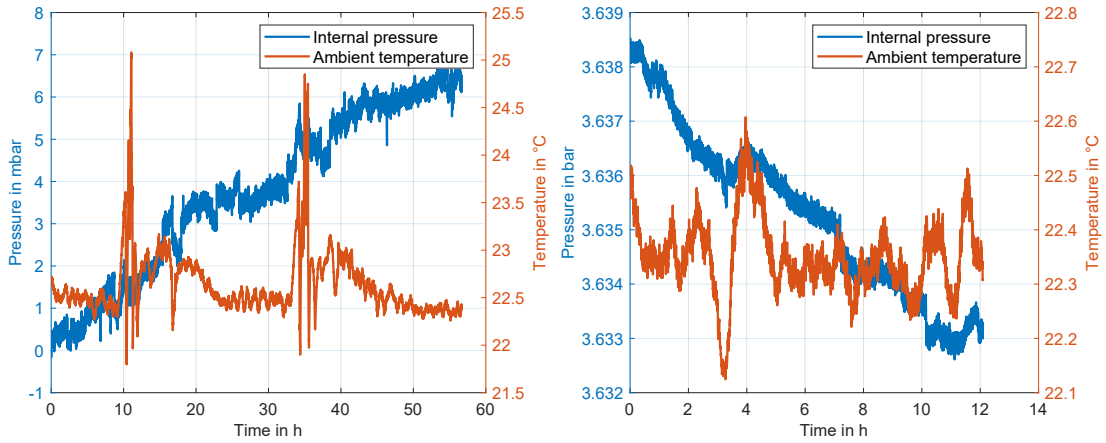

(a) Vacuum leak testing for test setup 3

(b) Pressure leak testing for test setup 3

Figure 4.23: Leakage testing of test setup 3

If start and end temperature of the pressure leak testing are not identical, the leakage rate result will be affected. Therefore, a corrected pressure $p_{compensated}$ that would be

in the system at a constant temperature of 20°C was calculated for the pressure loss evaluation by

$$p_{compensated} = \frac{p_{internal} * 293.15K}{T_{ambient}}, \tag{4.3}$$

where $p_{internal}$ is the measured pressure and $T_{ambient}$ is the measured ambient temperature in Kelvin. The compensation allows to calculate a pressure leakage rate independent of temperature changes during the test interval.

The resulting average pressure changes are shown in table 4.3. The largest leakage in the pressure test was 7.4 mbar in 24 hours for test setup 3. the largest vacuum pressure rise was 4.25 mbar in 24 hours for setup 2.

Test setup	Vacuum test	Vacuum leakage rate	Pressure test	Test pressure	Pressure leakage rate
	mbar/24h	mbar*L/s	mbar/24h	bar	mbar*L/s
1	2.94	6.7E-8	-5.0	3.51	1.1E-7
2	4.25	9.6E-8	-2.3	3.60	5.1E-7
3	2.65	6.0E-8	-7.4	3.64	1.7E-7

Table 4.3: Overview of leakage pressure changes and leakage rates for all test setups

To evaluate, whether these values are acceptable for the planned experiments, the consequences of a leakage must be considered. At high internal pressure due to high vapor temperature, a leakage rate leads to refrigerant loss. To estimate the refrigerant mass loss, it is assumed, that the volume flow rates out of the PHP at the point of leakage are identical for air ($\dot{V}_{air}$) and the refrigerant ($\dot{V}_{vap}$) for the same pressure. The volume flow rates are determined with respect to the fluid properties inside the PHP. Therefore, it can be stated that

$$\dot{V}_{vap} = \dot{V}_{air}. \tag{4.4}$$

The air volume flow rate can further be determined by

$$\dot{V}_{air} = \frac{-\dot{m}_{air}}{\rho_{air}}, \tag{4.5}$$

where $\dot{m}_{air}$ is the time derivative of the air mass inside the PHP and ρ_{air} is the density of the air. For air, the time derivative of the ideal gas equation is

$$\dot{p}_{air} V_{PHP} = \dot{m}_{air} R_{air} T_{air}, \tag{4.6}$$

where $\dot{p}_{air}$ is the time derivative of the air pressure during leak testing, V_{PHP} is the internal volume of the PHP, R_{air} is the specific ideal gas constant for air, and T_{air} is the air temperature. As $\dot{p}_{air}$ is measured, $\dot{m}_{air}$ can be calculated by

$$\dot{m}_{air} = \frac{\dot{p}_{air} V_{PHP}}{R_{air} T_{air}}. \tag{4.7}$$

The air density can be derived from the ideal gas equation and is calculated by

$$\rho_{air} = \frac{p_{test}}{R_{air} T_{air}}, \tag{4.8}$$

where p_{test} is the pressure of the air during leak testing. As the pressure changes are small during leak testing, p_{test} is assumed to be constant. Combining equations 4.4, 4.5, 4.7, and 4.8, the refrigerant volume flow rate can be calculated by

$$\dot{V}_{vap} = \frac{-\dot{p}_{air} V_{PHP}}{p_{test}}. \tag{4.9}$$

The time derivative $\dot{m}_{vap}$ of the vapor mass inside the PHP for the internal pressure p_{test} can then be calculated by

$$\dot{m}_{vap} = -\rho_{vap} \dot{V}_{vap} = \frac{\dot{p}_{air} V_{PHP} \rho vap}{p_{test}}. \tag{4.10}$$

For a time interval $t_{exposure}$ that the PHP is operated at the pressure p_{test}, the refrigerant mass loss $\Delta m_{loss,refrigerant}$ is then estimated to be

$$\Delta m_{loss,refrigerant} = \frac{|\dot{p}_{air}| V_{PHP} \rho_{vap} t_{exposure}}{p_{test}}. \tag{4.11}$$

For the described worst case with test setup 3, the vapor density is 19.3 kg/m^3. $t_{exposure}$ is conservatively estimated to be 24 hours until the PHP is refilled. This results in a maximum refrigerant loss of 8.2E-5 g. If the PHP was fully filled with liquid refrigerant, it contained approximately 2.5 g of refrigerant. With a minimum filling ratio of 30%, the minimum filled refrigerant mass is 0.75 g. The maximum refrigerant loss would then be 0.01% of the refrigerant in the PHP. This can be considered negligible.

The consequence of leakage while the internal vapor pressure is below the ambient pressure, is air leaking into the PHP. The minimum pressure that exists during the experiments is the saturated vapor pressure at 0°C, which is 0.48 bar. For simplicity and conservatism, the measured leakage pressure change at an internal pressure of 0 bar is used from the vacuum leakage test. The maximum exposure time at these temperatures

and internal pressures is estimated to be 12 hours before refilling the PHP. In the worst case of test setup 2 the pressure rise is 4.25 mbar in 24 hours. Therefore, in 12 hours the maximum reachable partial air pressure in the system will be 2.1 mbar. As this is calculated very conservatively, the value is acceptable for the experiments.

Figure 4.24 shows a partially filled PHP. The phase boundaries are clearly visible in the image. As the test setup is fully assembled and has a total weight of several kilograms, measuring the filling ratio by weighing the test setup would be far too inaccurate and time consuming. Before each weighing, the coolant tubes would have to be disconnected and the coolers emptied. Therefore, the filling ratio is analyzed optically. Looking into an image of the partially filled PHP in detail (figure 4.24), the liquid filled channel segment lengths can be measured and compared to the full channel length of the PHP. In the detailed view of figure 4.24, liquid phase is on the left side of each phase boundary and vapor is on the right. This method yields reproducible filling ratio analysis.

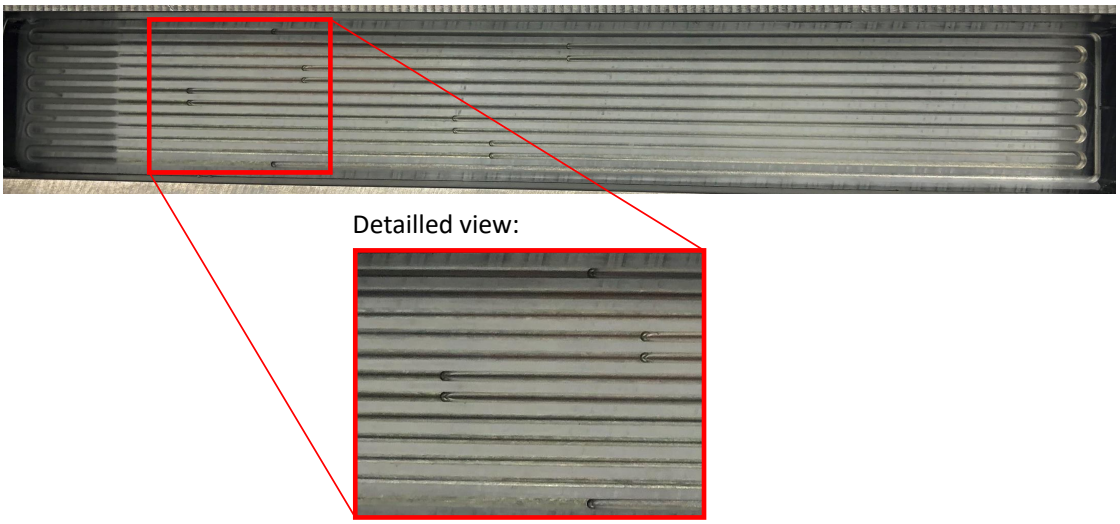

Figure 4.24: Detailed view of partially filled PHP

4.2 Measurement equipment

The measurement equipment is grouped into three different c ategories: Thermal measurement, electrical power measurement, and optical measurements. While the optical measurement system is completely independent of the other measurements, thermal and electrical measurements share a common data acquisition system. Both use a National

Instruments cDAQ-9189 rack system with separate measurement modules each. The data acquisition rack is coupled with a computer running a LabView software for control of the experiments and data recording.

To supply a constant heat flow, a power supply with power regulation (EA-PS 3040-10C) is used. The liquid coolers are provided with coolant of constant inlet temperature from a thermostat (Huber CC-508). The thermostat is operated at a fixed rotational speed of 2000 rpm to facilitate a constant volume flow rate. The coolant inlet temperature of the liquid coolers is regulated and kept at a pre-set value. Both the thermostat and the power supply can be controlled via the LabView software.

For thermal measurements, 17 type K sheath thermocouples with 0.25 mm diameter are installed on the baseplate of each test setup. The positions are defined with respect to the thermal zones. As documented in figure 4.25, five thermocouples are located in the evaporator zone (1 to 5), four thermocouples are placed in the adiabatic zone (6 to 9), and a total of eight thermocouples are placed in the condenser area (10 - 17) with four beneath each cooler. To measure the thermocouple temperatures, two National Instruments 9214 modules are used in the data acquisition rack system.

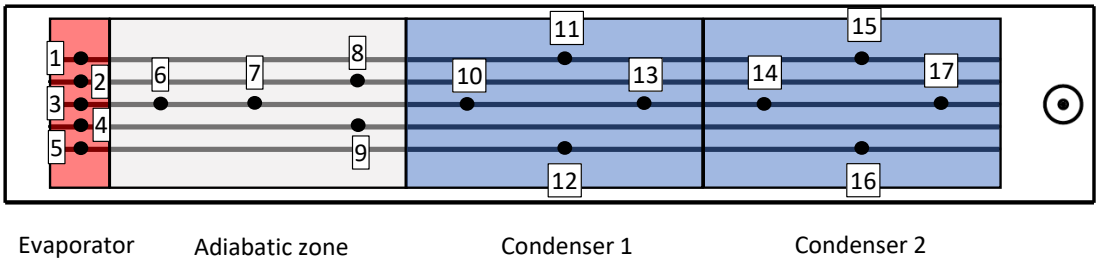

Figure 4.25: Thermocouple positions

To measure wall temperatures in the baseplate that are very close to the temperatures on the inner channel surface, the thermocouple grooves are designed 1.6 mm in depth. As shown in figure 4.26, this allows the thermocouple tips to be installed very close to the inner channel surfaces. The grooves have a rounded bottom to enable a good contact surface between the aluminum and the thermocouple tips. The grooves are 0.3 mm wide. This allows very small gaps to the thermocouples that have a diameter of 0.25 mm. A schematic cross-sectional drawing of a thermocouple installed in a groove is shown in figure 4.26.

The electrical power measurement consists of voltage and current measurement. The

voltage measurement is done with a parallel circuit to the heater to avoid measuring the voltage drop in the cables. Therefore, the voltage measuring circuit is attached directly to the positive and negative poles of the heater. The actual voltage reading is done with a NI 9219 universal measurement module programmed to voltage measurement in the range of $\pm$65 V.

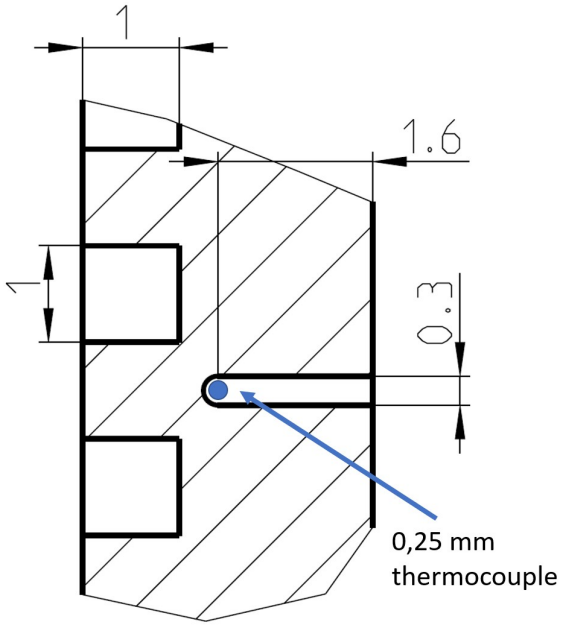

Figure 4.26: Thermocouple in groove of baseplate

The current measurement is done with a shunt resistor of 0.01 Ohm in series to the heater. The shunt resistor causes a voltage drop that is proportional to the current through the heater. The voltage drop across the shunt resistor is measured with a parallel circuit and a NI 9219 module, programmed to voltage measurement with a range of $\pm$15 V.

The full measurement chains of both thermal and electrical measurement systems are calibrated. More details can be found in appendix 10.2.

The purpose of the measurements with the high-speed camera (Photron Fastcam SA3) is to observe the flow and to detect bubbles for an evaluation of the bubble nucleation rate. As the bubbles are nucleated in the evaporator area, the camera is focused on this zone. Figure 4.27a shows the schematic setup of the camera system. On the left-hand side in the figure, the baseplate containing the PHP channels can be seen. The channels are covered on the right-hand side by the glass plate. The optical axis of the camera is

perpendicular to the baseplate, allowing for an undistorted image of the channel side of the baseplate. The lighting is located on both sides of the camera at an approximate angle of 45° to the optical axis. The lighting consists of LED-stripes that illuminate the full channel structure. The LED-modules are covered by a diffusive layer to uniformly light the baseplate. Nevertheless, the middle section of the image receives more light as the border areas, as the beams from the two light sources overlap here. The resulting image can be seen in figure 4.27b. The camera is set to 1000 frames per second with a shutter speed of 1/2500 s in all recordings. Approximately 5 s can be recorded in one take until the internal flash memory is full and the video needs to be transferred to the recording computer.

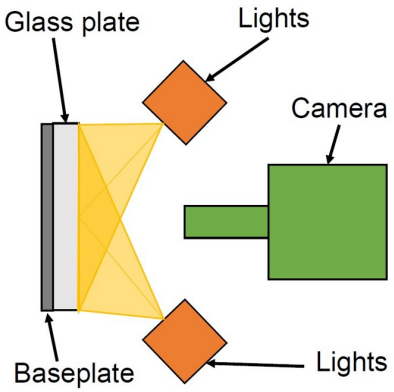

(a) Schematic camera setup with lights

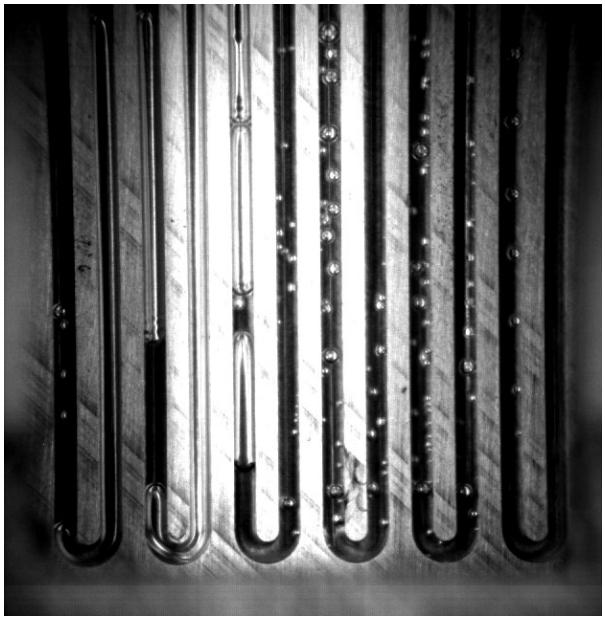

(b) Example image of evaporator

Figure 4.27: Image recording setup

4.3 Evaluation of bubble nucleation rate

To estimate bubble nucleation rates, an algorithm that comprises two main steps is used: Firstly, bubbles are detected in each frame. Secondly, the algorithm links the bubbles of each frame, so bubbles that already existed in one frame can be tracked and newly formed

bubbles can be detected.

In step one, the detection, the region of interest must be found for each new video. The video shows the full evaporator section, including the channel bends at the end of the PHP. Therefore, six separate channel segments can be identified in a video frame; each presenting an own region of interest that needs to be extracted. Figure 4.28 shows the extraction of one of the channel segments as an example.

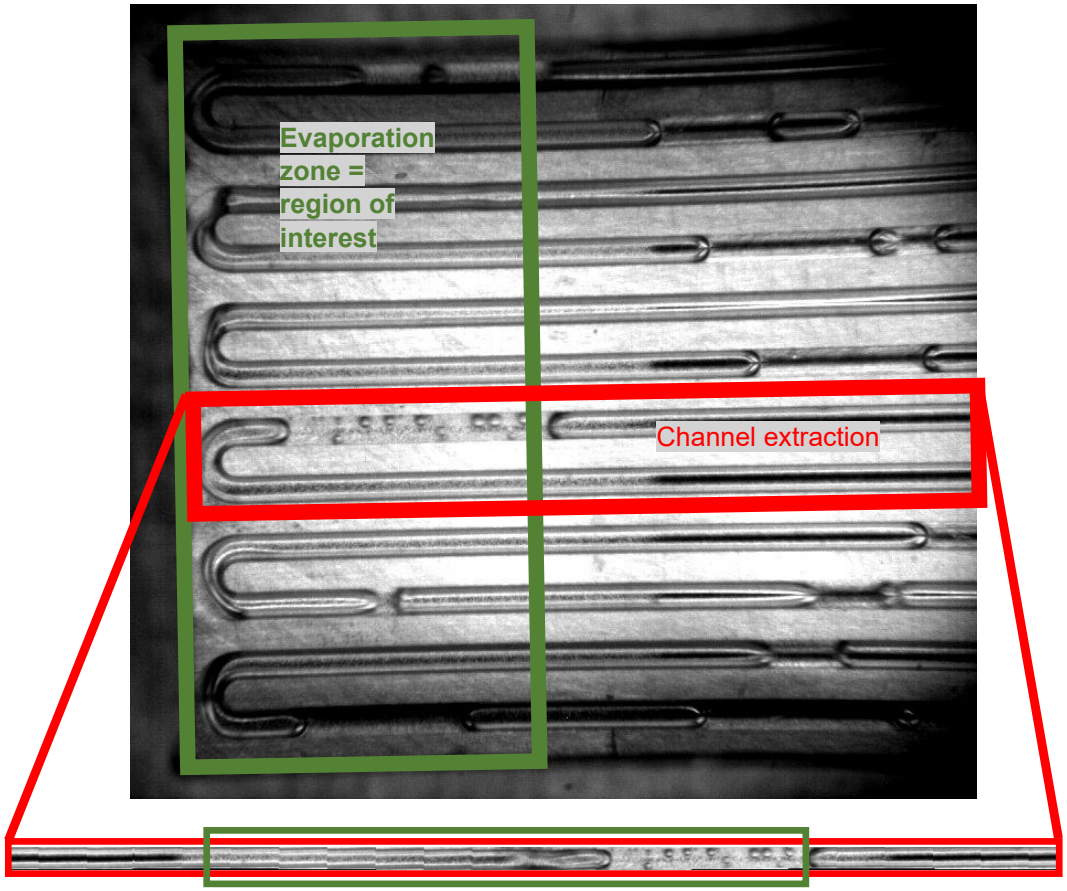

Figure 4.28: Channel extraction and region of interest

The positions of the channel segments are constant during one video and can also be the same for several videos recorded in a row. However, when the test setup or camera is moved in between two experiments, the position of the channels is not exactly the same anymore. Therefore, some key positions need to be marked manually for each video or a

batch of videos that can be used by the algorithm to identify the position of all channel segments. Each channel segment contains a curved section and two straight sections. To create an appropriate form for the detection algorithm, the curved section is uncoiled by coordination transformation to translate it into a straight section. The two straight channel sections with the uncoiled curved section in between can now be joined together to one long straight channel image. The result is depicted in the lower part of figure 4.28.

Each channel segment of a frame is transformed equally, and the six resulting straight channel images are passed on to the detection algorithm individually. To reduce the data that is processed, only the middle fraction of each channel segment is passed on to the detection algorithm. The middle section is slightly larger than the evaporator section, therefore, it is the relevant area for bubble nucleation. In figure 4.28, it is marked as the green area.

In the bubble detection step, the uncoiled input channel images are improved by several image enhancement methods to eliminate noise and improve contrast at the phase boundaries. The first processing step is a background subtraction. For this step, a plain image of the background without any phase boundaries or flow was recorded. This is done for each set of videos that have a common orientation of camera to test setup. In the background image, the channel segments are identified and uncoiled equally as for the video frames. Each background channel segment is handed on to the detection algorithm together with the video frame that is analyzed. After the background subtraction, the contrast is enhanced locally. To explain the enhancement procedure, a coordinate system is introduced for the channel segments in figure 4.29. The x-axis is defined as parallel to the channel direction. The y-axis is defined perpendicular to the channel direction. The image is split along each pixel of the x-axis into pixel columns parallel to the y-axis. For each pixel column a local enhancement factor was calculated that re-defines the gray scale values, so the maximum contrast is used.

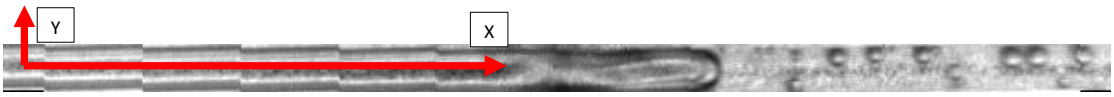

Figure 4.29: Channel segment coordinate system

The analysis yields an unsteady curve of the enhancement factor with respect to the x-position. The curve of the enhancement factor over x is smoothed with a moving-average filter. The enhancement factors are applied locally to the pixel columns. As contrast enhancement increases the noise level of the image, an adaptive 2D low-pass Wiener filter

is used for noise reduction.

The difference between the original image and the enhanced image can be seen in figure 4.30. The first (top) image in the figure shows the original image after the extraction of the region of interest. The second image shows the frame after image enhancement. In the next step, the enhanced gray scale image is converted into three different binary images. Each binary image has a different threshold value. 30, 100, and 170 have proven to be adequate threshold values for this procedure. In each binary image, different bubbles are visible, because their phase boundaries are dark and below the gray scale threshold value. The core of the bubble is bright and above the threshold value. Depending on local conditions, the bubble can only be clearly distinguishable in one of the binary images or in multiple binary images.

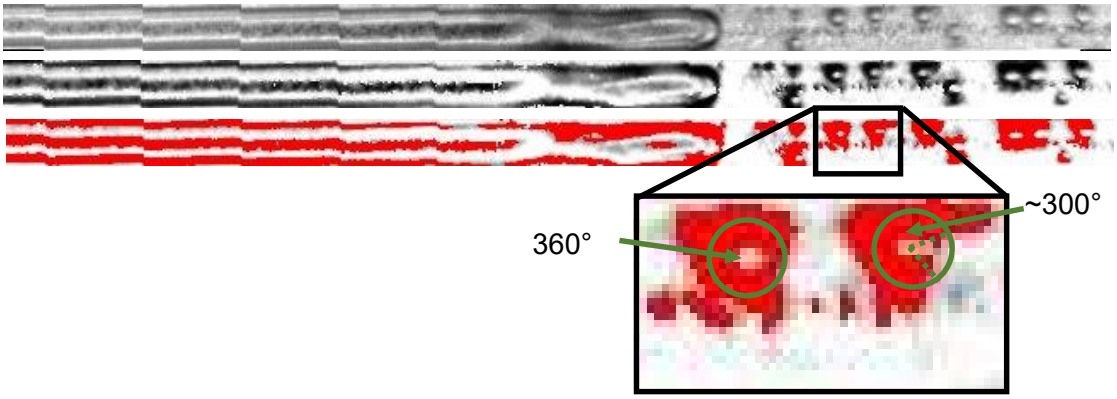

Figure 4.30: Channel image processing and bubble detection

The third image in figure 4.30 shows one of the binary images as an example. In this case, the threshold value of 170 was applied and the red pixels were below the threshold. The red pixels are marked for further processing. The binary image is analyzed for connected groups of red pixels. Each pixel group is then analyzed separately. All pixel groups with less than ten pixels are not analyzed further, because a bubble cannot be detected reliably here. For each pixel group, a circle is fitted to the coordinates of the red pixels using the method of least squares. The result is an idealized circle line with a radius value and center coordinates.

For each red pixel of a group, the distance to the idealized circle line is calculated. The distances of all red pixels to the circle line are added up and divided by the number of pixels. This yields a value for the quality of the fit. If the quality value is above a certain threshold, the fit quality is insufficient, and no circle (and, thus, no bubble) is detected.

The pixel group is then discarded. The fit quality is the first filter criterion that is applied to the pixel groups.

The second filter criterion takes the covered angle into account. In most cases not the entire circle line is covered by the red pixels, but only a fraction of the full angle. In the example image in figure 4.30, two pixel groups are analyzed further. The left image shows the rare perfect example of a 360° circle. The right image shows an open circle, covering only 300°. The smaller the covered angle is, the less likely it is that a bubble is located here in the image. Thus, a filter is applied, excluding all pixel groups that have less than 60° of coverage. The limit value has proved to avoid misdetections reliably.

The third filter excludes all pixel groups that have an idealized circle radius of more than a fourth of the channel width. This allows bubbles to be detected up to a diameter of half of the channel width. As the main focus of the analysis is to detect newly introduced bubbles, bubbles that are larger than this threshold can be discarded, because bubbles are always introduced as small bubbles before they start to grow. Excluding larger bubbles also reduces the risk of false detections.

The bubble detection yields a list of detected bubbles with radius values and center coordinates for each of the three binary images derived from one gray scale frame of a channel segment. Some bubbles only appear in one of the binary images, but others can be detected in multiple binary images. Therefore, the three lists are merged, and multiple entries of the same bubble need to be removed. This is done by analyzing the bubble center coordinates and eliminating bubbles in close proximity. Close proximity is confirmed when the distance between two center points is smaller than the sum of their radii.

After removing the redundant detections, a list of all the bubble detections remains. The result can be plotted by inserting the detected bubbles as red circles into the original gray scale image. For figure 4.30, the result can be seen in figure 4.31. The top image in the figure shows the original image without any detections and the bottom image shows the same image with the detected bubbles. It can be seen that all the small bubbles were detected. On the right-hand side of the image are two larger bubbles that were not detected. In this case, they were excluded in the filtering process due to their radius being above the threshold value. These bubbles were detected several frames ago and are, therefore, already accounted for.

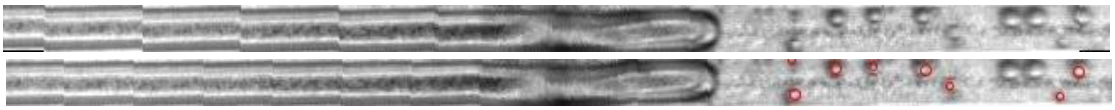

Figure 4.31: Bubble detection result

The described bubble detection is done for each frame of the channel segment. Therefore, it creates a list of bubbles for each time step. Most bubbles are detected in multiple frames because they persist within the region of interest, only slightly shifting their position with each frame. To only count the bubbles that are newly introduced, the bubbles need to be allocated to their predecessors in the previous frame if existent. For this, a tracking algorithm is implemented. This is the second main step in the evaluation of the bubble nucleation rate. For the allocation, a 2D motion tracking algorithm is implemented.

For the tracking algorithm, a few definitions are introduced: In a frame (time step), n_t bubbles are found. t is the number of the time step. The pixel positions of the bubbles at time step t are defined within the coordinate system described in figure 4.29 by

$$\vec{p}_{i,t} = \begin{pmatrix} x_{i,t} \\ y_{i,t} \end{pmatrix}, \tag{4.12}$$

where i is the bubble number, ranging from 1 to n_t. The velocity vector in this time step is defined by

$$\vec{v}_{i,t} = \begin{pmatrix} u_{i,t} \\ w_{i,t} \end{pmatrix} = f_{rec} s_{scale} (\vec{p}_{i,t} - \vec{p}_{i,t-1}), \tag{4.13}$$

where $\vec{p}_{i,t}$ is the bubble position at the current time step and $\vec{p}_{i,t-1}$ is the bubble position at the previous time step. f_{rec} is the recording frequency of the camera in Hertz. s_{scale} is the scaling factor that contains the scale of the current camera view. It is the physical distance per pixel and, thus, translates the velocities from pixel per second into meters per second. Based on the locations and velocities of the bubbles in the previous time step, the positions of the bubbles in the current time step $\vec{p}_{i,t,prediction}$ are predicted by

$$\vec{p}_{i,t,prediction} = \vec{p}_{i,t-1} + \frac{1}{f_{rec} s_{scale}} \vec{v}_{i,t-1}. \tag{4.14}$$

The closest matches between the predicted positions and the actual positions of the current time step are searched and allocated if the distance between the predicted position and the actual position is below a threshold. The threshold is defined as the double value of

the maximum pixel velocity of all the bubbles in the previous step. The pixel velocity of a bubble from the previous step is calculated by

$$\vec{v}_{i,t-1,pixel} = \frac{1}{f_{rec} s_{scale}} \vec{v}_{i,t-1}. \tag{4.15}$$

This enables direction reversal to be recognized by the tracking algorithm. For very small velocities, the calculated tolerance is also very small. Thus, the algorithm would fail to allocate most bubbles. Therefore, a minimum tolerance of 10% of the channel width is defined. The maximum tolerance is set to the channel width to avoid misdetection at high velocities. At high velocities, flow reversal is very unlikely, therefore the tolerance does not have to increase any further here.

The allocation of bubbles across multiple time steps is done via identity numbers that are given to the bubbles. The first and second time steps are special cases in the algorithm. In the first time step, no previous bubbles are available, thus, all detected bubbles obtain a new ID number. As not all of these bubbles are actually nucleated in this time step, the first time step is not taken into account for bubble nucleation counting. In the second time step, previous bubbles are available but without any velocity information. Therefore, the bubbles are all assumed to have zero velocity.

After all the bubbles from the previous time step have been allocated where possible, the remaining unallocated bubbles in the current time step are recognized as new bubbles that are given new IDs. If a bubble from the previous time step cannot be allocated anymore in the current time step, it is assumed to have vanished. In special cases, a bubble that is not detected in a single time step reappears one step later. Then, a new bubble identity would be falsely allocated, leading to a higher bubble nucleation rate than factually accurate. To avoid this error, the bubble tracks are virtually continued for one more step. If the bubble then reappears, the existing ID of the continued bubble is allocated. If the bubble does not reappear in the next step, the bubble track is ended at the time step when it first vanished.

The tracking algorithm yields bubble tracks that contain a bubble ID, the time step the bubble first appeared in, and the time step when the bubble vanished. From this information, the lifetime of the bubble track can be calculated. Correctly tracked bubbles appear in multiple time steps in a row before they disappear. Falsely detected bubbles due to image artefacts usually appear for only one or a few time steps and disappear again very quickly. Therefore, a filter is implemented that excludes bubble tracks that are shorter than five time steps. This proved to be a suitable limit, as shorter tracks were found to be misdetections.

To conclude, the algorithm enables to count the newly introduced bubble IDs within the recorded time. The bubble nucleation rate for the analyzed channel segment is then calculated by dividing the total count of newly introduced bubble IDs by the recording time

of the video. This yields the number of bubbles introduced per second on average. The six channel segments of a video showing the evaporator section are analyzed independently and all result in an individual bubble nucleation rate. The bubble nucleation rates of the channel segments are then added up for the resulting total bubble nucleation rate of the video file.

4.4 Thermal characterization

The measurement procedures necessary for thermal characterization are described in this chapter. Consequently, thermal losses that arise from heat exchange with the surroundings are analyzed and accounted for. The required post-processing of the measurement data is also explained here.

All test setups are insulated to the surroundings as well as possible. The stainless-steel frame, especially the back side that contains the heater and coolers is thickly insulated and has very little heat exchange with the surroundings. However, all setups have a glass cover plate, that is necessary for optical access of the PHP. The glass plate cannot be insulated any further and, therefore, has the highest heat exchange with the surroundings. It must be measured depending on the boundary conditions and compensated in the thermal resistance calculation. To compensate the heat exchange with the surroundings, the unfilled test setups are used for a reference measurement. The unfilled setups have a constant thermal resistance if perfectly insulated, as only thermal conduction in aluminum is applicable. Therefore, the first step is to measure the thermal resistance of the fully insulated unfilled PHP for each test setup. In addition to the permanent insulation on the backside and steel frame, insulation is added at the glass window for this measurement. At 20°C condenser temperature and approximately 5 W of electrical power loss at the heater, the thermal resistances of all three test setups are measured. As this is the reference thermal resistance, it is referred to as $R_{th,true}$ and calculated by

$$R_{th,true} = \frac{\bar{T}_{evap} - \bar{T}_{cond}}{\dot{Q}_{in}}, \tag{4.16}$$

where $\bar{T}_{evap}$ is the average evaporator temperature calculated as the arithmetic average of the readings of thermocouples 1 to 5 as marked in figure 4.25. $\bar{T}_{cond}$ is the average condenser temperature, calculated as the arithmetic average of thermocouples 10 to 17 in figure 4.25. All thermocouple readings are time averaged values, that are the mean value of a 3 min interval in steady-state condition. $\dot{Q}_{in}$ is the input heat flow in the evaporator section. In case of the fully insulated measurements, $\dot{Q}_{in}$ is assumed to be equal to the heater's electrical power loss P_{heater}. The measured reference thermal resistances $R_{th,true}$

for test setups 1, 2, and 3 are 4.35 K/W, 4.22 K/W, and 4.38 K/W, respectively. They are also controlled by a second measurement at 10 W heater power loss.

To quantify how much heat is exchanged with the surroundings for a non-insulated glass window, the insulation of the window is removed again on all test setups. With the unfilled PHP, several boundary conditions are now applied to compare the results with the $R_{th,true}$ values. Therefore, all applicable condenser temperatures are applied to each test setup. The heater power is varied from zero to a maximum value, including one intermediate step. The maximum value is set for the evaporator temperature to reach the relevant maximum value in subsequent experiments. Thus, the full temperature range at the evaporator is covered. The evaporator and condenser mean temperatures $\bar{T}_{evap}$ and $\bar{T}_{cond}$ are calculated for the steady-state condition. Thus, the applicable input heat flow in the evaporator area is calculated by

$$\dot{Q}_{in} = \frac{\bar{T}_{evap} - \bar{T}_{cond}}{R_{th,true}}. \tag{4.17}$$

The difference between the calculated heat flow $\dot{Q}_{in}$ and the measured electrical power P_{heater} is the effective heat exchange with the surroundings $\dot{Q}_{amb}$, and is defined as the heat flow from the surroundings to the test setup. For the calculation of the thermal resistance of an operating PHP, this means that $\dot{Q}_{amb}$ has to be added to the measured electrical power P_{heater}. The corrected thermal resistance $R_{th,corr}$ is, thus, calculated by

$$R_{th,corr} = \frac{\bar{T}_{evap} - \bar{T}_{cond}}{P_{heater} + \dot{Q}_{amb}}, \tag{4.18}$$

where $\dot{Q}_{amb}$ depends on the boundary conditions and is, therefore, a function of the condenser temperature and the evaporator temperature. The ambient temperature is assumed to be constant due to a temperature-controlled laboratory environment. Figure 4.32 shows the calculated $\dot{Q}_{amb}$ values for test setup 1 for various boundary conditions. The measurement and determination of $\dot{Q}_{amb}(\bar{T}_{evap}, \bar{T}_{cond})$ function was separately done for test setups 2 and 3 as well.

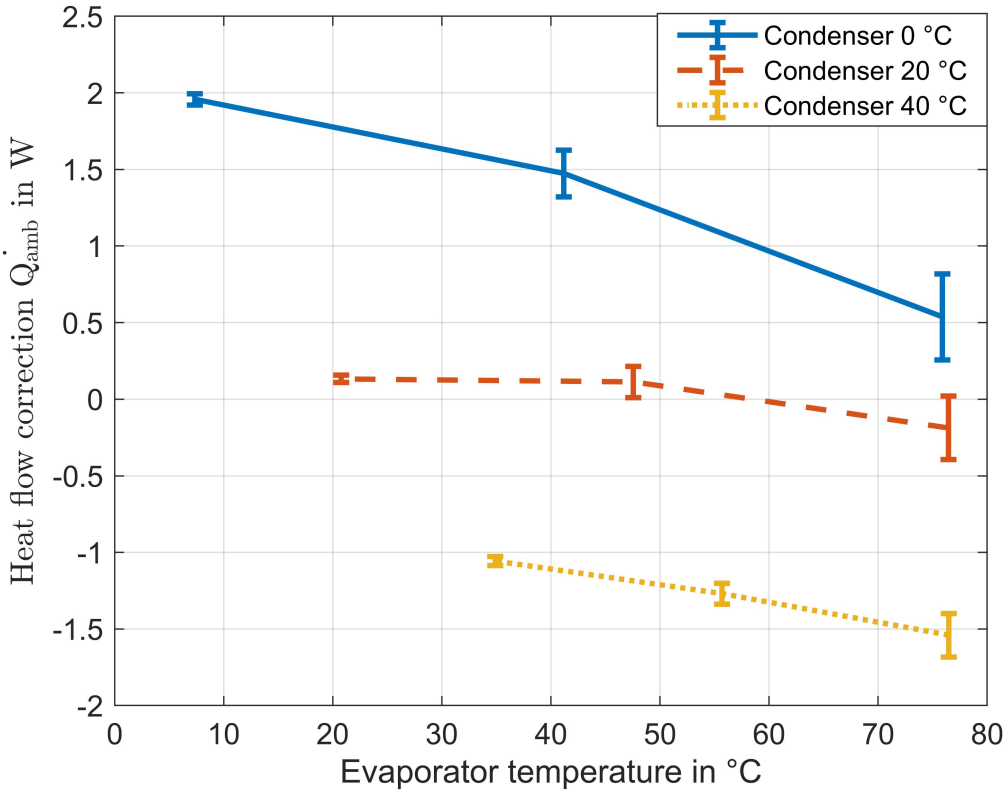

Figure 4.32: Correction of heat flow for test setup

4.5 Error analysis

4.5.1 Temperature measurement

The measurement uncertainty for a single thermocouple after the calibration, including the interpolation error, is ± 0.16 K. The associated derivation of the measurement uncertainty can be found in appendix 10.2. The calibration and interpolation error can be considered as systematic errors. The random error in the temperature measurement can be neglected. Therefore, the probability distribution of the error is uniform in the full possible interval of ± 0.16 K. According to GUM [66], the expanded measurement uncertainty U_{error} for a uniformly distributed error probability in the interval from $-f_s$ to $+f_s$ can be calculated

by

$$U_{error} = \frac{2f_s}{\sqrt{3}}. \tag{4.19}$$

The equation includes a coverage factor of 2 that ensures the real value to be within the calculated expanded measurement interval with a probability of 95%.

For a thermocouple, this yields an expanded measurement uncertainty of $\pm$0.185 K. From several thermocouples, average values are calculated for the evaporator area and the condenser area. The average temperature in the evaporator area T_{evap} is calculated by

$$\bar{T}_{evap} = \frac{1}{5}(T_1 + T_2 + T_3 + T_4 + T_5). \tag{4.20}$$

To calculate the measurement uncertainty for $\bar{T}_{evap}$, the law of error propagation must be applied. Gaussian error propagation was used, where the standard deviation of an output quantity $y(x_1, x_2, ...x_n)$ is calculated by

$$U_y = \sqrt{\sum_{i=1}^{n} (\frac{\delta y}{\delta x_i})^2 U_{x_i}^2}, \tag{4.21}$$

where U_{x_i} are the uncertainties of the input quantities. If the Gaussian error propagation (equation 4.21) is applied to equation 4.20 for calculating the uncertainty of $\bar{T}_{evap}$, it yields

$$\begin{aligned} U_{\bar{T}_{evap}} &= \sqrt{(\frac{\delta \bar{T}_{evap}}{\delta T_1})^2 U_{T_1}^2 + (\frac{\delta \bar{T}_{evap}}{\delta T_2})^2 U_{T_2}^2 + (\frac{\delta \bar{T}_{evap}}{\delta T_3})^2 U_{T_3}^2 + (\frac{\delta \bar{T}_{evap}}{\delta T_4})^2 U_{T_4}^2 + (\frac{\delta \bar{T}_{evap}}{\delta T_5})^2 U_{T_5}^2} \\ &= \sqrt{(\tfrac{1}{5})^2 U_{T_1}^2 + (\tfrac{1}{5})^2 U_{T_2}^2 + (\tfrac{1}{5})^2 U_{T_3}^2 + (\tfrac{1}{5})^2 U_{T_4}^2 + (\tfrac{1}{5})^2 U_{T_5}^2} \\ &= \sqrt{\tfrac{1}{25}((\pm 0.185K)^2 + (\pm 0.185K)^2 + (\pm 0.185K)^2 + +(\pm 0.185K)^2 + (\pm 0.185K)^2)} \\ &= \pm 0.08 \text{ K.} \end{aligned} \tag{4.22}$$

The average condenser temperature $\bar{T}_{cond}$ is calculated by

$$\bar{T}_{cond} = \frac{1}{8}(T_{10} + T_{11} + T_{12} + T_{13} + T_{14} + T_{15} + T_{16} + T_{17}). \tag{4.23}$$

Similarly, the Gaussian error propagation is applied to equation 4.23 which yields a $U_{\bar{T}_{evap}}$ of $\pm$0.07 K.

4.5.2 Heat flow

As derived in chapter 4.4, the input heat flow in the evaporator section $\dot{Q}_{\mathrm{in}}$ is calculated by

$$\dot{Q}_{in} = P_{heater} + \dot{Q}_{amb}. \tag{4.24}$$

Therefore, the errors of P_{heater} and $\dot{Q}_{\mathrm{amb}}$ must be found, before the error of $\dot{Q}_{\mathrm{in}}$ can be caulculated. P_{heater} is calculated by

$$P_{heater} = U_{heater} I_{heater}, \tag{4.25}$$

where U_{heater} is the measured voltage drop across the heater and I_{heater} is the measured current through the heater. The maximum difference of the current sensor reading to the reference sensor reading is 0.49% in the measurement range. The uncertainty of the current reference sensor is 0.05% [67]. The errors are assumed to be systematic. The full expanded current uncertainty is, therefore, calculated by

$$u_{I_{heater}} = 2 * \frac{\pm 0.49\% + \pm 0.05\%}{\sqrt{3}} = \pm 0.624\%. \tag{4.26}$$

The voltage measurement via the NI-module has an accuracy of $\pm 0.3\%$ according to the datasheet [68]. Assuming a systematic error, the voltage uncertainty $u_{U_{\mathrm{heater}}}$ is

$$u_{U_{heater}} = 2 * \frac{\pm 0.3\%}{\sqrt{3}} = \pm 0.346\%. \tag{4.27}$$

Applying the Gaussian error propagation to equation 4.25, the relative uncertainty of the electrical power is calculated by

$$u_{P_{heater}} = \sqrt{u_{I_{heater}}^2 + u_{U_{heater}}^2} = \pm 0.714\%. \tag{4.28}$$

For the fully insulated unfilled test setup, the thermal resistance $R_{\mathrm{th,true}}$ is measured as in chapter 4.4. $R_{\mathrm{th,true}}$ is calculated by

$$R_{th,true} = \frac{\bar{T}_{evap} - \bar{T}_{cond}}{P_{heater}}. \tag{4.29}$$

The uncertainty is calculated by

$$U_{R_{th,true}} = \sqrt{(\frac{1}{P_{heater}})^2 * (U_{\bar{T}_{evap}}^2 + U_{\bar{T}_{cond}}^2) + (\frac{\bar{T}_{evap} - \bar{T}_{cond}}{P_{heater}^2})^2 * U_{P_{heater}}^2}. \tag{4.30}$$

For setups 1, 2, and 3 this yields uncertainties for $R_{th,true}$ of ± 0.0627 K/W, ± 0.0376 K/W, and ± 0.0396 K/W, respectively.

$\dot{Q}_{amb}$ is calculated by

$$\dot{Q}_{amb} = \frac{\bar{T}_{evap} - \bar{T}_{cond}}{R_{th,true}} - P_{heater}. \tag{4.31}$$

For each measured point with the unfilled PHP (non-insulated window), the uncertainty of $\dot{Q}_{amb}$ is calculated by

$$U_{\dot{Q}_{amb}} = \sqrt{\frac{1}{R_{th,true}^2}(U_{\bar{T}_{evap}}^2 + U_{\bar{T}_{cond}}^2) + (\frac{\bar{T}_{evap} - \bar{T}_{cond}}{R_{th,true}^2})^2 U_{R_{th,true}}^2 + U_{P_{heater}}^2}. \tag{4.32}$$

The error bars of figure 4.32 are calculated from this equation. Each data point of the unfilled measurements is associated with a different error bar according to the calculated uncertainty. For data points in between the measured points, the expectancy and uncertainty values are both interpolated linearly between the known data points. Both $\dot{Q}_{amb}$ and $U_{\dot{Q}_{amb}}$ can, therefore, be regarded as functions of the test setup number, the condenser temperature, and the evaporator temperature.

4.5.3 Error for thermal resistance

In the measurements with the filled PHPs, the temperatures and electrical powers are measured. The thermal resistance for the measured data points can then be calculated by

$$R_{th} = \frac{\bar{T}_{evap} - \bar{T}_{cond}}{P_{heater} + \dot{Q}_{amb}}. \tag{4.33}$$

The uncertainty of R_{th} is calculated by

$$U_{R_{th}} = \sqrt{(\frac{1}{P_{heater} + \dot{Q}_{amb}})^2 (U_{\bar{T}_{evap}}^2 + U_{\bar{T}_{cond}}^2) + (\frac{\bar{T}_{evap} - \bar{T}_{cond}}{(P_{heater} + \dot{Q}_{amb})^2})^2 (U_{P_{heater}}^2 + U_{\dot{Q}_{amb}}^2)}. \tag{4.34}$$

Each data point in the measurement results is associated with an individual error bar according to the calculated uncertainty.

5 Experimental Results

5.1 Overview of different test cases

The associated results of setups and procedures explained in chapter 3 are shown here. The chapter starts by showing the general transient behavior of the investigated PHPs (section 5.2). The following sections show results in quasi-steady state split into different influencing factors. Not all the available results are presented here. The chapter rather focuses on the influences detected in the results. A summary of boundary conditions presented in this work can be found in tables 5.1 and 5.2. Boundary conditions are associated with a test case number that is used as a reference. The influencing factors presented here are heat flow (section 5.3), gravity (section 5.4), filling ratio (section 5.5), condenser temperature (section 5.6), and evaporator surface roughness (section 5.7). From here on, vertical bottom heated is abbreviated to vertical BH.

Test case nr.	Orientation	Test setup	Filling ratio	Condenser temperature
1	Vertical BH	1	70%	0° C
2	Vertical BH	1	70%	20° C
3	Horizontal side	1	70%	20° C
4	Vertical BH	1	70%	40° C
5	Vertical BH	1	50%	0° C
6	Vertical BH	1	50%	20° C
7	Vertical BH	1	50%	40° C
8	Vertical BH	1	30%	0° C
9	Vertical BH	1	30%	20° C
10	Vertical BH	1	30%	40° C

Table 5.1: Overview of all test cases with setup 1

Test case nr.	Orientation	Test setup	Filling ratio	Condenser temperature
11	Vertical BH	2	70%	20° C
12	Vertical BH	2	70%	40° C
13	Vertical BH	2	50%	20° C
14	Vertical BH	2	50%	40° C
15	Vertical BH	2	30%	20° C
16	Vertical BH	2	30%	40° C
17	Vertical BH	3	70%	20° C
18	Vertical BH	3	50%	20° C
19	Vertical BH	3	30%	20° C

Table 5.2: Overview of all test cases with setups 2 and 3

5.2 Transient behavior

Testing follows a standardized procedure. Firstly, the thermostat is started to create a constant temperature in the condenser zone. When no temperature variation with respect to time is registered at the thermocouple readings of the PHP baseplate, the experiment is initiated. The heater is set to the desired first heat load. Starting at this point, which is defined as time $t=0$, figure 5.1 shows an exemplary test se quence. The start of the experiment is clearly visible at the point where the heater power rises from 0 W to 7 W. Accordingly, the average evaporator temperature rises steeply up to approximately 40°C. Here, the PHP starts to pulsate and a sudden small drop in evaporator temperature can be observed.

The pulsating motion of the PHP is highly unsteady. Therefore, the temperatures, especially in the evaporator section, are never completely constant for a PHP in operation. After some time, they usually fluctuate around a mean value. This is a quasi-steady state condition where effectively the mean value does not change anymore and the fluctuations around the mean value are stable. It can be noted that the amplitude of the fluctuations generally increases with increasing heater power. The quasi-steady state condition is used for evaluating the thermal behavior of the PHP. Therefore, the boundary conditions are kept constant until the quasi-steady state condition is reached. Then, the heater is set to the next intended power.

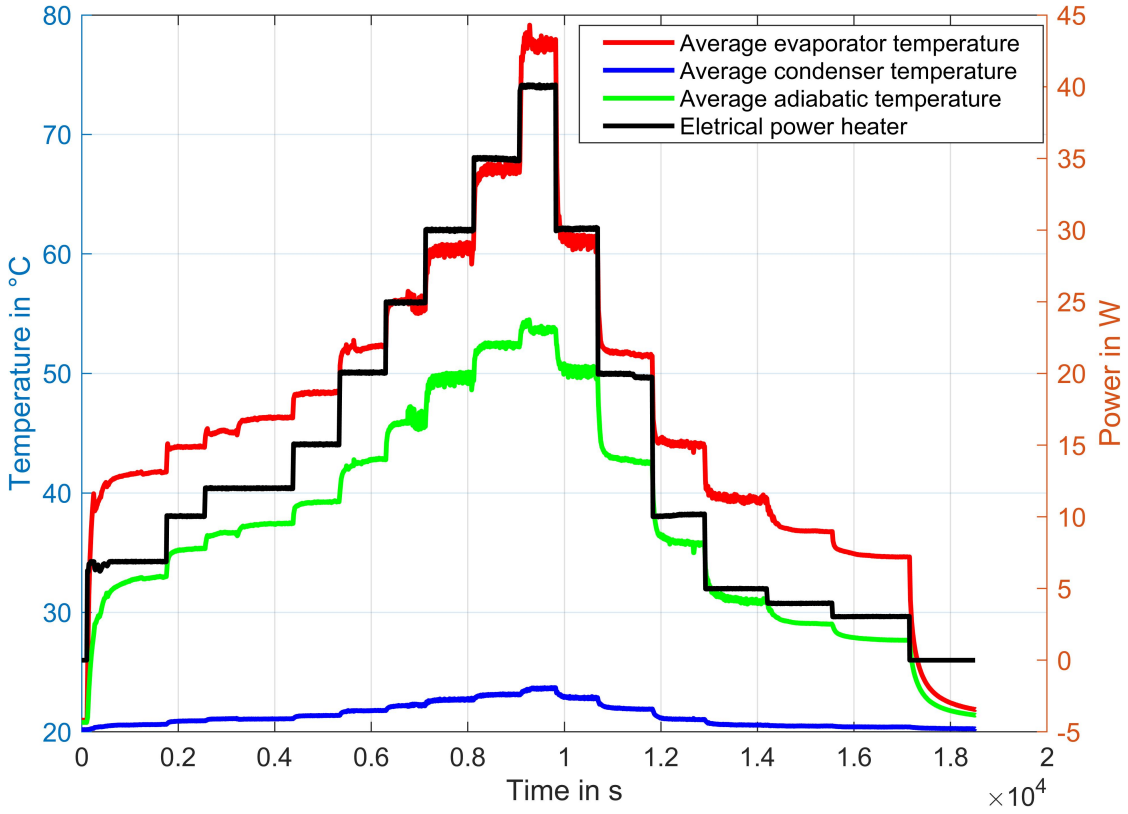

Figure 5.1: Power settings and rsulting transient temperatures in the experiments: test setup 1, vertical BH orientation, 70% filling ratio, 20◦C condenser temperature (test case 2)

The evaporator temperatures rise again until they reach the next stable level. The heater power is, thus, increased in steps until dry-out or the experimental limits are reached. The experimental limits are reached when the adiabatic temperature exceeds 55°C. The adiabatic temperature is assumed to be close to the saturation temperature of the refrigerant. The PHP is leak-tested up to the vapor pressure at 55°C. Therefore, this presents a reasonable limit. In the time plot, it can also be seen that the average condenser temperature slightly increases for high heat loads. The maximum value reached is usually around 23°C for a coolant inlet temperature of 20°C.

After reaching the maximum heater power, the power is reduced in steps to record the behavior for decreasing heat loads. The results for increasing and decreasing power show no significant difference. The only exception where a difference could occasionally be

observed is directly after dry-out was reached, followed by a fast shut down of the power, in order not to damage the setup. In this case, higher evaporator temperatures could be observed for decreasing power as compared to increasing power. This is due to the PHP still being in partial dry-out and not pulsating efficiently. Time and lower heater powers eliminate the partial dry-out and the PHP returns to normal operation.

Figure 5.2 shows the PHP start-up in detail. The power jump from 0 W to 10 W can be seen clearly in the plot. The evaporator temperatures react and increase rapidly. In this case, they reach a maximum value of 50°C, where the oscillating motion starts. The onset of the pulsation quickly removes heat from the evaporator area and transports it to the condenser section. Therefore, the PHP start-up leads to a fast decrease in evaporator temperature. The temperatures stabilize at around 43°C. Small fluctuations can also be seen after the start-up. At the maximum time displayed in figure 5.2, the quasi-steady state condition is reached.

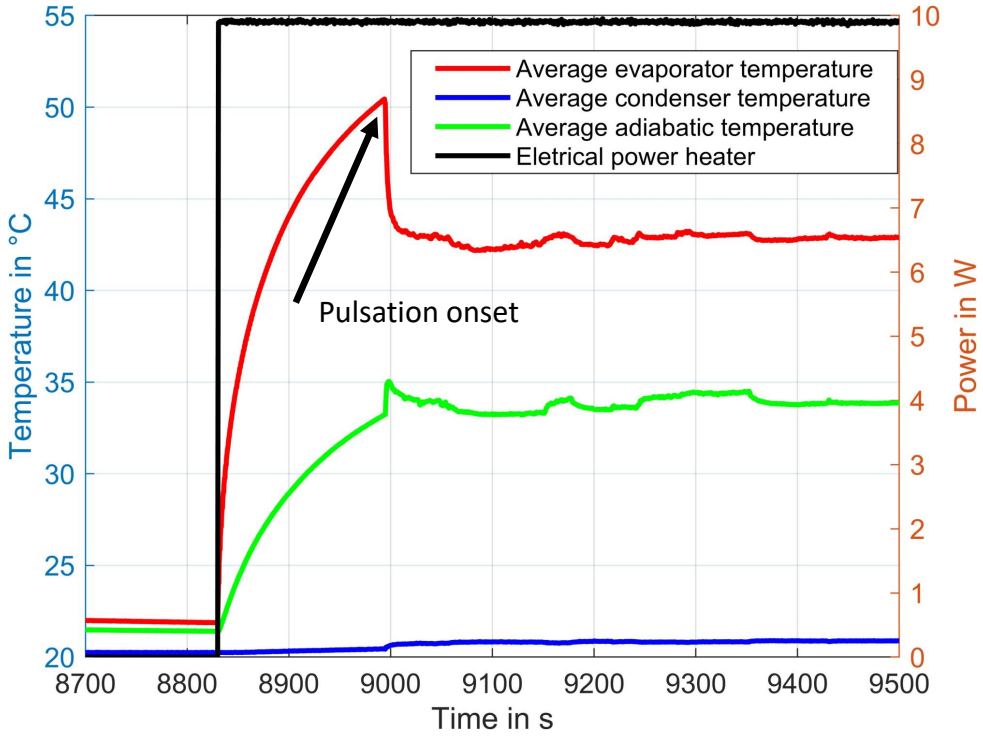

Figure 5.2: Startup characteristic of PHP for 10 W heater power: test setup 1, vertical BH orientation, 70% filling ratio, 20◦C condenser temperature (test case 2)

5.3 Effect of input heat flow on thermal resistance

The overall thermal resistance and the effective heat flow of the PHP is calculated as stated in chapter 4.4. Figure 5.3 shows the steady-state thermal resistances for different heat flow r ates. The filling ratio of 70% and the condenser temperature of 0° C were maintained constant for this experiment. The thermal resistance is highest for low heat flow r ates. At the lowest recorded heat flow of approximately 7 W, the thermal resistance was around 4.2 K/W. With the thermal resistance of the empty PHP being 4.35 K/W, the PHP is almost inactive in this point. The thermal resistance decreases with increasing heat flow until a minimum of 1.5 K/W is reached at 36 W. For a heat flow higher than 36 W, the thermal resistance increases slightly. The last stable point measured was at 46 W. A higher heat flow led to dry-out and, therefore, a rapid increase in evaporator temperature.

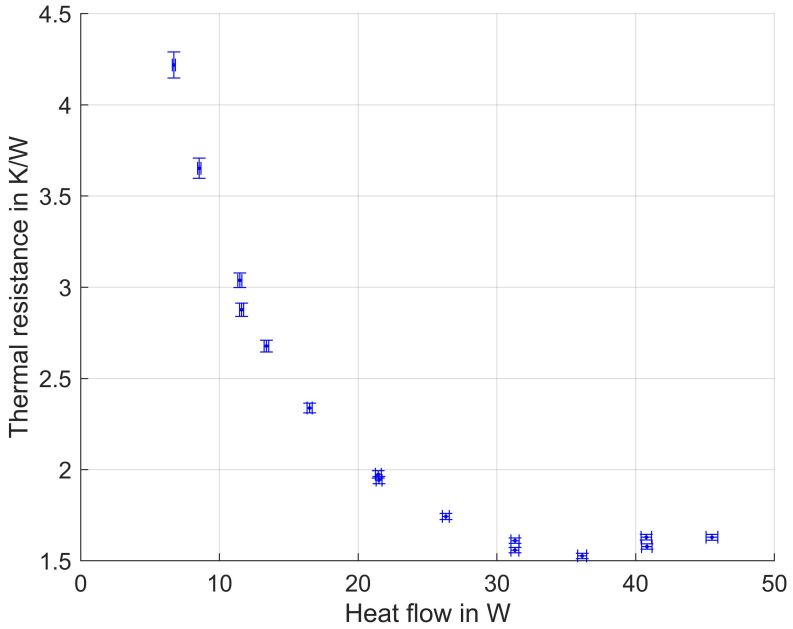

Figure 5.3: Thermal resistance of test setup 1 in vertical BH orientation for different heat loads at 0◦C condenser temperature and 70% filling ratio (test case nr. 1)

To visually observe the flow behavior and regimes, the PHP was recorded by a camera through the glass window. Figures 5.4 (evaporator area) and 5.5 (full PHP) show frames of the recordings at different heat flow rates. The frames give an indication of the differences that exist between 10 W heat flow on the left-hand side and 30 W heat flow on the

right-hand side. At 10 W the flow is dominated by bubble nucleation that happens at the bottom (evaporator section). The bubbles are small and rise in a channel to the topside of the liquid column in the channel. The pressure difference driving the bubbles is assumed to be small as the velocities that can be observed are rather low and the bubbles are hardly able to move any liquid slugs. It can also be observed that the left four channels and the right three channels are not active. Counting from the left-hand side, only channels 5 to 9 show bubble movement. In fact, the liquid seems to be pushed from the middle channels to the outer channels which are, consequently, completely filled with liquid. At 30 W (right-hand side), all channels show bubble movements and are, therefore, active. The liquid phase is distributed evenly and not concentrated on the outer channels anymore. The bubbles produced in the evaporator section grow to a larger size than for 10 W heat flow and the movements are faster. Therefore, the bubbles can push the liquid slugs to the topside of the baseplate and also into neighboring channels. The flow is characterized by direction changes and the typical chaotic movement of a PHP.

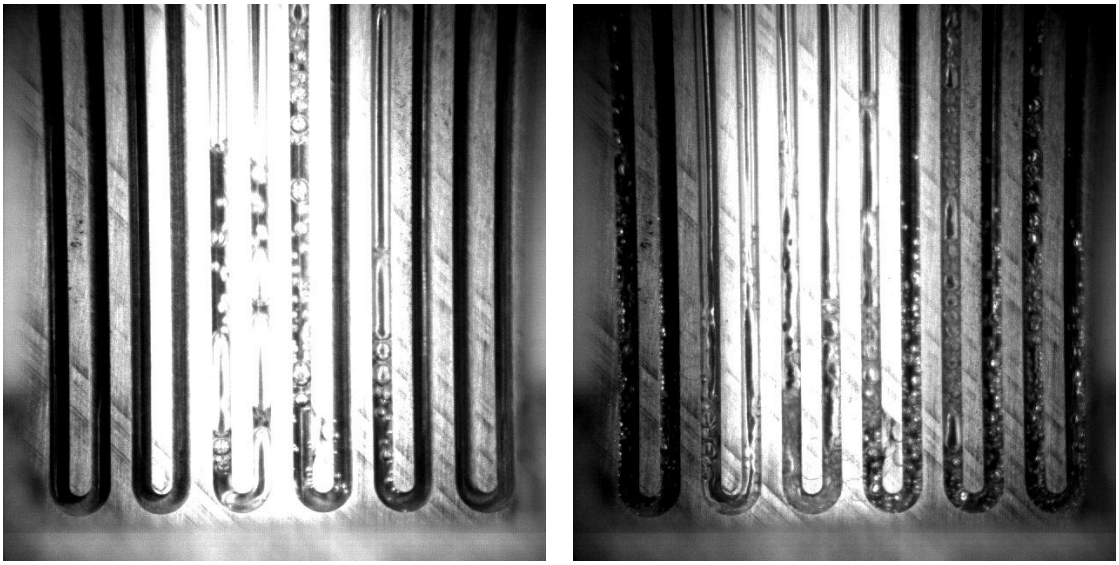

Figure 5.4: Flow comparison between 10 W (left) and 30 W (right) in the evaporator area for test setup 1 in vertical BH orientation at filling ratio 70% and 0◦C condenser temperature (test case nr. 1)

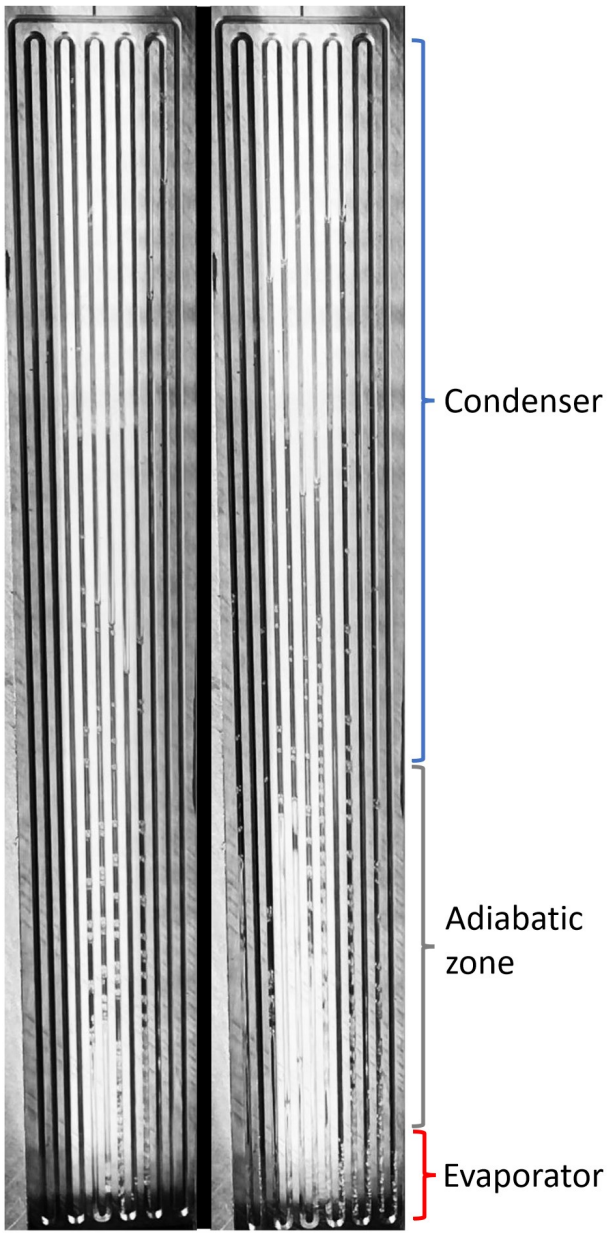

Figure 5.5: Flow comparison between 10 W (left) and 30 W (right) for test setup 1 in vertical BH orientation at filling ratio 70% and 0◦C condenser temperature (test case nr. 1)

5.4 Effect of orientation to gravity on thermal resistance

All three PHP test setups were tested in four different orientations to gravity. The orientations are shown in figure 5.6. The PHP is heated in the red section and cooled in the blue section in each orientation.

Orientations B and D did not operate in all boundary conditions. The PHP dried out immediately in the evaporator section at the smallest tested heat flow of 5 W. The PHP function was tested in these orientations for all three roughness values (all test setups), 0°C, 20°C, and 40°C condenser temperature, and 30%, 50%, and 70% filling ratio with the same result.

Orientations A and C were operating in all tested conditions but with different dry-out limits. While orientation A had rather high dry-out limits, the dry-out limit was always reached at lower heat flow rates in orientation C for all test setups, filling ratios, and condenser temperatures.

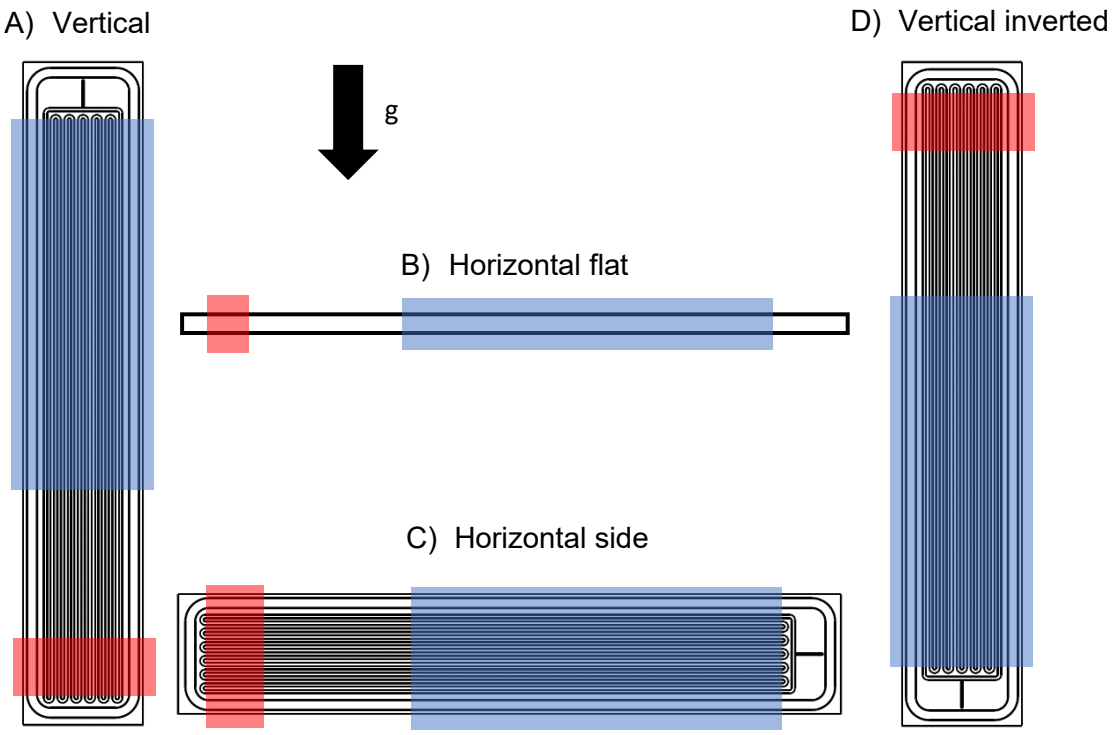

Figure 5.6: PHP orientations to gravity

Figure 5.7 shows an example comparison between horizontal side and vertical bottom-heated orientation. The example is recorded with test setup 1 at 70% filling ratio and 20°C condenser temperature. While dry-out was reached at a heat flow larger than 15 W for the horizontal side orientation (orientation C), the vertical orientation (A) did not reach dry-out condition for heat flow rates up to 40 W. For horizontal side orientation, the PHP exhibited the optimum thermal resistance between 7 W and 10 W with values of approximately 2.5 K/W. For vertical orientation, the optimum thermal resistance is much lower with a value of around 1.25 K/W at considerably higher heat flow rates of 30 to 35 W. The two thermal resistance curves intersect at around 8 W to 9 W. For heat flow rates below the intersection, the thermal resistance is slightly lower in horizontal side orientation compared to vertical orientation. For a higher heat flow, the vertical orientation yields lower thermal resistance values. The same qualitative differences could be observed for other filling ratios and condenser temperatures.

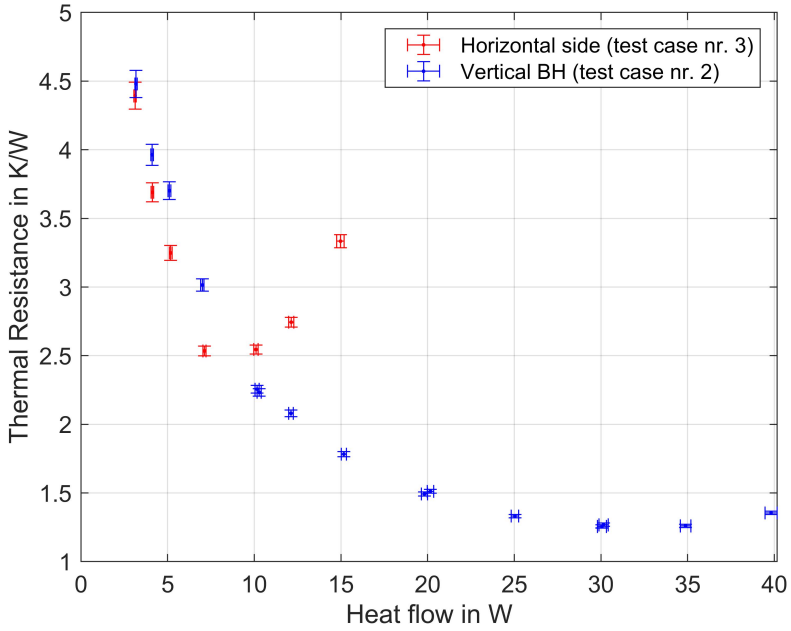

Figure 5.7: Thermal resistance of test setup 1 for different orientations at 20◦ C condenser temperature and 70% filling ratio (test case nr. 2 & 3)

5.5 Effect of filling ratio on thermal resistance

Thermal measurements were also conducted for different filling ratios with the refrigerant R1233zd(E). 30%, 50%, and 70% were chosen for the investigation. In vertical bottom-heated orientation, figure 5.8 shows the comparison between different filling ratios for test setup 1 and 20°C condenser temperature. For all investigated heat flow rates, the thermal resistance was lower for lower filling r atios. C onsequently, 3 0% fi lling ratio yielded the overall lowest thermal resistance values of 0.8 K/W at the optimum compared to 1 K/W and 1.25 K/W at the optima for 50% and 70% filling ratio, r espectively. While the optimum for 70% filling ratio is located at 30 W to 35 W, the optimum for 50 % and 30% filling ratio are at 25 W.

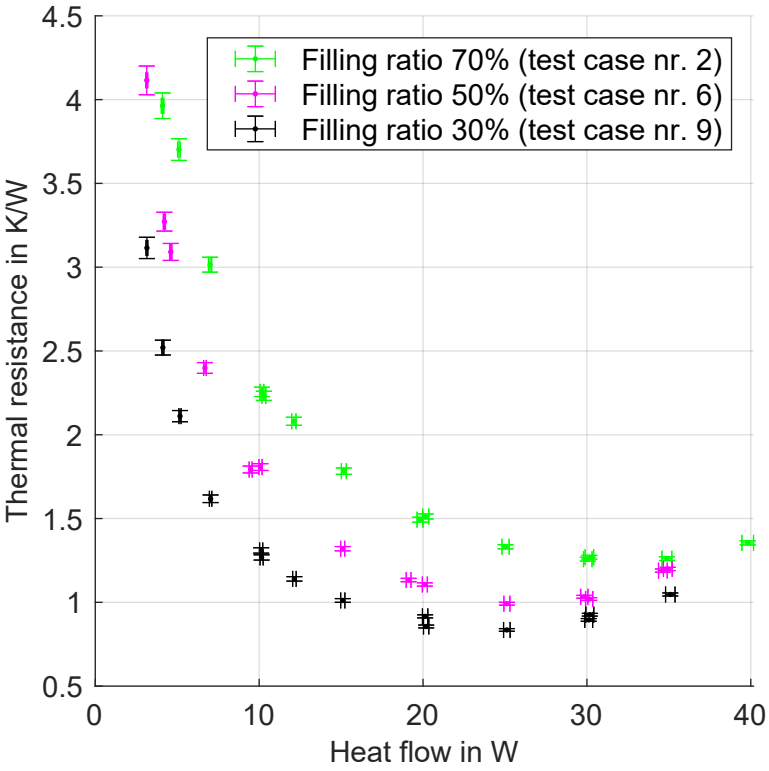

Figure 5.8: Thermal resistance of test setup 1 in vertical BH orientation for different filling ratios at 20◦C condenser temperature (test cases nr. 2, 6 & 9)

Dry-out was not reached for 70% filling ratio for tests up to 40 W. The heat flow was

limited by the maximum allowed fluid pressure, so the dry-out limit is higher than 40 W. The last stable points for filling ratios 30% and 50% were at 35 W. Higher heat flow rates led to dry-out. It can, therefore, be concluded that the dry-out limits are reached at lower heat flow rates for lower filling ratios. The difference in thermal resistance between the different filling ratios is especially pronounced at medium and low heat flow rates up to around 20 W. For higher heat loads the difference becomes smaller and almost negligible close to the dry-out limit at 35 W. The same trend could be observed for all three evaporator roughness values (test setups) and all tested condenser temperatures.

5.6 Effect of condenser temperature on thermal resistance

The effect of different condenser temperatures on the thermal performance was investi-gated. The result can be seen in figure 5.9.

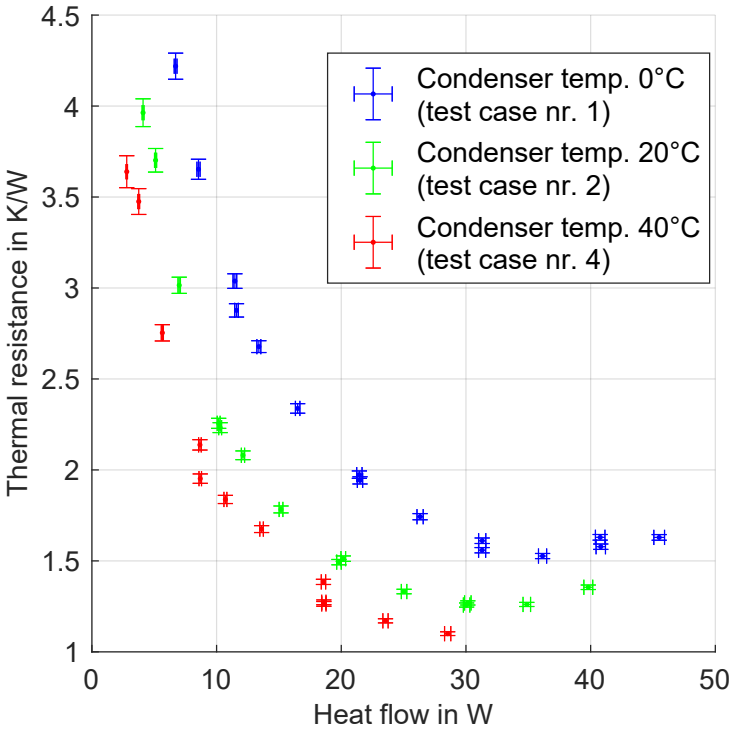

Figure 5.9: Thermal resistance of test setup 1 in vertical BH orientation for different condenser temperatures at 70% filling ratio (test case nr. 1, 2 & 4)

The condenser temperature directly sets the overall temperature level and, thus, average saturation temperature of the PHP fluid. Subsequently, fluid properties such as density, surface tension, viscosity, and heat of vaporization change. Experiments were conducted where apart from the heat flow, only the condenser temperature was varied. The experiments were firstly conducted for test setup 1 at a filling ratio of 70% in vertical orientation (figure 5.9). It can be concluded that lower condenser temperatures lead to a higher thermal resistance. This trend could be repeated for all evaporator roughness values and filling ratios. The optimum thermal resistances can be found at slightly lower heat flow rates for higher condenser temperatures. Thus, the optimum thermal resistances are reached at 30 W with 1.25 K/W for 20°C condenser temperature and at 35 W with 1.5 K/W for 0°C condenser temperature. This leads to almost the same qualitative behavior, but with a shift of the curves towards lower heat flow rates for higher condenser temperature.

5.7 Effect of surface roughness on thermal resistance

As explained in chapter 4.1.2, the three setups all have different evaporator roughness values due to different surface treatments. The first setup is milled with no further surface treatment and has, therefore, the smoothest surface. The second setup has a sand blasted surface that is very rough, and the third setup was glass bead blasted and, thus, has an intermediate evaporator surface roughness. The influence of evaporator surface roughness on the thermal resistance was investigated by comparing the three different experimental setups.

The effect of the different surface roughness values can be seen in figure 5.10. The data is recorded identically for all three setups at 70% filling ratio and 20°C condenser temperature. Setup 1 with the smoothest surface has the highest thermal resistance for all recorded heat flow rates. Setup 2 with the roughest surface has the lowest thermal resistance and setup 3 has an intermediate thermal resistance for an intermediate surface roughness. Thus, the thermal resistance decreases consistently with increasing evaporator surface roughness. The decrease in thermal resistance with increasing heat flow is most prominent for setup 1 and considerably less pronounced for setup 3. Setup 2 has no decrease in thermal resistance with increasing heat flow and is almost constant. The effect is even slightly inversed, with the thermal resistance increasing slightly with increasing heat flow. Overall, the difference in thermal resistance between the three setups is, therefore, largest for small heat flow rates. At 30 W to 40 W the difference between setups 2 and 3 is almost zero and the difference between setup 1 and the other two setups also reaches a minimum at 30 W. The qualitative differences described here also occur at

different condenser temperatures and filling ratios.

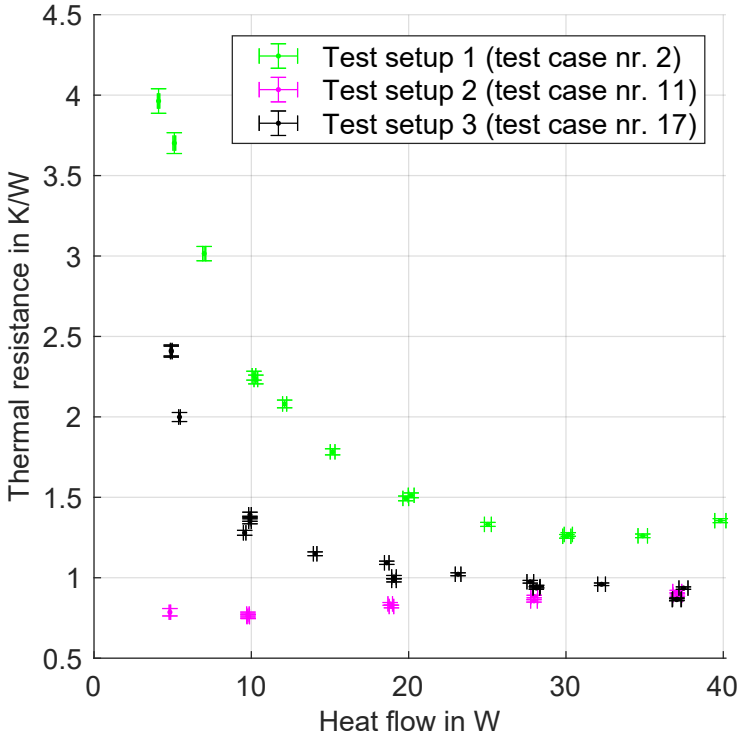

Figure 5.10: Thermal resistance for different test setups in vertical BH orientation at 70% filling ratio and 20◦C condenser temperature (test case nr. 2, 11 & 17)

The impact of evaporator roughness on the flow behavior is shown in figure 5.11. The left image shows the first test setup with the smoothest surface structure (only milled) at 10 W, a filling ratio of 70%, and a condenser temperature of 0°C. The flow is dominated by small bubbles, which are nucleated in the evaporator section and moving into the condenser section without pushing liquid columns into adjacent channels. Only the middle channels are active, the outer channels show no bubble movement.

The middle image shows the second test setup with the roughest surface. All channels are actively pulsating and the flow is dominated by bubbles that grow very long and almost reach the full length of a channel. Thus, liquid columns are displaced far into adjacent channels and create a very chaotic slug-plug flow. Though not visible in the single frame, it could be observed that flow velocities are highest for test setup 2 for these boundary conditions.

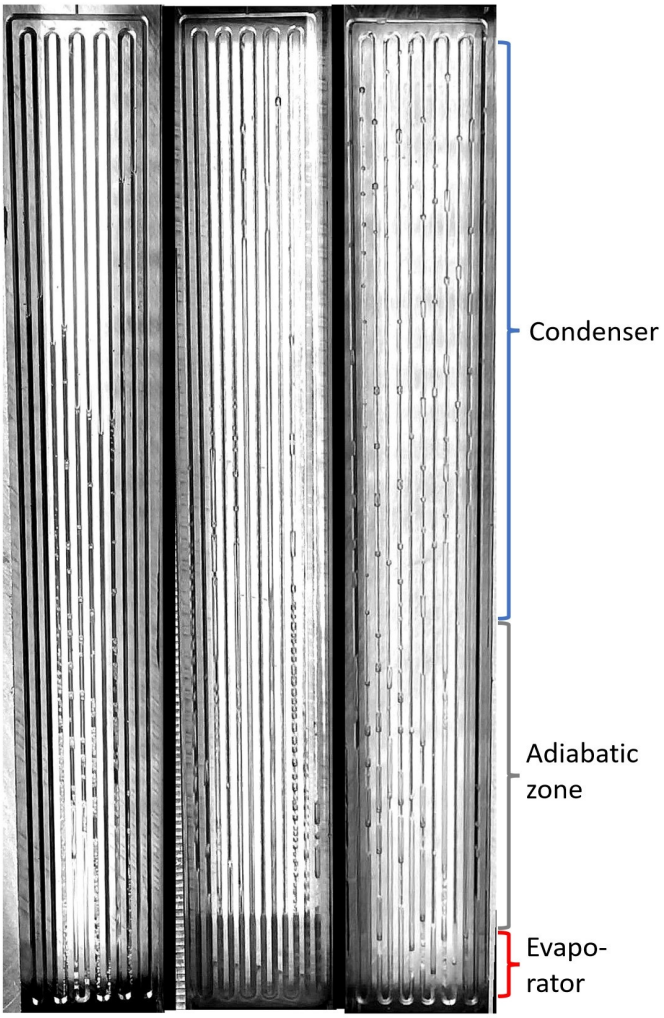

Figure 5.11: Flow comparison between test setups 1 (left), 2 (middle), and 3 (right) at 10 W, filling ratio 70%, and 20◦C condenser temperature in vertical BH orientation (test case nr. 2, 11 & 17)

The right image shows the third test setup with an intermediate roughness due to glass-bead blasting. The flow behavior can also be considered as an intermediate step between test setups 1 and 2. The general flow behavior is dominated by chaotic slug-plug flow in all channels and, therefore, resembles the flow in test setup 2. However, the bubble sizes that could be observed are a lot smaller than in test setup 2.

6 Correlations

Based on the experimental results presented in chapter 5, a correlation is introduced that links the overall thermal resistance with various influencing parameters such as heat flow, condenser temperature, surface roughness, fluid, and filling ratio (section 6.1). The correlation is based on the bubble nucleation threshold. Subsequently, the second part of this chapter (section 6.2) presents experimental results of bubble nucleation rates, to examine, whether a plausible link between the nucleation threshold and bubble nucleation rates can be found.

6.1 Correlation of thermal resistance with nucleation threshold

The influence of surface roughness on thermal resistance is very distinct as shown in chapter 5.7. It is reasonable to further investigate the physical effects behind the influence. Changes in surface roughness strongly influence the temperature difference needed for bubble nucleation, the nucleation threshold $\Delta T_{nucleation}$. It is calculated by

$$\Delta T_{nucleation} = T_{wall} - T_{sat} = \frac{2 T_{sat} \sigma}{h_E \rho_{sat} r_{bubble}}. \tag{6.1}$$

The presented equation 6.1 [13] is known as the pool boiling nucleation equation. The fluid properties surface tension σ, latent heat of vaporization h_E, and the saturated vapor density ρ_{sat} are determined at the saturation temperature T_{sat}. The saturation temperature is not measured directly, as it cannot be measured easily without significant intervention into the PHP channel and subsequent influencing of the evaporation behavior of the PHP. Instead, it is estimated to be equal to the mean temperature in the adiabatic zone. For the bubble radii r_{bubble}, the mean bubble radii determined for each test setup in chapter 4.1.2, are used. The pool boiling nucleation equation shows that higher surface roughness values and, consequently, higher bubble radius values result in lower nucleation threshold. To investigate whether changes in nucleation threshold cause the changes in thermal resistance, observed in the experiments, nucleation thresholds are calculated for each measured data point.

The calculated bubble nucleation thresholds $\Delta T_{\text{nucleation}}$ are further used to calculate the relative nucleation threshold RNT by

$$RNT = \frac{\Delta T_{nucleation}}{\dot{Q}_{corr} R_{th,true}} = \frac{T_{wall} - T_{sat}}{T_{evap} - T_{cond}}, \tag{6.2}$$

where $\dot{Q}_{\text{corr}}$ is the effective input heat flow rate as determined in chapter 4.4. $R_{\text{th,true}}$ is the thermal resistance of the fully insulated, unfilled PHP. The denominator is equal to the temperature difference the test setup exhibits for the given input heat flow rate at no PHP pulsation or when the PHP does not contain refrigerant. RNT is, therefore, a quotient of temperature differences and, thus, a dimensionless number.

The measured thermal resistance $R_{\text{th,corr}}$ is further used to calculate the relative thermal resistance RTR by

$$RTR = \frac{R_{th,corr}}{R_{th,true}}. \tag{6.3}$$

The quotient presents a quality criterion of the PHP, quantifying the thermal resistance enhancement the PHP offers compared to the absence of PHP operation.

The two dimensionless values RNT and RTR are plotted in figure 6.1. All measurement data listed in tables 5.1 and 5.2 is contained here. Different filling ratios, heat flow rates, condenser temperatures, and wall roughness values (different test setups) are included in the plot. The plot shows that low RNT values generally lead to low relative thermal resistances. For a constant filling ratio, the relative thermal resistance can be correlated to RNT. However, different filling ratios exhibit different correlation parameters. Subsequently, a fitting curve can be found, that represents the correlation between the relative thermal resistance and RNT for each filling ratio individually. The fitting curves for the investigated filling ratios 30%, 50%, and 70% are also depicted in the plot. Using a power function approach the fitting curves can be calculated by

$$RTR = a + b(RNT)^c. \tag{6.4}$$

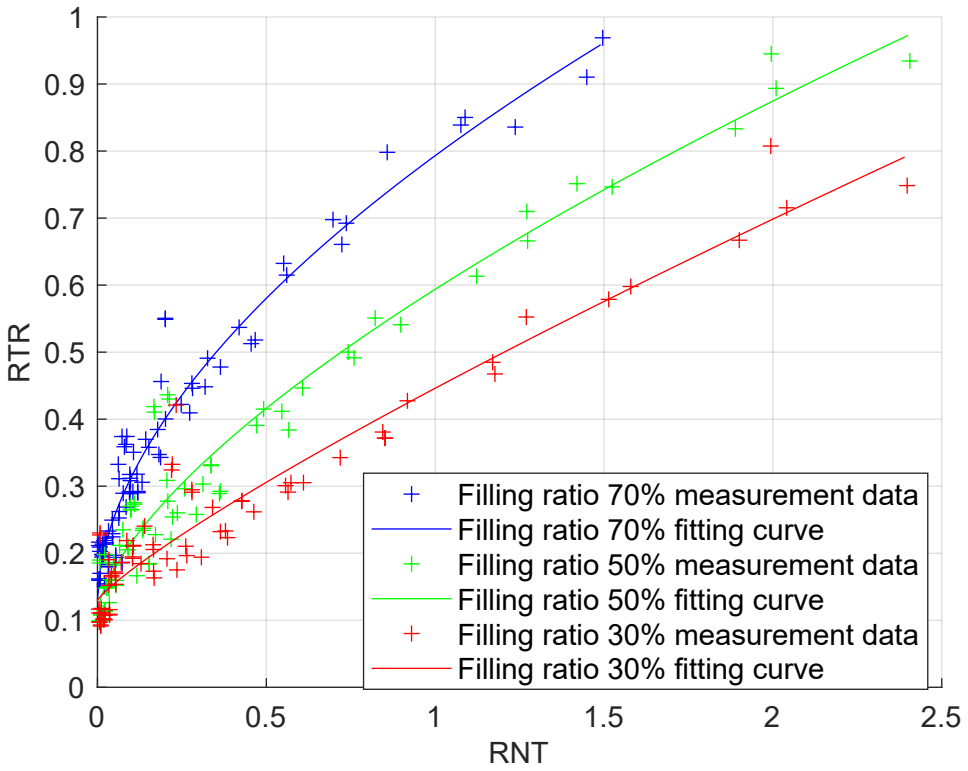

Figure 6.1: Correlation between relative nucleation threshold and relative thermal resistance; filling ratio 70%: test case 1, 2, 4, 11, 12, 17; filling ratio 50%: test case 5, 6, 7, 13, 14, 18; filling ratio 30%: test case 8, 9, 10, 15, 16, 19

It contains the fitting parameters a, b, and c that have unique values for each filling ratio. The fitted parameter values can be found in table 6.1. The fitted curve for 70% filling ratio exhibits the highest gradient. The curves become less steep with 50% and 30% filling ratio, respectively. It can, therefore, be concluded that for high filling ratios, the relative nucleation threshold has the highest impact on PHP performance. There also exists a threshold value for the relative nucleation threshold, that needs to be underrun for PHP operation. The threshold values for 70% and 50% filling ratio are 1.5 and 2.5, respectively. At 30% filling ratio, the threshold value was not reached in the measurements. By using the fitting curve, it is estimated to be around 3.3. To validate the threshold value at 30% filling ratio experimentally, measurements at lower temperatures or smoother surfaces (for example polished) are needed, to further increase the nucleation threshold. If all cavities were of the same size, no PHP start-up would occur for RNT values greater than

1. On real surfaces, however, RNT is based on an average cavity size, larger cavities are still present on the surface. Therefore, a PHP can also start-up for RNT>1, although the number of active cavities and, thus, the PHP performance is limited.

Filling ratio	a	b	c
70%	0.1308	0.6623	0.5593
50%	0.1104	0.4834	0.6608
30%	0.1296	0.3165	0.8457

Table 6.1: Correlation constants for different filling ratios

In general, the threshold value increases with decreasing filling ratio. Therefore, PHPs with lower filling ratios perform better at conditions of high relative nucleation threshold. For example, if a PHP is intended to exhibit good thermal performance at low condenser temperatures (cold start) and low heat flow rates, a low filling ratio should be chosen. Towards a nucleation threshold of zero, the curves approach a minimum value of relative thermal resistance. This presents a limit where no further improvement is possible.

The relative nucleation threshold only considers the mean value of the bubble radius distribution profile of a surface and only accounts for an average nucleation threshold. It neglects surface cavities that have larger size than the average value. Larger cavities and, thus, larger bubble radii, have a lower nucleation threshold and, therefore, lead to bubble nucleation even if the calculated average nucleation threshold of the surface is not reached yet. A more precise way of analyzing the nucleation behavior is to calculate the number of active nucleation sites.

The fluid's saturation temperature T_{sat} is estimated by measuring the mean wall temperature in the adiabatic zone. The difference between the evaporator wall temperature $T_{evap,wall}$ and the saturation temperature T_{sat} presents the available temperature difference for bubble nucleation that was measured in the experiments. The rearranged form of the pool boiling nucleation equation yields the minimum bubble radius $r_{bubble,min}$ of a surface cavity (or nucleation site), that can be activated for a given temperature difference. It is calculated by

$$r_{bubble,min} = \frac{2T_{sat}\sigma}{h_E \rho_{sat}(T_{evap,wall} - T_{sat})}, \tag{6.5}$$

where $r_{bubble,min}$ presents a minimum threshold, where all cavities, or potential nucleation sites, that are larger than the threshold can be activated for the available temperature

difference. A bubble radius distribution profile as presented in chapter 4.1.2 (for example in figure 4.22) shows the number of surface cavities of a given size with respect to the cavity size. As bubbles are nucleated in these cavities, the bubble radius is regarded to be equal to the cavity size. Thus, it can be formulated as a function $n_{bubble}(r_{bubble})$. The number of active nucleation sites ANS represents the number of surface cavities that are larger in size than the calculated minimum bubble radius $r_{bubble,min}$ and is defined by

$$ANS = \int_{r_{bubble,min}}^{\infty} \frac{n_{bubble}(r_{bubble})}{A_{analysis}} dr_{bubble}. \tag{6.6}$$

Subsequently, each measured data point can be associated with an ANS value that represents the number of active nucleation sites for the measured temperature difference. ANS does not equal the number of bubbles visible in a flow visualization. It is the number of cavities on a surface that can be activated to produce a bubble of microscopic size within its confinements. A few of these microscopic bubbles grow due to further heat transfer from the channel wall. Their growth (which implies evaporation) cools down the wall and prevents neighboring microscopic bubbles from growing at the same rate. Finally, a growing micro-bubble reaches the position of an adjacent micro-bubble, and they merge. In the end, only very few of the original number of micro-bubbles reach a macroscopic size that can be seen visually and that produces pressure gradients that drive the PHP (elongated Taylor-bubbles).

The relative thermal resistance plotted with respect to ANS can be seen in figure 6.2. This diagram shows a correlation between the bubble nucleation behavior, represented by ANS, and the thermal behavior. An increased ANS value leads to a reduced relative thermal resistance and, therefore, enhanced PHP performance. For 70% filling ratio, the thermal resistance drops steepest with increasing ANS value. The curve becomes less steep for 50% and 30% filling ratio. Additionally, a minimum number of active nucleation sites per surface area can be found depending on the filling ratio. For PHP startup 350 active nucleation sites per square millimeter are necessary at 70% filling ratio. For 50% and 30% filling ratio, the minimum number of active nucleation sites decreases to 90 and 12 $1/mm^2$, respectively. For values of ANS = 10^4 $1/mm^2$, almost all potential nucleation sites are active. This explains why no further thermal resistance improvement is possible at this point.

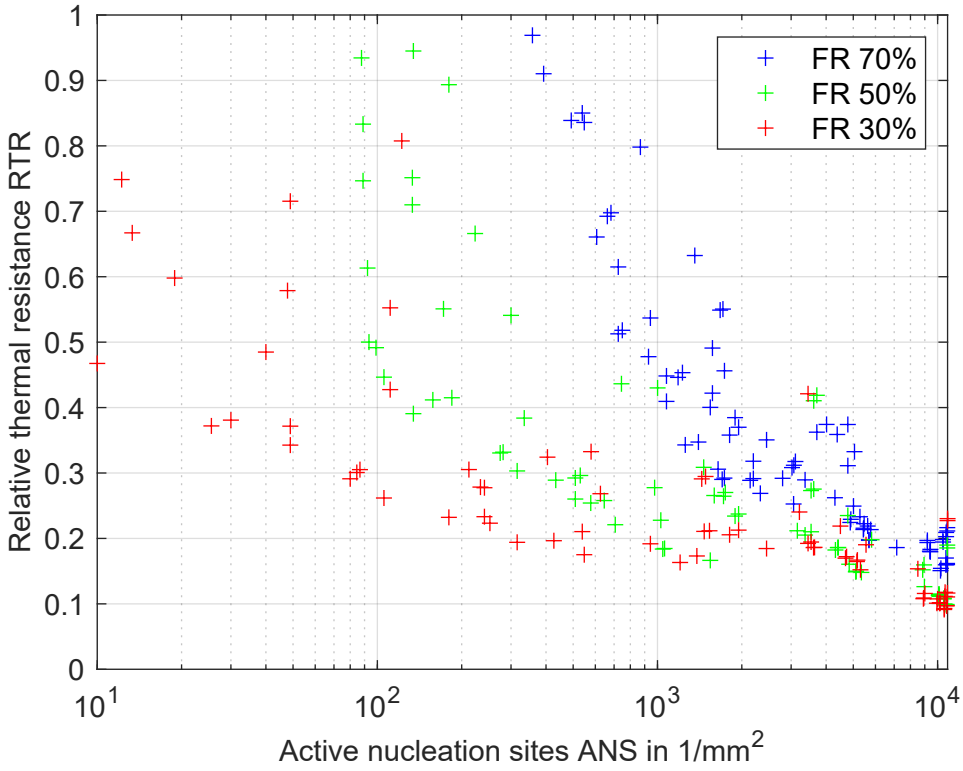

Figure 6.2: Relative thermal resistances of PHP at different filling ratios for all data points; filling ratio 70%: test case nr. 1, 2, 4, 11, 12, 17; filling ratio 50%: test case nr. 5, 6, 7, 13, 14, 18; filling ratio 30%: test case nr. 8, 9, 10, 15, 16, 19

6.2 Bubble nucleation rates

The analysis of the high-speed video material as described in chapter 4.3 reveals average bubble nucleation rates in the evaporator area for the investigated boundary conditions. For test setup 1 and 70% filling ratio, the bubble nucleation rates are displayed in figure 6.3 for two different condenser temperatures. Both curves approach zero bubbles per second for a heat flow approaching zero. Starting at this point, the nucleation rates increase with increasing heat flow. For a condenser temperature of 0°C, the nucleation rate reaches a maximum at 6500 1/s and 22 W. For a condenser temperature of 20°C, the maximum is reached already at 15 W with a value of 8100 1/s. For heat flow rates higher than the location of the peak, the nucleation rates in both curves decrease until

they approach zero close to the dry-out limit at the maximum investigated heat flow rates.

The increase of nucleation rate with increasing heat flow at low heat flow rates strengthens the impression that bubble nucleation strongly influences the PHP behavior. With increasing heat flow, the relative nucleation threshold RNT decreases, facilitating bubble nucleation and decreasing the thermal resistance as the pulsating motion is enhanced by an increased number of disturbances. For a higher condenser temperature, higher values of bubble nucleation rate can be achieved which is in accordance with a reduced nucleation threshold at higher fluid temperatures. However, both curves of nucleation rates reach a maximum and the nucleation rate decreases for heat flow rates above the peak location. In this area of high heat flow rate, the thermal resistance still decreases. Consequently, the thermal resistance of the PHP cannot be directly correlated with the bubble nucleation rate.

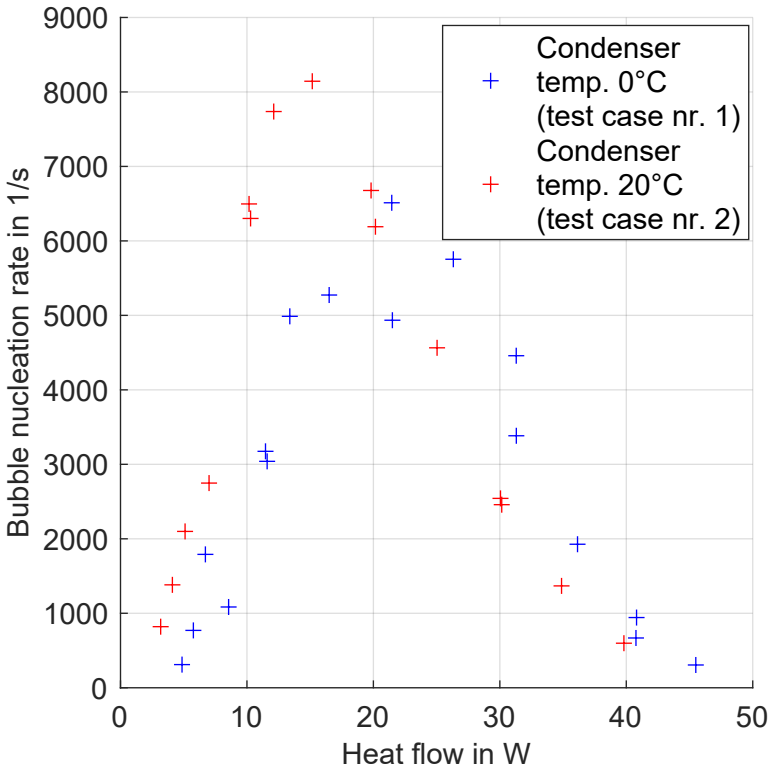

Figure 6.3: Bubble nucleation rates for 0◦C and 20◦C of test setup 1 at 70% filling ratio, test case nr. 1 & 2

The decrease in nucleation rate for high heat flow rates may be a result of a decreasing liquid mass fraction in the evaporator section. Bubble nucleation can only occur if a liquid slug passes through the evaporator section, but at high heat flow rates the evaporator section is filled increasingly with elongated bubbles or even local dry-out zones. Figure 6.4 compares two images of the same channel segment at different input heat flow. The upper image shows the channel at 20 W and the lower image at 45 W. Both images were recorded with test setup 1 for 70% filling ratio and 20°C condenser temperature. The upper image shows segments of an elongated bubble on the left-hand side, followed by smaller circular bubbles that grow within a liquid slug. The liquid slug fills the largest portion of the channel segment and continues all the way to the right-hand side with many small circular bubbles. The lower image at higher heat flow is completely filled with an elongated bubble and, thus, no smaller circular bubbles are visible.

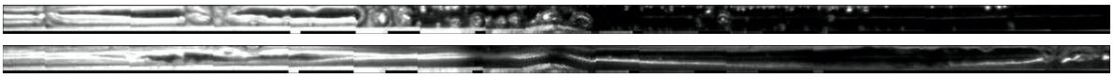

Figure 6.4: Example images of a channel segment at 20 W (upper image) and 45 W (lower image) heat flow for test setup 1 at 20◦C and 70% filling ratio (test case nr. 2)

The influence of wall roughness and filling ratio on the bubble nucleation rate was also investigated. The results from chapter 6.1 indicate, that for a constant filling ratio, the PHP performance depends only on the relative nucleation threshold RNT. Therefore, it is firstly analyzed whether the same rule applies to the bubble nucleation rate. Figure 6.5 depicts the bubble nucleation rates with respect to RNT for a filling ratio of 70%. Measurements at different evaporator wall roughness (test setups), condenser temperature, and heat flow rate are included in the plot.

The data shows a steep increase in bubble nucleation rate with increasing relative nucleation threshold at small RNT values. The nucleation rates reach a maximum at an RNT value of approximately 0.3. Above this value, the nucleation rates drop towards high RNT values. For RNT $>$ 0.3, the bubble nucleation rates are explicable, as increasing nucleation threshold leads to lower nucleation rates. For RNT $<$ 0.3, the behavior contradicts the theory, that lower RNT values lead to higher bubble nucleation rates.

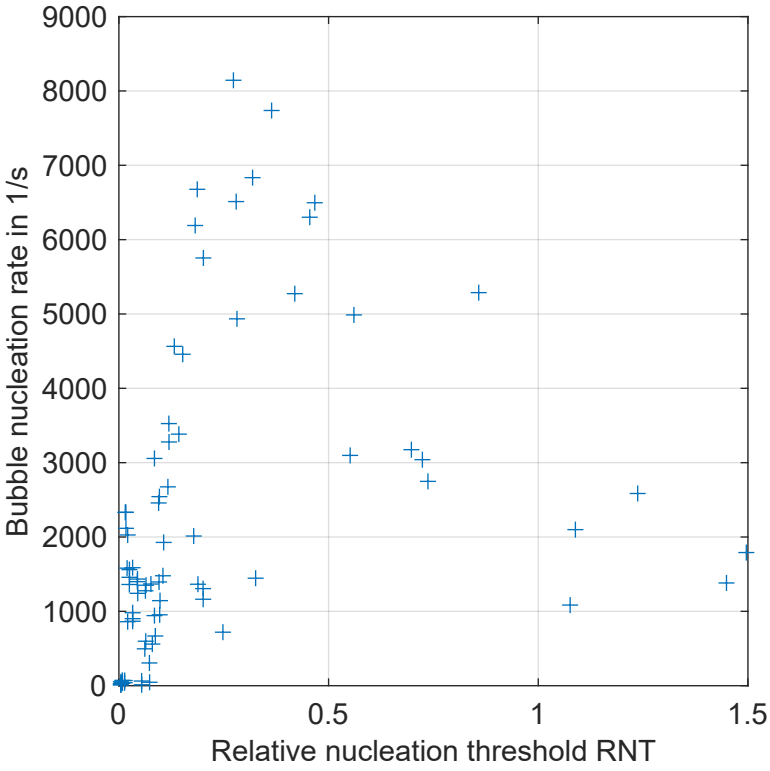

Figure 6.5: Bubble nucleation rates for all data points at 70% filling ratio with respect to relative nucleation thresholds (test case nr. 1, 2, 4, 11, 12, 17)

Two possible explanations can be found for the behavior of the bubble nucleation rates at low RNT values:

Firstly, it is possible that the relative nucleation threshold is only the limiting quantity in a range of RNT > 0.3. For low RNT values, other phenomena such as film evaporation and frictional pressure drop of liquid slugs at the walls and in the bends could be the dominant effects. Therefore, the overall PHP behavior might not be represented only by RNT in ranges of RNT < 0.3. In this case, a limited range of validity (RNT > 0.3) should be considered for the correlation presented in chapter 6.1.

Secondly, the overall PHP behavior might still be limited mainly by the relative nucleation threshold, even in ranges of RNT < 0.3. In this case, the drop of bubble nucleation rate towards RNT $= 0$ might be explicable by another effect: Bubbles can only be nucleated if liquid is present in the evaporator. The recorded video material revealed qualitatively that on average, less liquid is present in the evaporator at high heat flow rates compared

to low heat flow rates. Therefore, it is possible that the reduction in bubble nucleation rate is simply caused by less time in which liquid is present in the evaporator. Further investigations must be conducted to see which of these two theories are valid.

While at a filling ratio of 70% the nucleation rates show a clear maximum, the data is less clear for the filling ratios 50% and 30%. Figure 6.6 shows the nucleation rates plotted with respect to RNT for all filling ratios in comparison. The plot shows that lower filling ratios generally exhibit lower bubble nucleation rates. Also, the maximum achievable nucleation rate is lower for lower filling ratios. From the video data it was qualitatively visible that lower filling ratios typically correspond to less liquid in the evaporator (or less time that the evaporator contains liquid on average). This supports the second theory stated above, that low liquid content in the evaporator prevents higher bubble nucleation rates.

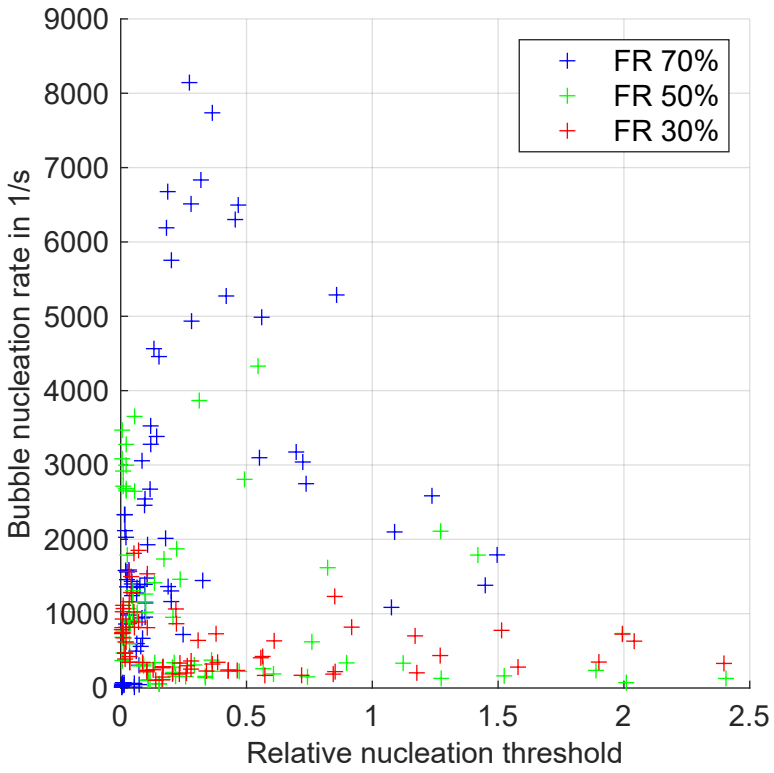

Figure 6.6: Bubble nucleation rates for all data points; filling ratio 70%: test case nr. 1, 2, 4, 11, 12, 17; filling ratio 50%: test case nr. 5, 6, 7, 13, 14, 18; filling ratio 30%: test case nr. 8, 9, 10, 15, 16, 19

While this general trend is visible from the data in the plot, no clear maximum bubble nucleation rates can be identified for 50% and 30% filling ratio. The optical analysis of nucleation rate determines an average value for the recorded time frame. Therefore, it shows some scattering of the data depending on how much and how fast the nucleation rates change with time. The absolute error tends to increase when less liquid is present in the evaporator on average, because the result then depends hugely on the exact time of the recording. Therefore, lower filling ratios increase the absolute error of the estimation. Additionally, the values of bubble nucleation rate are lower for lower filling ratios. Consequently, the relative error in the data is significantly higher for 50% and 30% filling ratio than for 70%. Ultimately, the data at 50% and 30% filling ratio can only be used to show that the general level of bubble nucleation rate is lower than for 70%. No clear dependency on RNT can be derived at these low filling ratios. Longer time intervals need to be recorded in order to reduce the measurement error to an acceptable level. However, this would require different camera equipment and could, therefore, not be done in this work.

7 Numerical simulations

The measurements presented in chapters 4 and 5 led to a correlation found between relative thermal resistance RTR and relative nucleation threshold RNT (section 6). Though the results showed a clear correlation between the two values, the plausibility check using the recorded bubble nucleation rates yielded some open questions (section 6.2): For very low RNT values, a decrease in RNT did not lead to a higher bubble nucleation rate. Therefore, further insights into PHP behavior need to be generated. As not all quantities are easily measurable in an experimental setup, 1D-simulations are first validated (section 7.1) and then analyzed for further physical properties. In total, the internal heat transfer coefficients (section 7.2), oscillation frequencies (section 7.3), and liquid mass fractions in the evaporator section (section 7.4) are analyzed in these simulations. Lastly, section 7.5 numerically investigates the influence of geometry variations on the thermal resistance of the PHP. Thus, the correlation from chapter 6 is extended to facilitate a simple prediction method for the thermal resistance of a PHP. The modified version of the correlation is then validated numerically.

7.1 Validation of 1D-simulation

The simulations presented here were all conducted with the software PHP-Sim Desktop in the version 0.2.19, published by JJ Cooling Innovation Sarl. The software uses the simulation approach published by Aubin et al. [13]. Therefore, it presents a 1D-approach that models the physical phenomena by using the Taylor-bubble model and associated correlations [13]. Chapter 2.3 gives an overview of the modelled physical phenomena. As the modelling is well published [13], this chapter focuses on the documentation of the input data required for the simulations by the software and the results obtained from the simulations.

The simulation uses a 1D-approach. Therefore, the geometrical setup can be defined by parameters alone. The parameters mimic the setup that was experimentally investigated. The channel setup is shown schematically in figure 7.1. The evaporator turns are adiabatic

and, thus, not included in the evaporator area. The constant heat flow applied to the channel walls is, therefore, limited to the marked evaporator area. Similarly, the condenser turns are not included in the condenser area.

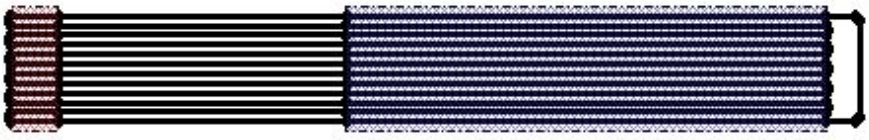

Figure 7.1: Channel setup in 1D-simulation

A specific external thermal resistance of 0.3 Km/W with a cooling reference temperature is applied to the channel walls in the condenser area. The specific external thermal resistance $R_{th,spec}$ is defined by

$$R_{th,spec} = R_{th,ext} L_{channel}, \tag{7.1}$$

where $R_{th,ext}$ is the thermal resistance to the external reference temperature and $L_{channel}$ is the length of the channel, that the boundary condition is applied to (total channel length within condenser zone). The cooling reference temperature is set equal to the coolant inlet temperature in the experiments. The section between evaporator and condenser is the adiabatic section and has no heat transfer to the surroundings.

The roughness of the inner channel walls is set equal to the mean bubble radii derived from the confocal surface analysis in chapter 4.1.2. Therefore, 0.2089 μm, 4.537 μm, and 1.255 μm are used for test setups 1, 2, and 3, respectively.

In the simulation settings, a fraction of inner channel surface area involved in heat transfer with the channel walls can be defined. As the channels in the experiments were covered with an insulating glass plate, only three of four channel walls participated in heat transfer. Therefore, the fraction is set to 0.75. Finally, the channel is split into equally long cells of 1 mm length for the numerical discretization. The time constants are chosen dynamically by the simulation to maintain a constant Courant number of 0.1. The total time simulated is 100 s.

A full list of simulation boundary conditions can be found in table 10.1 in appendix 10.4.

From the simulation results, multiple physical properties can be obtained with respect to time, as the simulation is fully transient. As an example, the average evaporator and condenser wall temperatures are plotted in figure 7.2. To calculate a thermal resistance similar to the experimental investigations in chapter 4.4, time averaged values of the wall

temperatures were obtained using an averaging interval of 20 s. The results are evaluated in a quasi-steady state condition.

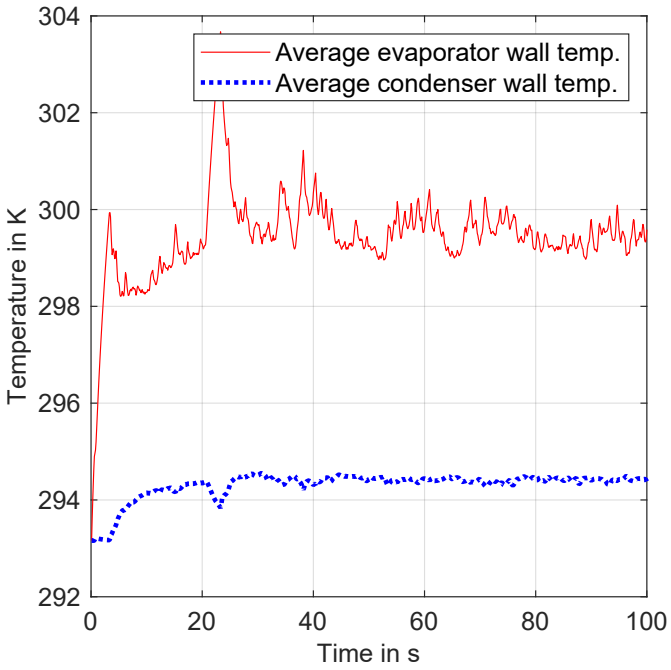

Figure 7.2: Example result of 1D PHP simulation

The boundary conditions of the simulations are chosen equal to the boundary conditions of the experiments. Therefore, the resulting thermal resistances should be the same if the simulation accurately predicts the behavior of the PHP. In a first attempt, test setup 1 is considered at a filling ratio of 70%. Consequently, the roughness value (0.2089 μm) and filling ratio in the simulation are set accordingly. Heat flow and condenser temperature are varied. The simulated thermal resistances for this set of boundary conditions can be seen in figure 7.3 in comparison to the associated experimental results. Firstly, considering the results at 20°C condenser temperature, the simulation predicted the thermal resistances quite accurately. The highest error is at 20 W with approximately -16% (-0.25 K/W). The influence of heat flow is well reproduced, showing the same decrease in thermal resistance with increasing heat flow. The influence of condenser temperature on the thermal resistance is also well reproduced. The curves at 0°C and 40°C condenser temperature are both predicted accurately. The highest error is found at 40°C condenser temperature and 10 W with 29% (-0.58 K/W). The error of all data

shown in figure 7.3 is in a range of approximately ±10% besides the two mentioned exceptions. The average error is ±8% for all simulations.

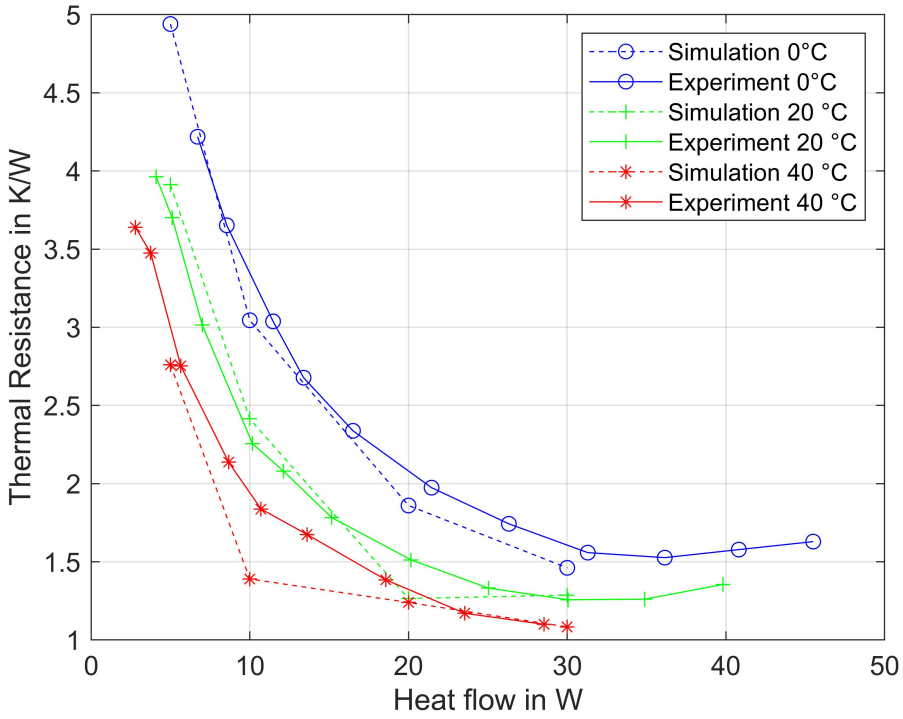

Figure 7.3: Comparison of simulation to experimental data for different condenser temperatures for test setup 1 with filling ratio 70%

As a next step, the variation of surface roughness is investigated in the simulation. Roughness values can only be set globally for the full channel in the simulation. In the experiments, however, the roughness is only changed in the evaporator section. Roughness influences the frictional losses and pressure drops in the PHP. Therefore, the boundary conditions for test setups 2 and 3 are physically not exactly reproduced in the simulations and a slight offset is to be expected. Nevertheless, the simulations correctly depict the changes in bubble nucleation behavior due to different surface roughness in the evaporator area. For the simulations, the analyzed mean bubble radii for each test setup are used. Therefore, the channel roughness is chosen as 0.2089 μm, 4.537 μm, and 1.255 μm for test setups 1, 2, and 3, respectively. Changes in heat flow and surface roughness are investigated for a filling ratio of 70%, because the thermal resistance change with RNT is most pronounced here, as shown in chapter 6.1. Additionally, a condenser temperature

of 20°C is chosen. The comparison of simulation and experimental results is depicted in figure 7.4. The qualitative differences between the roughness values is reproduced sufficiently. The difference between the smooth test setup 1 and the rougher test setups 2 and 3 is of the correct scale and highest for small heat flow rates. At higher heat flow rates, especially at 30 W, the curves for different evaporator roughness are very close together, both in simulation and experiments. The qualitative differences are, therefore, overall, well reproduced. However, the error to the experimental results increases compared to the errors found for test setup 1. The average error for the simulation results associated with test setup 2 is 34%, for test setup 3 the average error is 27%. Considering the fact, that the roughness is applied uniformly on the full channel in the simulation, while in the experiments only the evaporator roughness was varied, the prediction quality was still within a reasonable range.

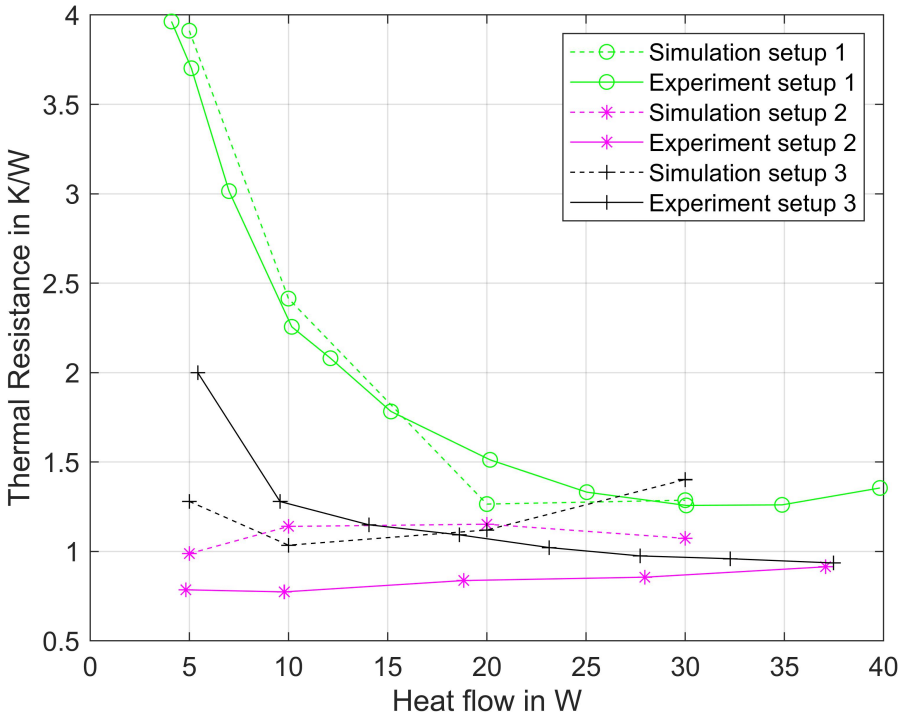

Figure 7.4: Comparison of simulation to experimental data for different test setups at filling ratio 70% and 20◦C condenser temperature

The influence of filling ratio is investigated in the simulation compared to the experimental results. The comparison depicted in figure 7.5 is conducted for test setup 1 at 20°C

condenser temperature. In the experiments, the filling ratio 70% produced the highest thermal resistances. Reducing the filling ratio to 50% and 30% each resulted in a lower thermal resistance. The simulation conducted for 70% filling ratio fitted well with the experimental data.

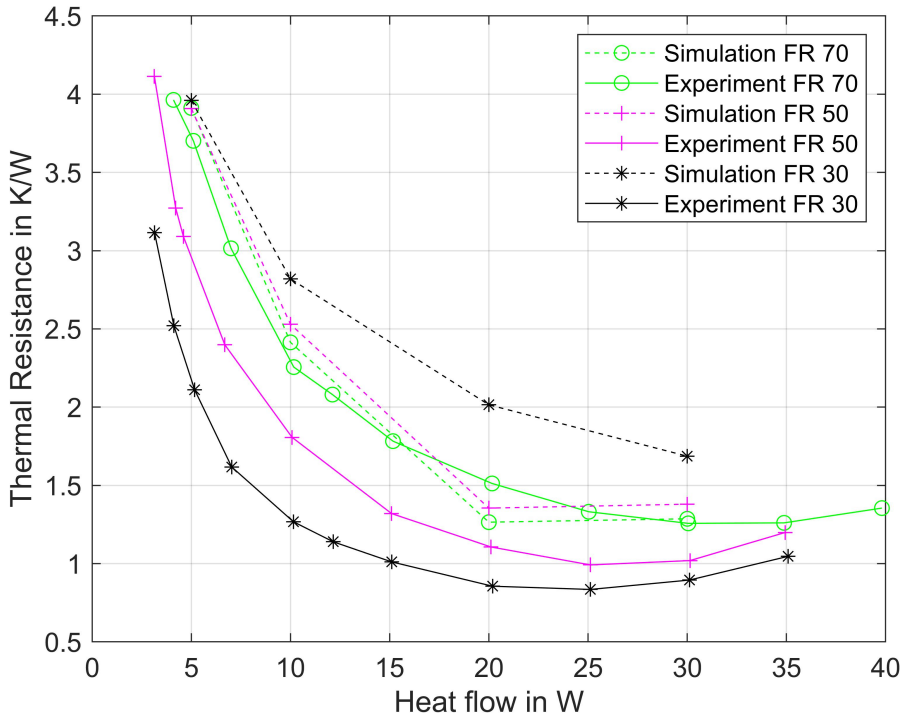

Figure 7.5: Comparison of simulation to experimental data for different filling ratios for test setup 1 and 20◦C condenser temperature

However, the simulation for 50% filling ratio produced almost the same thermal resistances as for 70%, while in the experiments a significant reduction could be observed. Therefore, the average error for 50% filling ratio is 34%. In the simulations, 30% filling ratio produces higher thermal resistances than 50% filling ratio. In the experiments, the opposite effect could be observed. The average error for 30% filling ratio is, consequently, very high at 107%. Overall, the influence of filling ratio was not predicted well in the simulations, the qualitative tendency was not reproduced. This results in high prediction errors for 30% and 50% filling ratio. Two possible explanations can be found, why the simulation yields less accurate results at lower filling ratios: Firstly, the simulation limits the film thickness to values greater than the surface roughness to numerically stabilize

the simulation. Therefore, local dry-out is assumed in the simulation at locations, where the film thickness reaches the value of the surface roughness. At lower filling ratios, this happens quite frequently, as Taylor bubbles grow larger and time spans until rewetting of the surface by a liquid slug are higher compared to at higher filling ratios. Therefore, the simulation assumes local dry-out, associated with zero heat transfer, where in reality local dry-out is not yet reached and the heat transfer is very high due to thin liquid film evaporation. Secondly, the simulation assumes a stationary liquid film at the walls. The thickness of the film changes locally due to heat transfer and differently in each cell of the simulation. Therefore, intense local heating can lead to local dry-out in fractions of a Taylor bubble, while the liquid film close by hardly changes thickness. In reality, the surface tension of the fluid leads to a more homogeneous film thickness and local dry-out does not occur as often as in the simulation.

7.2 Heat transfer coefficients

An experimentally validated simulation offers more insights into the behavior of a PHP and allows access to physical properties that cannot be measured easily in experiments. The errors in thermal resistance of the simulations compared to the experiments were reasonably low at 70% filling ratio for varied surface roughness, condenser temperature, and heat flow. The errors and the qualitative trends for filling ratio changes were not reproduced well. Therefore, only simulations at 70% filling ratio were used for further investigation. The fluid temperature in the experiments cannot be measured easily, especially in the evaporator area, without interfering with the bubble nucleation behavior. Determining accurate heat transfer coefficients between fluid and channel walls is, therefore, quite difficult in the experiments. In the simulations, the heat transfer coefficients are accessible and offer further insights into the behavior of the PHP.

The simulation distinguishes between three different heat transfer coefficients, depending on which phase is present in a cell. If only vapor is present in the cell (local dry-out), the associated heat transfer coefficient $HTC_{dryout,i}$ in cell i is defined as

$$HTC_{dryout,i} = 0, \tag{7.2}$$

as it is considered to be negligible. If only liquid phase is present in the cell i, the heat transfer coefficient $HTC_{conv,i}$ is defined by

$$HTC_{conv,i} = \frac{\dot{Q}_{conv,i}}{A_i(T_{w,i} - T_{fluid,i})}, \tag{7.3}$$

where $\dot{Q}_{\text{conv,i}}$ is the heat transfer rate due to convection from wall to fluid, A_i is the contact area between fluid and wall, $T_{w,i}$ is the wall temperature, and $T_{\text{fluid,i}}$ is the fluid temperature in cell i. If a Taylor bubble is present, a liquid film is located between wall and vapor, which leads to film evaporation or condensation. Then, the heat transfer coefficient $HTC_{\text{film,i}}$ is defined by

$$HTC_{film,i} = \frac{\dot{Q}_{film,i}}{A_i(T_{w,i} - T_{fluid,i})} = \frac{\lambda_{liq}}{t_{film,i}}, \tag{7.4}$$

where $\dot{Q}_{\text{film,i}}$ is the heat transfer rate due to phase change from wall to fluid, λ_{liq} is the thermal conductivity of the liquid phase, and $t_{\text{film,i}}$ is the film thickness in cell i. The total heat transfer in cell i is then calculated by

$$\dot{Q}_i = \dot{Q}_{film,i} + \dot{Q}_{conv,i} = HTC_{film,i} A_i (T_{w,i} - T_{fluid,i}) + HTC_{conv,i} A_i (T_{w,i} - T_{fluid,i}). \tag{7.5}$$

The effective heat transfer coefficient HTC_i of the cell is defined by

$$HTC_i = \frac{\dot{Q}_i}{A_i(T_{w,i} - T_{fluid,i})}. \tag{7.6}$$

Combined with equation 7.5, this yields

$$HTC_i = HTC_{film,i} + HTC_{conv,i}. \tag{7.7}$$

For one time step, the average heat transfer coefficient for all n cells of the PHP is then calculated by

$$HTC = \frac{1}{n} \sum_{i=1}^{n} HTC_i. \tag{7.8}$$

In a time interval within a quasi-steady-state condition of the simulation, HTC is averaged over all time steps. This yields a location and time averaged HTC value, which is from now on referred to as average HTC. The average HTC between fluid and channel wall of the simulations that were in good agreement with the experimental results were extracted. Figure 7.6 shows the results for simulations at 70% filling ratio.

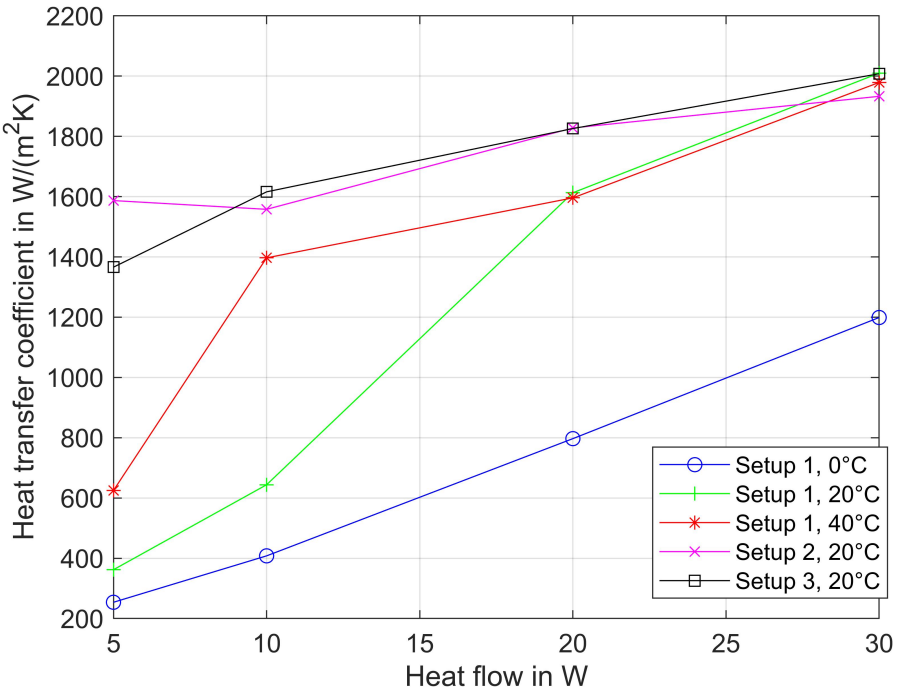

Figure 7.6: Heat transfer coefficients in simulations for different temperatures and test setups at 70% filling ratio

It can be observed that higher surface roughness leads to a high HTC even at low heat flow rates. For test setup 2, the HTC was already at 1600 W/(m^{2}K) for 5 W while test setup 1 only reached 600 W/(m^{2}K) at the same heat flow. Also, the influence of condenser temperature can be seen: Test setup 1 reaches higher HTC values at low heat flow for 40°C condenser temperature than for 20°C and 0°C. The difference to 0°C condenser temperature persists even at higher heat flow rates.

The extracted heat transfer coefficients HTC can also be plotted with respect to their relative nucleation threshold RNT. The result can be seen in figure 7.7. The diagram shows that there is a correlation between RNT and HTC, where low RNT leads to high HTC values. The correlation can be modelled by

$$HTC = \frac{1}{a + b * RNT^c}, \tag{7.9}$$

where the coefficients are defined as a=0.0004 $\frac{\mathrm{m^2K}}{\mathrm{W}}$, b=0.001652 $\frac{\mathrm{m^2K}}{\mathrm{W}}$, and c=0.883.

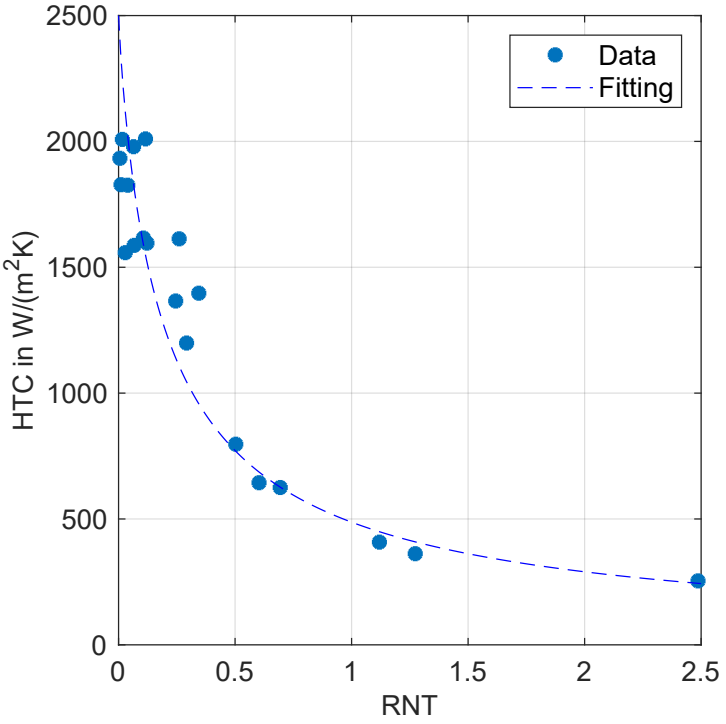

Figure 7.7: Heat transfer coefficients in simulations for different temperatures and test setups at 70% filling ratio with respect to relative nucleation threshold RNT

The HTC values presented above are time averaged HTC values that account for both liquid convection and phase change. The average HTC is defined in the simulation software by

$$HTC = \frac{HTC_{conv}\Delta t_{conv} + HTC_{phase}\Delta t_{phase}}{\Delta t_{conv} + \Delta t_{phase}} = \frac{HTC_{conv}\Delta t_{conv} + HTC_{phase}\Delta t_{phase}}{\Delta t_{total}}, \tag{7.10}$$

where HTC_{conv} is the average heat transfer coefficient that applies if a liquid slug is present and convectional heat transfer occurs. t_{conv} is the time interval in which a liquid slug was present. Consequently, HTC_{phase} and t_{phase} are HTC and time interval for phase change, respectively. Based on the above definition, fractional HTC values $HTC_{conv,frac}$ and $HTC_{phase,frac}$, that reflect on the fraction of heat transfer they caused, can be defined by

$$HTC_{conv,frac} = \frac{HTC_{conv}\Delta t_{conv}}{\Delta t_{total}}, \tag{7.11}$$

and

$$HTC_{phase,frac} = \frac{HTC_{phase}\Delta t_{phase}}{\Delta t_{total}}. \tag{7.12}$$

The fractional HTC values can be directly extracted from the simulation software. The heat transfer area and temperature difference can be considered constant in a quasi-steady state condition. Consequently, a fraction $\phi_{\text{phasechange}}$ is calculated that equals the fraction of heat transfer caused by phase change in the PHP, given by

$$\phi_{phasechange} = \frac{HTC_{phase,frac}}{HTC} = \frac{\dot{Q}_{phase}}{\dot{Q}_{total}}, \tag{7.13}$$

where $\dot{Q}_{\text{phase}}$ is the phase change heat transfer rate and $\dot{Q}_{\text{total}}$ is the total heat transfer rate. The results of $\phi_{\text{phasechange}}$ for different boundary conditions are plotted in figure 7.8.

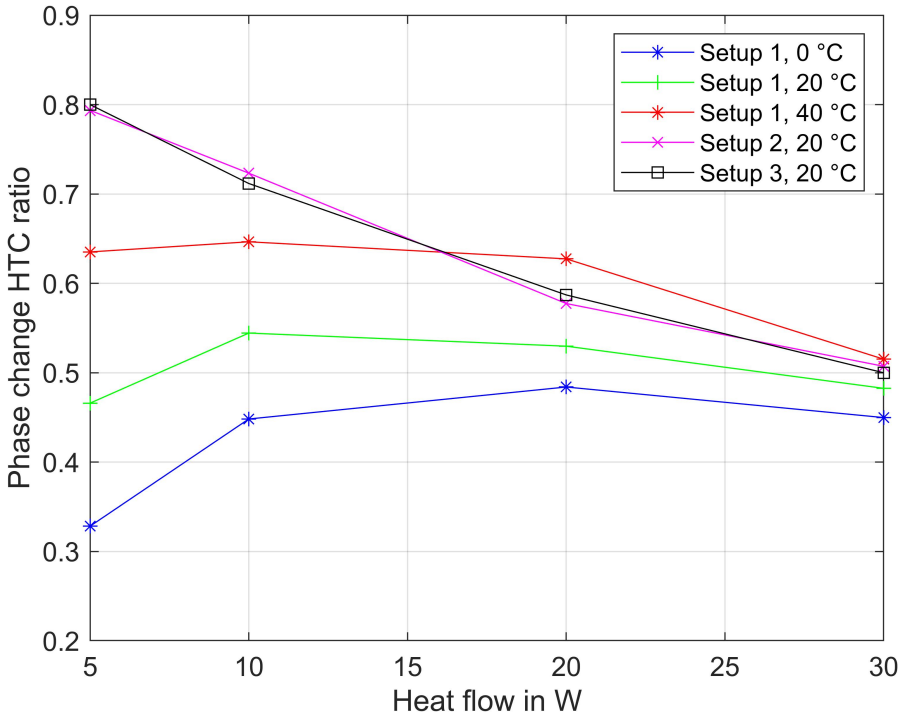

Figure 7.8: Phase change heat transfer ratio $\varphi_{phasechange}$ in simulations for different temperatures and test setups at 70% filling ratio

The ratio approaches 0.5 for high heat flow for all roughness values and condenser temperatures. At high heat flow, heat transportation by convective cooling of the liquid

slugs and phase change is approximately equal. For low heat flow rates, the ratio of phase change heat transport seems to increase with increasing roughness and condenser temperature. Thus, with decreasing nucleation threshold the ratio of phase change heat transportation increases at low heat flow. The improved thermal resistances at low nucleation thresholds and low heat flow, therefore, seem to be mainly caused by an improved evaporation and condensation behavior.

The simulation also allows to evaluate heat transfer coefficients locally. Therefore, the heat transfer coefficients in the evaporator area $\mathrm{HTC}_{\mathrm{evap}}$ and in the condenser area $\mathrm{HTC}_{\mathrm{cond}}$ can be compared. The ratio ϕ_{evap} between the two values is defined by

$$\phi_{evap} = \frac{HTC_{evap}}{HTC_{cond}}. \tag{7.14}$$

The results are depicted in figure 7.9.

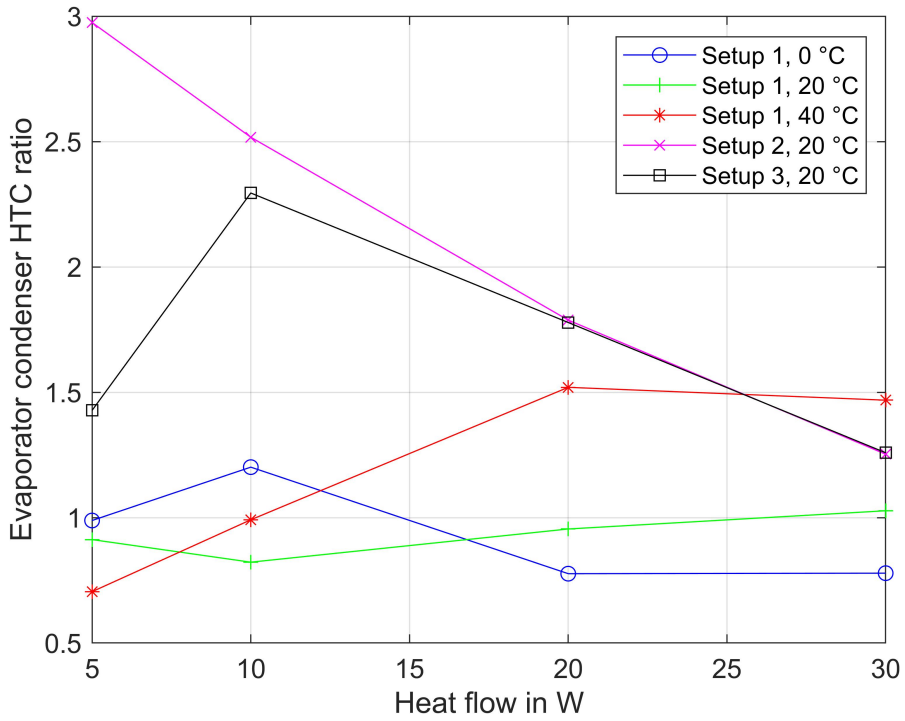

Figure 7.9: Evaporator condenser HTC ratio φ_{evap} in simulations for different temperatures and test setups at 70% filling ratio

At 0°C and 20°C condenser temperature for test setup 1 the ratio was close to 1 for all

heat flow rates. At high heat flow, setup 1 showed a trend of increased evaporator HTC for higher condenser temperatures. The rougher test setups 2 and 3 both show increased ratios at low heat flow rates, most pronounced for test setup 2. Therefore, rough surface area seems to enhance the heat transfer coefficient especially in the evaporator area.

7.3 Oscillation frequencies

The changes in heat transfer coefficient were further analyzed. Sensible and latent heat can only be transported from evaporator to condenser section if the slug-plug flow oscillates back and forth between the two sections. The higher the frequency of the oscillations, the more heat can be transported, and heat transfer coefficients will also be enhanced. Therefore, the flow velocities need to be further investigated. As the flow in a PHP is quite chaotic, it has different velocities at different locations at the same time, sometimes even different flow directions. The flow velocities must, therefore, be evaluated locally instead of using an average value. The six evaporator bends are chosen as the locations for velocity evaluation here. All positions are regarded separately. The flow velocities at each location can be tracked with time. An example profile can be seen in figure 7.10a.

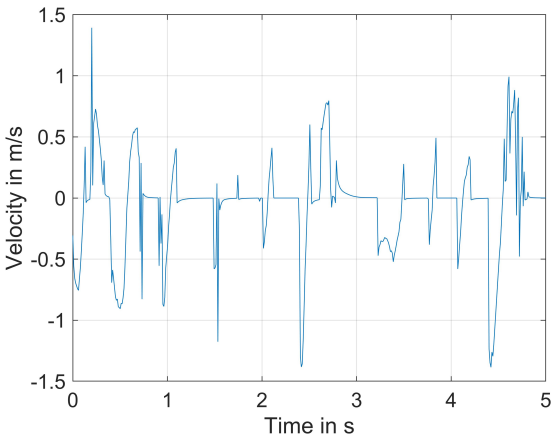

(a) Velocity profile in third evaporator bend from the left for test setup 3, filling ratio 70%, 20◦C, and 10 W

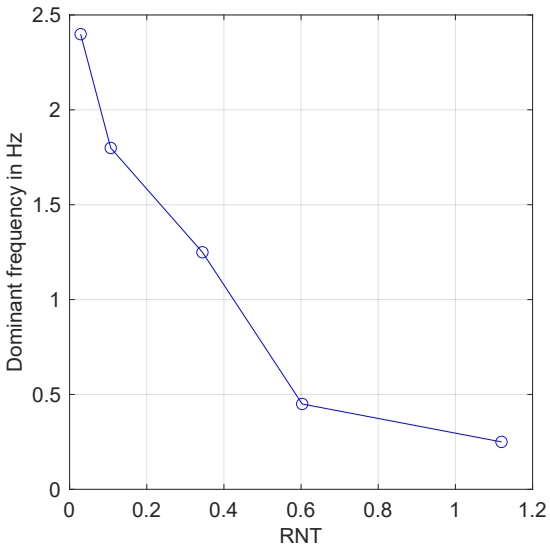

(b) Dominant frequency of PHP at 10 W for different RNT values at third evaporator bend

Figure 7.10: Frequency analysis in simulations

This profile was recorded in the third evaporator bend from the left with roughness values from test setup 3, a filling ratio of 70%, 20°C condenser temperature and 10 W heat flow. The profile looks quite ra gged. Changes in flow direction seem to occur quite suddenly with high acceleration. Flow velocities up to 1.4 m/s are reached.

The velocity profiles were further analyzed with a Fast-Fourier-Transformation (FFT) to determine dominant frequencies for each case. It is noted that the dominant frequencies are analyzed separately in each evaporator bend for the same boundary conditions. However, in the investigated cases, the dominant frequencies were always equal in each evaporator bend. Therefore, a common dominant frequency could be assigned to the whole PHP for each set of boundary conditions. Other researchers [12] have already shown that the dominant frequency increases with an increasing heat flow. In this study, the heat flow is, therefore, kept constant at 10 W and the influence of bubble nucleation threshold on the dominant oscillation frequency is investigated. Therefore, condenser temperature and surface roughness are varied for this study. For all cases, a relative nucleation threshold was calculated. As the heat flow is kept constant here, the different RNT values only reflect on changes of bubble nucleation threshold. The results can be seen in figure 7 .10b. It can be observed that the dominant frequency increases considerably with decreasing RNT. Therefore, reduced bubble nucleation threshold leads to higher oscillation frequencies and enhanced pulsating motion within the PHP. The results give a good indication to why heat transfer coefficients and ultimately the overall thermal resistance of the PHP is effected by the bubble nucleation threshold.

7.4 Liquid mass fractions

The liquid mass fraction (LMF) in the evaporator area is analyzed in the simulations. LMF is defined as the time averaged fraction of liquid mass present at the evaluated location. If a liquid slug is present, the momentary value would be 1 and if a vapor plug passes, the value would be close to 0. The average value, therefore, approximates the fraction of time a liquid slug was present in the evaluated region. As bubbles in the evaporator can only be nucleated if a liquid slug is present, the LMF value in the evaporator area is of particular interest. For the evaluation, LMF was averaged over 20 s of simulation time. The results can be seen in figure 7.11.

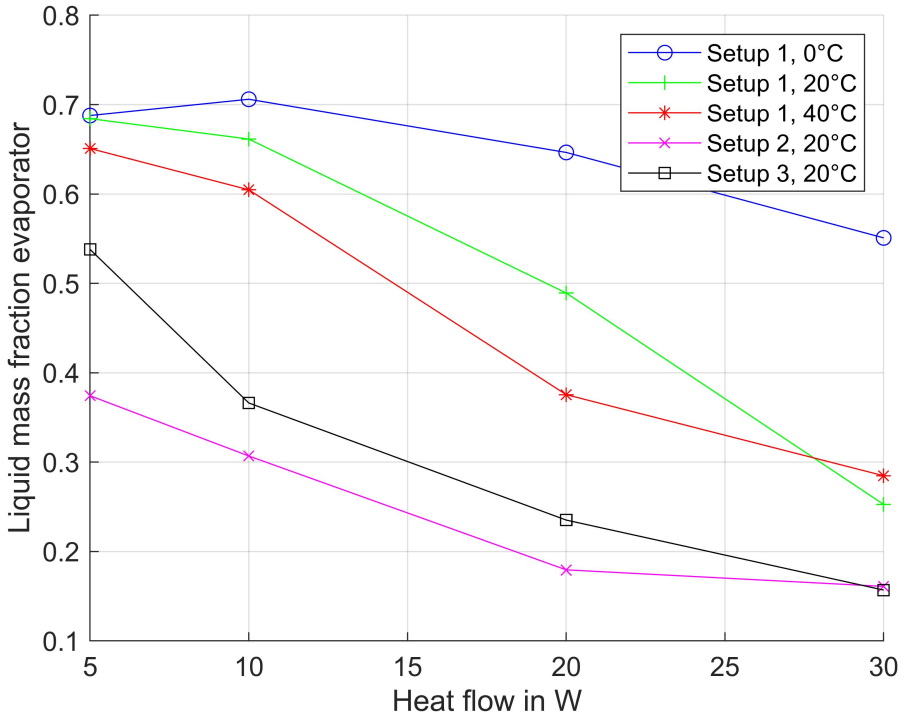

Figure 7.11: Liquid mass fraction in evaporator section LMF in simulations for different temperatures and test setups at 70% filling ratio

It can be observed that higher heat flow leads to lower liquid mass fractions in the evaporator area for all boundary conditions. Similarly, higher condenser temperature and surface roughness seem to result in lower liquid mass fractions. Therefore, the dependency of LMF on the relative nucleation threshold is worth investigating. Figure 7.12 shows the LMF values of the simulations with respect to their RNT values.

Higher relative nucleation threshold leads to increased LMF. The increase is very steep at low RNT values and becomes less steep for higher RNT values. In fact, LMF is approaching a limit value of approximately 0.7 for high RNT values. As 0.7 is also the filling ratio used for the simulations, it must be analyzed, whether it is reasonable to assume the limit value as equal to the filling ratio. Simulations at 50% and 30% filling ratio, though not experimentally validated, suggest that the limit value is indeed equal to the filling ratio. The associated simulation results can be found in appendix 10.5.

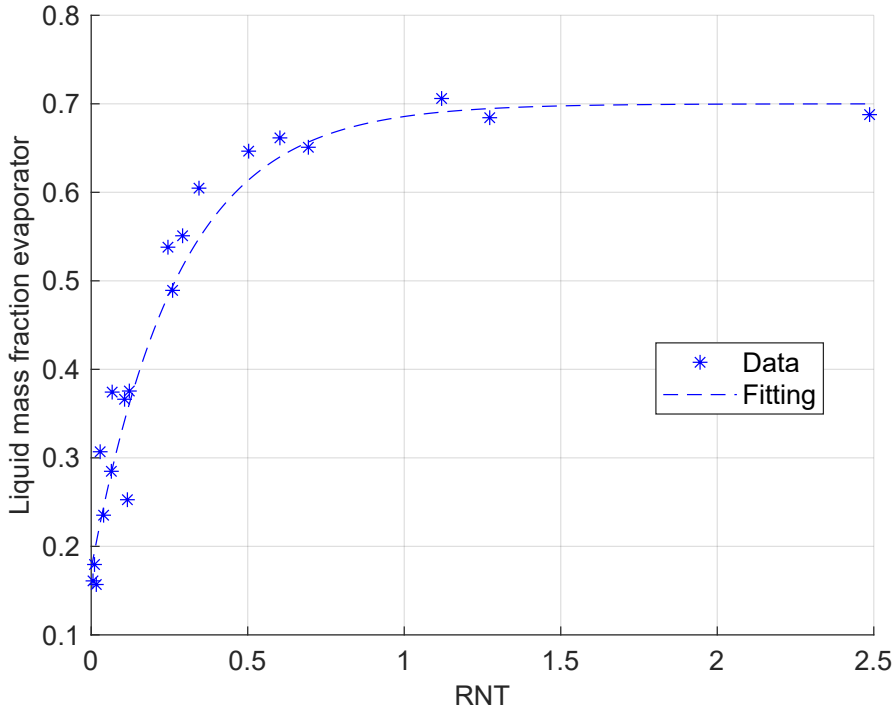

Figure 7.12: Liquid mass fraction in evaporator section in simulations for different temperatures and test setups at 70% filling ratio with respect to RNT

Subsequently, LMF can be approximated by a fitting function using an exponential limited growth approach. It is calculated by

$$LMF(RNT) = a \cdot \exp(b \cdot RNT) + FR, \tag{7.15}$$

where the fitting coefficients were found to be a=-0.5253 and b=-3.599. FR is the filling ratio and used as a limit value. From the fitting equation for 70% filling ratio it can be derived that LMF approaches the value FR + a = 0.7 − 0.5253 = 0.1747 when RNT approaches zero.

In chapter 6.2 it was found that the bubble nucleation rates increase with decreasing relative nucleation threshold, starting at high values of RNT. This seems reasonable, as decreased nucleation threshold allows for more bubbles to be nucleated in a liquid slug passing through the evaporator section. The trend was expected to continue until reaching a maximum value at RNT=0. However, it was found, that the maximum is reached at a higher RNT value around RNT=0.3. For RNT<0.3, the bubble nucleation

rate decreased until reaching close to zero for an RNT=0. The decrease was expected to be a result of a decreased amount of liquid available in the evaporator section. However, the theory could only be confirmed qualitatively in the experiments, as the liquid mass fraction in the evaporator area could not be extracted from the high-speed recordings. The simulations support the theory and show that the liquid mass fraction in the evaporator area decreases with decreasing RNT. The decrease is particularly steep when approaching RNT=0. Consequently, a term for the bubble nucleation rate BNR_{slug} could be found that would apply if the evaporator area was permanently and completely filled with liquid. The empirically fitted term is, thus,

$$BNR_{slug} = 1.5(8000 - 4500RNT^{1.5})^{1.05}. \tag{7.16}$$

To get the real bubble nucleation rate, the term BNR_{slug} needs to be multiplied by the modified liquid mass fraction LMF_{mod} that is defined by

$$LMF_{mod} = LMF - LMF(RNT = 0) = LMF - (FR + a). \tag{7.17}$$

The shift by LMF(RNT=0) in the modification is assumed to be necessary, as for very low liquid mass fractions (below 0.1747 in this case) the distances between the bubble nucleation and the nearest Taylor bubble are so small that new bubbles merge immediately into the Taylor bubble, before being released from the wall. Also, bubble nucleation within the liquid film occurs regularly in areas of thicker liquid film for very low RNT values. They also merge immediately into the neighboring Taylor bubble before being released from the wall. The real bubble nucleation rate is finally calculated by the product of BNR_{slug} and LMF_{mod}. For 70% filling ratio this yields

$$BNR = BNR_{slug}LMF_{mod} = 1.5(8000 - 4500RNT^{1.5})^{1.05}(LMF - LMF(RNT = 0)). \tag{7.18}$$

This modelling approach is assumed to cover the physical phenomena quite well and matches qualitative observations in the video recordings. Figure 7.13 shows the measured bubble nucleation rates with respect to RNT as well as the fitting function explained in this chapter. Also shown is the theoretical equation for the bubble nucleation rate in an evaporator filled permanently with liquid phase BNR_{slug}. It can be seen that BNR_{slug} rises monotonously from high to low RNT values.

It should be noted that the fitting of BNR_{slug} is applied to data from this specific geometry in vertical bottom-heated orientation, with refrigerant R1233zd(E) at a filling ratio of 70%. Although it is expected to be valid for different filling ratios as well, this could not yet be shown experimentally, as the bubble nucleation rates for 50% and 30% could not be evaluated accurately. However, the fitting covers measurement data at different heat flow rates, condenser temperatures, and surface roughness values.

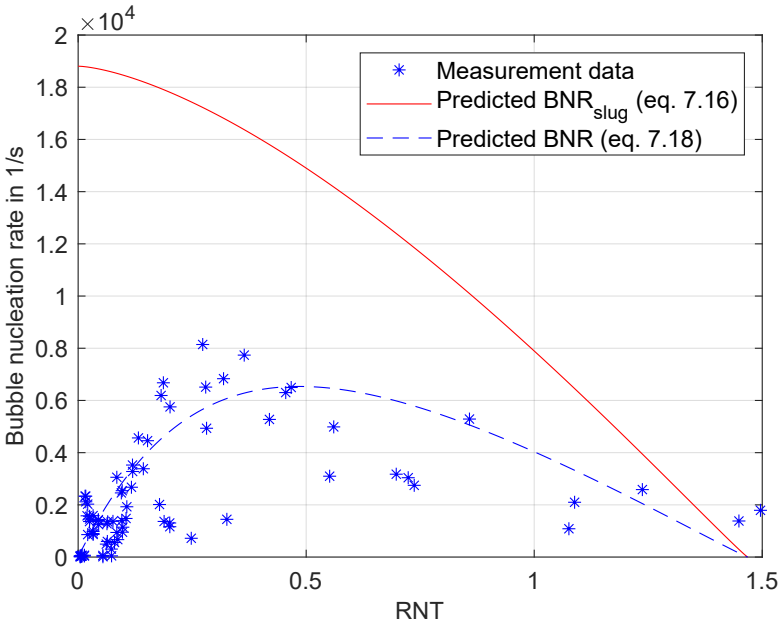

Figure 7.13: Fitting of bubble nucleation rates for filling ratio 70%

The findings support the theory presented in chapter 6 . It appears that even for RNT < 0.3, the correlation can be used to predict the behavior of a PHP. The decrease in bubble nucleation rate towards RNT=0 could be explained by a decrease in liquid mass fraction in the evaporator in this range. Therefore, less bubbles are nucleated due to the absence of liquid, even though the relative nucleation threshold is further decreased. All in all, it can be summarized, that the trend of bubble nucleation rates found in chapter 6.2 does not contradict the statement, that overall PHP performance is mainly dependent on the relative nucleation threshold.

7.5 Geometry variations

The range of validity of the correlation between the relative thermal resistance and the relative nucleation threshold presented in chapter 6.1 is limited to an identical channel geometry. Though significant in understanding the working principle of a PHP, it cannot be used to predict thermal resistances of a different geometry and, thus, cannot be used as a design tool for real applications. Geometry variations present a high challenge in experimental investigations, as each geometry requires a separate test setup. Therefore,

the influence of a few geometry parameters is investigated numerically in this work.

The goal of the investigation is to see whether the correlation can be used for other geometries as well or which changes would be required to the correlation. The geometrical changes in this work focus on the evaporator region. It is assumed that evaporator length and number of turns are important parameters in influencing the PHP behavior. Thus, these two parameters are varied while other parameters such as condenser and adiabatic length as well as channel width and height are kept constant.

Because the simulations showed highest accuracy for 70% filling ratio, this parameter is also kept constant. Firstly, a heat flow of 10 W with channel numbers 12, 16, and 24 and evaporator lengths of 10 mm and 30 mm are considered. The simulations yield thermal resistances for these boundary conditions that can be found in figure 7.14. Both increased channel number and evaporator length led to a reduced thermal resistance.

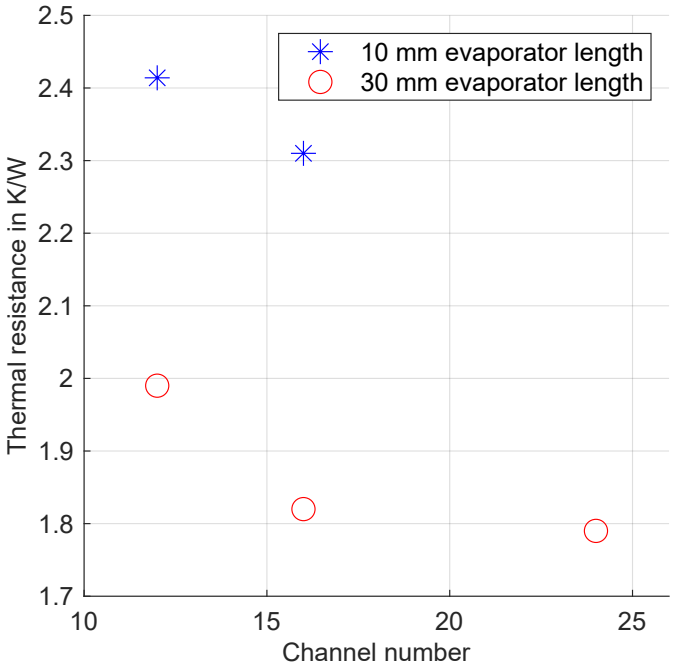

Figure 7.14: Simulated thermal resistances for different evaporator lengths and channel numbers for the roughness of test setup 1, 20◦C condenser temperature, 70% filling ratio, and 10 W heat flow rate

The number of channels $n_{channels}$ and evaporator length L_{evap} both influence the total length of channel within the evaporator area. The total evaporator channel lengths

$L_{evap,total}$ are calculated for each geometrical setup by

$$L_{evap,total} = n_{channels} L_{evap}. \tag{7.19}$$

Figure 7.15 shows the simulated thermal resistances with respect to the total evaporator channel length. It can be seen that the thermal resistance directly depends on $L_{evap,total}$, where increasing $L_{evap,total}$ leads to lower thermal resistances.

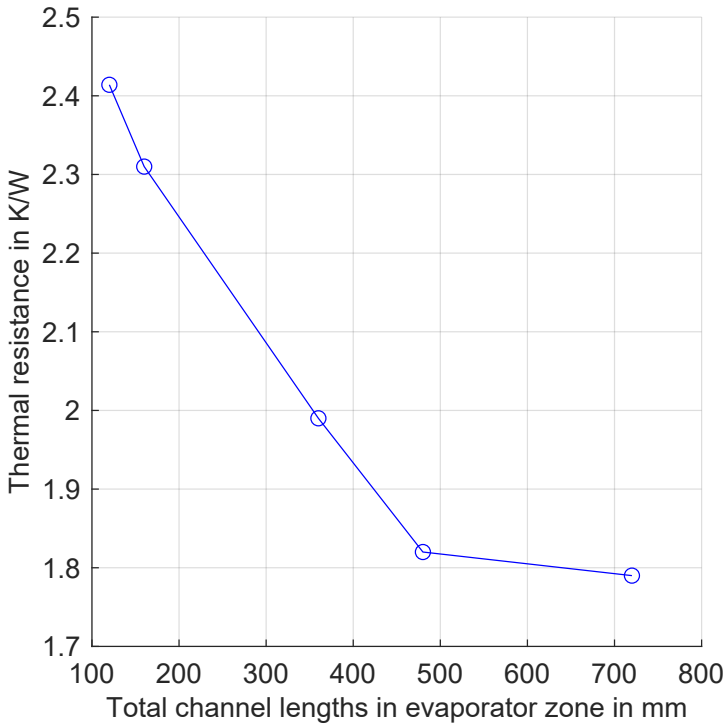

Figure 7.15: Simulated thermal resistances for different evaporator channel lengths for the roughness of test setup 1, 20◦C condenser temperature, 70% filling ratio, and different heat flow rate

To check the correlation from chapter 6.1 for validity for different geometries, the nucleation thresholds are calculated for each of the simulations presented above. To further calculate the relative nucleation thresholds, a thermal resistance of the empty (non-operational) PHP $R_{th,true}$ is needed for each geometrical setup. For simplification, $R_{th,true}$ is estimated to be anti-proportional to the number of channels, as the cross-sectional

area of wall material increases linearly with the number of parallel channels. The non-operational thermal resistance for 12 channels (measured in chapter 4.4) is 4.35 K/W. $R_{th,true}$ is, therefore, defined by

$$R_{th,true} = 4.35 \frac{12}{n_{channels}} \frac{K}{W}. \tag{7.20}$$

Additional simulations with 12, 16, 20, and 24 channels, 5 W, 7 W, 10 W, and 30 W heat flow, and 10 mm and 30 mm evaporator lengths were conducted. The values for $R_{th,true}$, as calculated by equation 7.20, are further used to calculate the relative thermal resistances and relative nucleation thresholds for all simulation results. The results are depicted in figure 7.16. Next to the data points, the correlation discovered in chapter 6.1 is shown here. The correlation fits reasonably well for high RNT values but shows considerable differences at low and medium RNT values. It can be concluded that the correlation cannot be used for a different geometry in the current form.

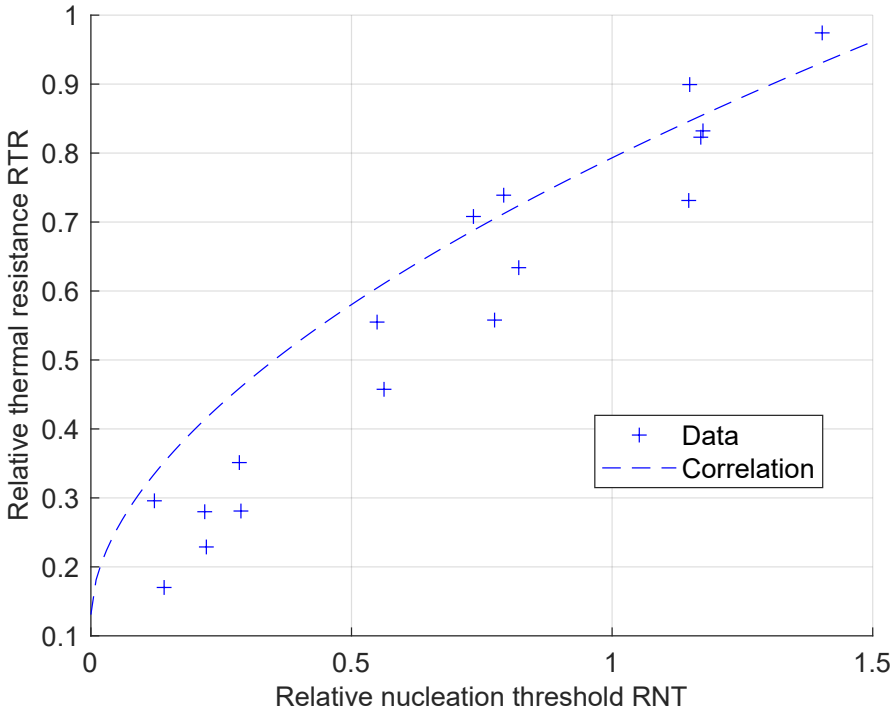

Figure 7.16: Simulated relative thermal resistances RTR for different relative nucleation thresholds RNT in comparison with the experimental correlation

To simplify the design process of a PHP for real applications, the next section focuses on finding a pragmatic modification of the correlation that extends its range of validity to variations in channel number and evaporator length. The data presented above is used to empirically fit a modelling approach. As a dependency of the thermal resistance on the total evaporator channel length was visible in figure 7.15, a modification of the previously used correlation based on changes in evaporator channel length is needed. To enable the use of the same correlation for different geometries, a modified input heat flow rate $\dot{Q}_{\mathrm{mod}}$ is calculated in an approach to cover this influence. $\dot{Q}_{\mathrm{mod}}$ is calculated by

$$\dot{Q}_{mod} = \dot{Q}_{corr}\left(\frac{L_{evap,total}}{0.12m}\right)^{(1.3-RNT)}. \tag{7.21}$$

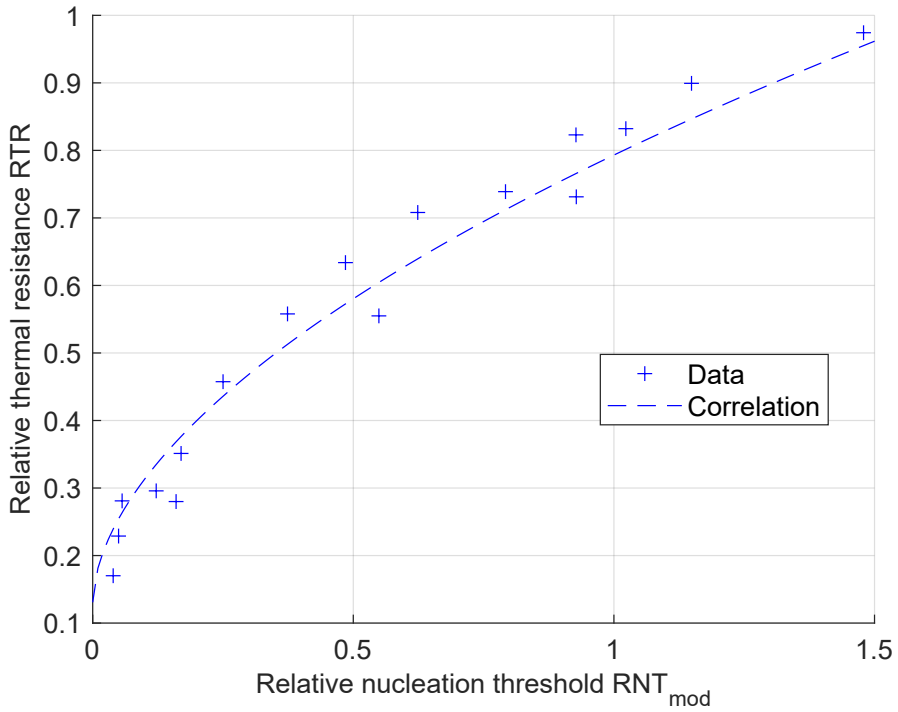

Figure 7.17: Simulated relative thermal resistances RTR for different modified relative nucleation thresholds RNTmod in comparison with the experimental correlation

$\dot{Q}_{\mathrm{corr}}$ is the actual input heat flow rate and $L_{\mathrm{evap,total}}$ is the total length of evaporator channel. RNT is the regular, unmodified relative nucleation threshold, calculated for the

actual input heat flow rate. This simple modification of the input heat flow by the ratio of the total evaporator channel length of the new design to a reference design with 0.12 m of evaporator channel length enables the use of the same correlation even for other geometries. The modified relative nucleation threshold is then calculated by

$$RNT_{mod} = \frac{\Delta T_{nucleation}}{\dot{Q}_{mod} R_{th,true}}. \tag{7.22}$$

Subsequently, the same data points as in figure 7.16 are plotted with respect to their RNT_{mod} values in figure 7.17. The data shows good agreement with the correlation.

Lastly, the modified version of the correlation is tested for predicting the thermal resistances of a new and unknown design. A design with 32 channels and an evaporator length of 15 mm is chosen for the trial. This combination was not part of the data, the modification of the correlation was built on. Therefore, the design can be used as a validation. The non-operational thermal resistance $R_{th,true}$ of the test case can be estimated with equation 7.20.

Because the fluid's saturation temperature is not yet known, it is assumed to be equal to the condenser temperature in the first iteration step. The condenser temperature is chosen to be 5°C and the fluid R1233zd(E) is used for the test case. Based on the fluid properties at this estimated saturation temperature, nucleation thresholds $T_{nucleation}$ and, consequently, RNT_{mod} values can be calculated as stated in equations 6.1, 6.2, 7.22, and 7.21 for a specified input heat flow and a given surface roughness of 0.5 μm for the test case. Using the correlation presented in equation 6.4 and the corresponding coefficients in table 6.1, a relative thermal resistance can be calculated. Combined with the estimated $R_{th,true}$ the real thermal resistance R_{th} was calculated. Based on R_{th}, the specified heat flow, and the condenser temperature, an evaporator temperature was predicted. As this prediction still assumes the fluid's saturation temperature to be equal to the condenser temperature, it is still very imprecise and a new estimation for the saturation temperature must be found by using the average value between the predicted evaporator and chosen condenser temperature. With the new estimation for the saturation temperature, the calculation is repeated from the beginning and reveals a new estimation for the thermal resistance, evaporator temperature, and the saturation temperature. The calculation is, therefore, an iterative process that converges after a few calculation steps. In some cases, numerical damping is needed for the values to converge. The thermal resistances predicted for the test case geometry and boundary conditions are plotted in figure 10.7 for multiple heat flow rates. Several data points of the same curve are then simulated by the 1D-simulation software. The simulation results are also depicted in the same figure. The values predicted by the iterative use of the modified correlation are in good agreement with the simulated values.

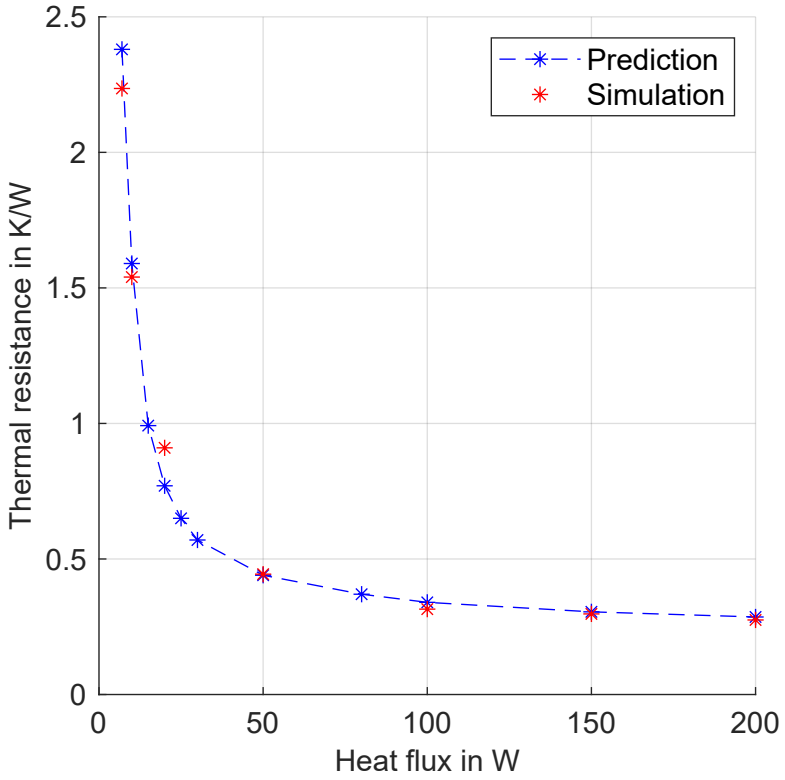

Figure 7.18: Correlation predictions for new geometry, roughness, and condenser temperature in comparison to simulation results

8 Summary and conclusions

8.1 Summary

Three geometrically identical transparent experimental setups were manufactured and investigated. They differed from each other by their inner channel surface roughness in the evaporator area. The surface structures were created by milling, sand blasting, and glass bead blasting. The surface structures were analyzed using a confocal and a newly introduced algorithm to evaluate the sizes of the surface cavities and derive representative bubble radii for the cavities. R1233zd(E) was used as a working fluid in the experiments with filling ratios of 30%, 50%, and 70%. Thermal resistances between evaporator and condenser area were measured.

It was found that increasing filling ratio resulted in a higher thermal resistance. Additionally, the condenser temperature was varied between 0°C, 20°C, and 40°C. Higher operating temperatures resulted in lower thermal resistances. It was further observed that different evaporator surface roughness had a major influence on the thermal resistance, most pronounced at low heat flow rates. Rougher surfaces produced lower thermal resistances. At high heat flow above around 30 W the difference between thermal resistances of different roughness values became very small.

From the bubble radii estimations derived from the confocal surface scans, the heat flow, and fluid properties at operating temperature, a newly introduced quantity, denominated here as relative nucleation threshold RNT, was calculated. For constant filling ratio, the measured thermal resistances correlated with the RNT values of the investigated operational points. This included measurements at different heat flow rates, condenser temperatures, and evaporator surface roughness. Such a correlation could be found for all three filling ratios in the experiments, although the correlation parameters are unique for each filling ratio. In general, the thermal resistance increases with increasing relative nucleation threshold. The gradient of this increase is highest for high filling ratios and becomes smaller with lower filling ratios. This matches the qualitative observations made by Sun et al. [54]. They also discovered in flow observations, that bubble nucleation is most important for operating a PHP at high filling ratios. For RNT values close to

zero, the thermal resistance reaches a minimum. The findings of this work also question the suitability of the correlation presented by Juno Kim and Sung Jin Kim [31]. They investigated the influence of fluid temperature on PHP performance and found that higher fluid temperature led to lower thermal resistance. They attributed the change to a steeper vapor pressure curve at high temperatures. Although the present work discovered the same influence on fluid temperature, it revealed a strong connection of the thermal resistance to the bubble nucleation threshold. Thus, the newly introduced correlation covers not only changes in fluid temperature but also roughness changes which were not covered by the correlation presented by Kim.

To analyze the bubble nucleation rates in the experiments, the PHP channels in the evaporator area were recorded with a high-speed camera. Using a bubble detection and motion tracking algorithm, the newly generated bubbles could be counted within the analyzed time interval. An average bubble nucleation rate was, therefore, derived for each analyzed set of boundary conditions. The bubble nucleation rates estimated for the measurements at 70% filling ratio depended on the relative nucleation threshold. From high RNT values down to approximately RNT=0.3, the bubble nucleation increased with decreasing RNT. For an RNT value of 0.3, a maximum bubble nucleation rate was reached. For small RNT values below 0.3, a further decrease in RNT led to a decrease in bubble nucleation rate. At low and especially medium heat flux, intensive bubble generation was observed. At high heat flux, the bubble nucleation rate decreased, and the flow was dominated by Taylor-bubbles. This is in good agreement with observations made by Qu et al. [56].

A 1D PHP simulation approach as published by Aubin et al. [13] was used to reconstruct the experimental setup in a virtual environment. It was found that for 70% filling ratio, various condenser temperatures, heat flow, and surface roughness values, the simulations were in good agreement with the experimental results. Lower filling ratios produced less accurate results. Therefore, only the simulations at 70% filling ratio were used to gain further insights into PHP behavior.

In a first step, heat transfer coefficients between the fluid and the channel walls were analyzed in the simulations. It could be shown that the heat transfer coefficient averaged over time and the full inner channel surface correlated with RNT. Lower RNT resulted in higher heat transfer coefficients.

The flow velocities were recorded and analyzed for their dominant frequencies. The oscillation frequency also depended on the relative nucleation threshold. For constant heat flow, a lower RNT value leads to higher oscillation frequencies. For the milled (smooth) evaporator the frequencies at 10 W were in a range of 0.25 to 1.25 Hz. This approximately matches the frequency range found by other researchers [12]. For the rougher sand and glass bead blasted evaporators, frequencies up to 2.4 Hz were reached for the same heat

flow.

To further explain the trend discovered for the bubble nucleation rates, liquid mass fractions (LMF) in the evaporator area were analyzed in the simulations. It was found that LMF also correlates with RNT. Close to an RNT value of zero, LMF reached a minimum value. For high RNT values, LMF approached the filling ratio. Based on this data, a theoretical bubble generation term was introduced and fitted empirically. It indicates the bubble nucleation rate that would apply if the evaporator was completely and permanently filled with liquid. The theoretical bubble generation term monotonously decreases with increasing RNT, which is the behavior that is expectable. Multiplied by a modified form of LMF, the bubble generation term models the actual bubble nucleation rate, as bubbles can only be nucleated if a liquid slug is present in the evaporator zone. The modelling approach of the bubble nucleation behavior successfully explained the trend of the bubble nucleation rate curve observed in the experiments.

Lastly, the number of channels and the evaporator channel length was varied in multiple simulations, to identify the influence of key geometrical parameters. It was found that the thermal resistance depended on the total channel length within the evaporator area.

8.2 Conclusions

The insights into PHP behavior obtained by the simulations indicate that it is plausible to use the correlation between thermal resistance and relative nucleation threshold that was found in the experiments. Thermal resistance, bubble nucleation rate, heat transfer coefficient, oscillation frequency, and liquid mass fraction in the evaporator can all be modelled based on RNT. This conclusion leads to the assumption that bubble nucleation has a major impact on PHP performance and might even be the major driving force. Even though film evaporation and liquid convection are the major heat transfer mechanisms present in a PHP, they are both governed mainly by the velocity profiles of the liquid slugs inside the PHP. The liquid convection is directly governed by the flow velocity and film evaporation is indirectly governed by the velocities as the slug velocity influences the initial film thickness at the trailing edge of a liquid slug. As the work of some researchers already indicates that high oscillation velocities and amplitudes are mainly caused by bubble nucleation [51] and bubble nucleation is responsible for maintaining the oscillations [53], this would implicate that bubble nucleation indirectly governs both heat transfer mechanisms.

This theory seems plausible when considering that a direct correlation between relative nucleation threshold and thermal resistance could be found in the experiments and other quantities such as oscillation frequency, liquid mass fraction, and heat transfer coefficients

could also be correlated to the relative nucleation threshold. However, these observations were so far only made for one geometrical setup and one working fluid. Therefore, further investigations with different channel geometries and working fluids, combined with the relevant confocal surface scans, should be made, to check whether the same correlation (with different coefficients) can also be found for these setups.

If it can indeed be shown that bubble nucleation is the major source of propulsion in a PHP, it is still likely that frictional losses have to be considered as a counter part to the propulsion. Therefore, total length of channel from evaporator to condenser, channel diameter, and fluid viscosity are also expected to influence the overall thermal resistance of a PHP. The conclusion is, therefore, that a correlation between thermal resistance and relative nucleation threshold generally exists, but the coefficients of the correlation change with several boundary conditions. Future works should focus on investigating these influences.

Lastly, an attempt was made to extend the correlation to the use with different channel geometries. The correlation was empirically fitted to account for a varying number of channels and evaporator lengths based on results obtained from 1D-simulations. Consequently, the modified correlation can now be used to predict thermal resistances of test setups in a narrow range of boundary conditions. Thus, it is possible to predict the behavior of test setups with rectangular channels of 1 mm by 1 mm with R1233zd(E) as a working fluid. It is possible to make predictions for different filling ratios, condenser temperature, number of channels, lengths of evaporators, heat flow, and surface roughness values. An experimental validation is required, however, to validate the modified version of the correlation. Different fluids, channel diameters, and total channel lengths are still expected to influence the parameters of the modified correlation, but it is assumed that a correlation of the presented form exists for all PHPs (even if the correlation parameters change). Therefore, the number of experiments needed for future application design work is reduced, as only a few experiments reveal the coefficients of the correlation, enabling the calculation of various other boundary conditions.

9 Bibliography

[1] R. Mahajan, R. Nair, V. Wakharkar, J. Swan, J. Tang, G. Vandentop, Emerging directions for packaging technologies, Intel Technology Journal 06 (02) (2002) 62–75.

[2] F. Chang, I. O., M. Lienkamp, L. Voss, Improving the overall efficiency of automotive inverters using a multilevel converter composed of low voltage si mosfets, IEEE Transactions on Power Electronics 34 (4) (2019) 3586–3602, doi: 10.1109/TPEL.2018.2854756.

[3] G. Domingues-Olavarria, P. Fyhr, A. Reinap, M. Andersson, M. Alaküla, From chip to converter: A complete cost model for power electronics converters, IEEE Transactions on Power Electronics 32 (2017) 8681–8692.

[4] V. Ayel, M. Slobodeniuk, R. Bertossi, C. Romestant, Y. Bertin, Flat plate pulsating heat pipes: a review on the thermohydraulic principles, thermal performances and open issues, Applied Thermal Engineering (2021). doi:https://doi.org/10.1016/j.applthermaleng.2021.117200.

[5] D. Bastakoti, H. Zhang, D. Li, W. Cai, F. Li, An overview on the developing trend of pulsating heat pipe and its performance, Applied Thermal Engineering 141 (2018) 305–332. doi:https://doi.org/10.1016/j.applthermaleng.2018.05.121.

[6] B. Corporation, Boyd two phase thermal solution guide, Boyd Corporation (2021).

[7] L. L. Vasiliev, Heat pipes in modern heat exchangers, Applied Thermal Engineering 25 (2005) 1–19, doi:10.1016/j.applthermaleng.2003.12.004.

[8] A. A. Attia, B. T. El-Assal, Experimental investigation of vapor chamber with different working fluids at different charge ratios, Ain Shams Engineering Journal 3 (2012) 289–297, doi:10.1016/j.asej.2012.02.003.

[9] G. Czerwinski, J. Woloszyn, Numerical study of a cooling system using phase change of a refrigerant in a thermosyphon, Energies 14, doi:10.3390/en14123634 (2021).

[10] X. Han, X. Wang, H. Zheng, X. Xu, G. Chen, Review of the development of pulsating heat pipe for heat dissipation, Renewable and Sustainable Energy Reviews 59 (2016) 692–709. doi:http://dx.doi.org/10.1016/j.rser.2015.12.350.

[11] Y. Zhang, A. Faghri, Advances and unsolved issues in pulsating heat pipes, Heat Transfer Engineering 29 (1) (2008) 20–44. doi:10.1080/01457630701677114.

[12] R. Perna, M. Mameli, A. Mariotti, L. Pietrasanta, M. Marengo, S. Filippeschi, Wavelet analysis of the pressure signal in a pulsating heat pipe, in: UIT Heat Transfer Conference, no. 37, 2019.

[13] P. Aubin, B. D'Entremont, F. Cataldo, J. Marcinichen, R. L. Amalfi, J. Thome, Numerical simulations of pulsating heat pipes, part 1: Modeling, 2019, pp. 232–242. doi:10.1109/ITHERM.2019.8757388.

[14] S. Khandekar, Thermo-hydrodynamics of closed loop pulsating heat pipes, Ph.D. thesis, University of Stuttgart, Institut für Kernenergetik und Energiesysteme (2004).

[15] M. Ebrahimi, M. B. Shafii, M. A. Bijarchi, Experimental investigation of the thermal management of flat-plate closed-loop pulsating heat pipes with interconnecting channels, Applied Thermal Engineering 90 (2015) 838–847. doi:http://dx.doi.org/10.1016/j.applthermaleng.2015.07.040.

[16] Q. Lu, L. Jia, Experimental study on rack cooling system based on a pulsating heat pipe, Journal of Thermal Science 25 (1) (2016) 60–67.

[17] H. K. S. Abad, M. Ghiasi, S. J. Mamouri, M. B. Shafii, A novel integrated solar desalination system with a pulsating heat pipe, Desalination 311 (2013) 206–210. doi:10.1016/j.rser.2012.03.030.

[18] H. N. Chaudhry, B. R. Hughes, S. A. Ghani, A review of heat pipe systems for heat recovery and renewable energy applications, Renewable and Sustainable Energy Reviews 16 (2012) 2249–2259. doi:10.1016/j.rser.2012.01.038.

[19] W. Srimuang, P. Amatachaya, A review of the applications of heat pipe heat exchangers for heat recovery, Renewable and Sustainable Energy Reviews 16 (2012) 4303–4315. doi:10.1016/j.rser.2012.03.030.

[20] H. Alizadeh, R. Ghasempour, M. B. Shafii, M. H. Ahmadi, W.-M. Yan, M. A. Nazari, Numerical simulation of pv cooling by using single turn pulsating heat pipe, International Journal of Heat and Mass Transfer 127 (2018) 203–208, https://doi.org/10.1016/j.ijheatmasstransfer.2018.06.108.

[21] E. Roslan, I. Hassim, Solar pv system with pulsating heat pipe cooling, Indonesian Journal of Electrical Engineering and Computer Science 14 (2019) 311–318, dOI: 10.11591/ijeecs.v14.i1.pp311-318.

[22] Q. Wang, Z. Rao, Y. Huo, S. Wang, Thermal performance of phase change material/oscillating heat pipe-based battery thermal management system, International Journal of Thermal Sciences 102 (2016) 9–16, http://dx.doi.org/10.1016/j.ijthermalsci.2015.11.005.

[23] T. Mito, K. Natsume, N. Yanagi, H. Tamura, Y. Terazaki, Enhancement of thermal properties of hts magnets using built-in cryogenic oscillating heat pipes, IEEE Transactions on Applied Superconductivity 23 (3) (2013) 4602905–4602905. doi:10.1109/TASC.2013.2251393.

[24] J. Qu, H. Wu, P. Cheng, Start-up, heat transfer and flow characteristics of silicon-based micro pulsating heat pipes, International Journal of Heat and Mass Transfer 55 (21) (2012) 6109–6120. doi:https://doi.org/10.1016/j.ijheatmasstransfer.2012.06.024.

[25] H. Yang, S. Khandekar, M. Groll, Performance characteristics of pulsating heat pipes as integral thermal spreaders, International Journal of Thermal Sciences 48 (4) (2009) 815–824. doi:https://doi.org/10.1016/j.ijthermalsci.2008.05.017.

[26] F. Schwarz, V. Danov, A. Lodermeyer, A. Hensler, S. Becker, Thermodynamic analysis of the dryout limit of oscillating heat pipes, energies 13 (2020) 6346, doi:10.3390.

[27] H. Xian, Y. Yang, D. Liu, X. Du, Heat transfer characteristics of oscillating heat pipe with water and ethanol as working fluids, Journal of Heat Transfer 132 (12) (2010).

[28] P. Charoensawan, P. Terdtoon, Thermal performance of horizontal closed-loop oscillating heat pipes, Applied Thermal Engineering 28 (5) (2008) 460–466. doi:https://doi.org/10.1016/j.applthermaleng.2007.05.007.

[29] C. Wilson, B. Borgmeyer, R. A. Winholtz, H. B. Ma, D. L. Jacobson, D. S. Hussey, M. Arif, Visual observation of oscillating heat pipes using neutron radiography,

Journal of Thermophysics and Heat Transfer 22 (3) (2008) 366–372. doi:10.2514/1.33758.

[30] M. A. Nazari, M. H. Ahmadi, R. Ghasempour, M. B. Shafii, How to improve the thermal performance of pulsating heat pipes: A review on working fluid, Renewable and Sustainable Energy Reviews 91 (2018) 630–638. doi:https://doi.org/10.1016/j.rser.2018.04.042.

[31] J. Kim, S. J. Kim, Experimental investigation on working fluid selection in a micro pulsating heat pipe, Energy Conversion and Management 205 (2020) 112462. doi:https://doi.org/10.1016/j.enconman.2019.112462.

[32] X. Wang, L. Jia, Experimental study on heat transfer performance of pulsating heat pipe with refrigerants, Journal of Thermal Sciences 25 (5) (2016) 449–453, dOI: 10.1007/s11630-016-0883-6.

[33] H. Fang, H. Yang, J. Wang, J. Li, J. Zou, Fractal characteristics of temperature oscillation in pulsating heat pipe under medium-low load, Huagong Xuebao/CIESC Journal 67 (4) (2016) 1251–1257.

[34] G. Spinato, N. Borhani, J. R. Thome, Operational regimes in a closed loop pulsating heat pipe, International Journal of Thermal Sciences 102 (2016) 78–88. doi:https://doi.org/10.1016/j.ijthermalsci.2015.11.006.

[35] M. Mameli, M. Manzoni, L. Araneo, S. Filippeschi, M. Marengo, Pulsating heat pipe in hyper-gravity conditions, Heat Pipe Science and Technology, An International Journal 6 (1-2) (2015) 91–109.

[36] L. Lu, Z.-H. Liu, H.-S. Xiao, Thermal performance of an open thermosyphon using nanofluids for high-temperature evacuated tubular solar collectors: Part 1: Indoor experiment, Solar Energy 85 (2) (2011) 379–387. doi:https://doi.org/10.1016/j.solener.2010.11.008.

[37] Y. Hu, T. Liu, X. Li, S. Wanf, Heat transfer enhancement of micro oscillating heat pipes with self-rewetting fluid, International Journal of Heat and Mass Transfer 70 (2014) 496–503, http://dx.doi.org/10.1016/j.ijheatmasstransfer.2013.11.031.

[38] X. Wang, H. Zheng, M. Si, X. Han, G. Chen, Experimental investigation of the influence of surfactant on the heat transfer performance of pulsating heat pipe, International Journal of Heat and Mass Transfer 83 (2015) 586–590. doi:https://doi.org/10.1016/j.ijheatmasstransfer.2014.12.010.

[39] L. Betancur, D. Mangini, M. Mantelli, M. Marengo, Experimental study of thermal performance in a closed loop pulsating heat pipe with alternating superhydrophobic channels, Thermal Science and Engineering Progress 17 (2020) 100360, https://doi.org/10.1016/j.tsep.2019.100360.

[40] C.-Y. Tseng, K.-S. Yang, K.-H. Chien, M.-S. Jeng, C.-C. Wang, Investigation of the performance of pulsating heat pipe subject to uniform/alternating tube diameters, Experimental Thermal and Fluid Science 54 (2014) 85–92, http://dx.doi.org/10.1016/j.expthermflusci.2014.01.019.

[41] S. Thompson, H. Ma, C. Wilson, Investigation of a flat-plate oscillating heat pipe with tesla-type check valves, Experimental Thermal and Fluid Science 35 (7) (2011) 1265–1273. doi:https://doi.org/10.1016/j.expthermflusci.2011.04.014.

[42] B. Agostini, D. Torresin, M. Bortolato, Influence of the manifold configuration of pulsating heat pipes on their performance, Journal of Engineering Physics and Thermophysics 92 (4) (2019) 1008–1015, dOI 10.1007/s10891-019-02014-5.

[43] S. Pouryoussefi, Y. Zhang, Numerical investigation of chaotic flow in a 2d closed-loop pulsating heat pipen, Applied Thermal Engineering 98 (2016) 617–627.

[44] P. Pachghare, A. Mahalle, Thermo-hydrodynamics of closed loop pulsating heat pipe: an experimental study, Journal of Mechanical Science and Technology 28 (2014) 3387–3394.

[45] D.-T. Vo, H.-T. Kim, J. Ko, K.-H. Bang, An experiment and three-dimensional numerical simulation of pulsating heat pipes, International Journal of Heat and Mass Transfer 150 (2020) 119317. doi:https://doi.org/10.1016/j.ijheatmasstransfer.2020.119317.

[46] V. S. Nikolayev, Physical principles and state-of-the-art of modeling of the pulsating heat pipe: A review, Applied Thermal Engineering 195 (2021) 117111, https://doi.org/10.1016/j.applthermaleng.2021.117111.

[47] P. Cheng, H. Ma, A mathematical model of an oscillating heat pipe, Heat Transfer Engineering 32 (11-12) (2011) 1037–1046. doi:10.1080/01457632.2011.556495.

[48] A. Yoon, S. J. Kim, Characteristics of oscillating flow in a micro pulsating heat pipe: Fundamental-mode oscillation, International Journal of Heat and Mass Transfer 109 (2017) 242–253, http://dx.doi.org/10.1016/j.ijheatmasstransfer.2017.02.003.

[49] V. S. Nikolayev, A dynamic film model of the pulsating heat pipe, Journal of Heat Transfer 133 (8) (2011).

[50] B. P. d'Entremont, J. R. Thome, A Numerical Study of Pulsating Heat Pipe Performance Volume 3: Advanced Fabrication and Manufacturing; Emerging Technology Frontiers; Energy, Health and Water- Applications of Nano-, Micro- and Mini-Scale Devices; MEMS and NEMS; Technology Update Talks; Thermal Management Using Micro Channels, Jets, Sprays (07 2015). doi:10.1115/IPACK2015-48350.

[51] R. Senjaya, T. Inoue, Oscillating heat pipe simulation considering bubble generation part i: Presentation of the model and effects of a bubble generation, International Journal of Heat and Mass Transfer 60 (2013) 816–824. doi:http://dx.doi.org/10.1016/j.ijheatmasstransfer.2013.01.059.

[52] R. Senjaya, T. Inoue, Oscillating heat pipe simulation considering dryout phenomena, Heat and Mass Transfer 50 (10) (2014) 1429–1441. doi:10.1007/s00231-014-1354-9.

[53] I. Nekrashevych, V. S. Nikolayev, Effect of tube heat conduction on the pulsating heat pipe start-up, Applied Thermal Engineering 117 (2017) 24–29. doi:https://doi.org/10.1016/j.applthermaleng.2017.02.013.

[54] Q. Sun, J. Qu, J. Yuan, H. Wang, Start-up characteristics of mems-based micro oscillating heat pipe with and without bubble nucleation, International Journal of Heat and Mass Transfer 122 (2018) 515–528. doi:https://doi.org/10.1016/j.ijheatmasstransfer.2018.02.003.

[55] Q. Cai, C.-L. Chen, J. F. Asfia, Heat Transfer Enhancement of Planar Pulsating Heat Pipe Device Heat Transfer, Volume 2 (2006) 153–158. doi:10.1115/IMECE2006-13737.

[56] J. Qu, Q. Sun, H. Wang, D. Zhang, J. Yuan, Performance characteristics of flat-plate oscillating heat pipe with porous metal-foam wicks, International Journal of Heat and Mass Transfer 137 (2019) 20–30. doi:https://doi.org/10.1016/j.ijheatmasstransfer.2019.03.107.

[57] L. A. Betancur-Arboleda, J. P. Flórez Mera, M. Mantelli, Experimental study of channel roughness effect in diffusion bonded pulsating heat pipes, Applied Thermal Engineering 166 (2020) 114734. doi:https://doi.org/10.1016/j.applthermaleng.2019.114734.

URL https://www.sciencedirect.com/science/article/pii/S1359431119357679

[58] Y. Frey, A. Dörr, M. Lorenz, Experimental investigation of pulsating heat pipes with different evaporator roughness values, Applied Thermal Engineering 233 (2023) 120999. doi:https://doi.org/10.1016/j.applthermaleng.2023.120999.

[59] S. Khandekar, N. Dollinger, M. Groll, Understanding operational regimes of closed loop pulsating heat pipes: an experimental study, Applied Thermal Engineering 23 (2003) 707–719.

[60] Solstice zd.
URL https://www.climalife.co.uk/docs/Solstice-zd-FP-EN.pdf

[61] C. Kondou, N. Ryuichi, N. Nii, S. Koyama, Y. Higashi, Surface tension of low gwp refrigerants r1243zf, r1234ze(z), and r1233zd(e), International Journal of Refrigeration (2015) 80–89.

[62] M. E. Mondejar, M. O. McLinden, E. W. Lemmon, Thermodynamic properties of trans-1-chloro-3,3,3-trifluoropropene (r1233zd(e)): Vapor pressure, p-rho-t data, speed of sound measurements and equation of state, Journal of Chemical and Engineering Data (2013).

[63] Leader Tech, LT Product Profile Thermal Gap Fillers (2015).

[64] H.-J. J. et al., Quality assurance of harms and moems surface structures using confocal white light miroscopy, in: H. P. H. Ernst-Bernhard Kley (Ed.), Lithographic and Micromachining Techniques for Optical Component Fabrication, Vol. Proceedings of SPIE Vol. 4440, 2001.

[65] C. M. Rao, K. Venkatasubbaiah, K. J. Rao, Experimental investigation of surface roughness characteristics ra, rq and rz, International Journal of Hybrid Information Technolo 9 (7) (2016) 373–388.

[66] K.-D. Sommer, B. R. L. Siebert, Praxisgerechtes bestimmen der messunsicherheit nach gum (practical determination of the measurement uncertainty under gum), Technisches Messen 71 (2) (2004) 52–66, doi: https://doi.org/10.1524/teme.71.2.52.27068.

[67] Keysight Technologies, U1280 Series Handheld Digital Multimeters, published in USA (8 2020).

[68] National Instruments, NI-9219 Specifications (December 2021).

10 Appendix

10.1 3D surface scans

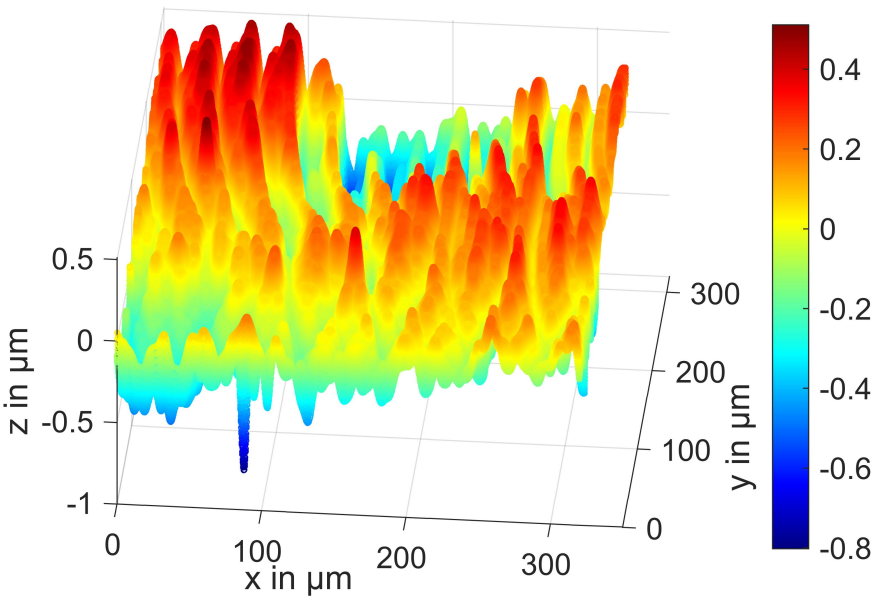

Figure 10.1: Test setup 1: 3D surface plot (lowpass filtered)

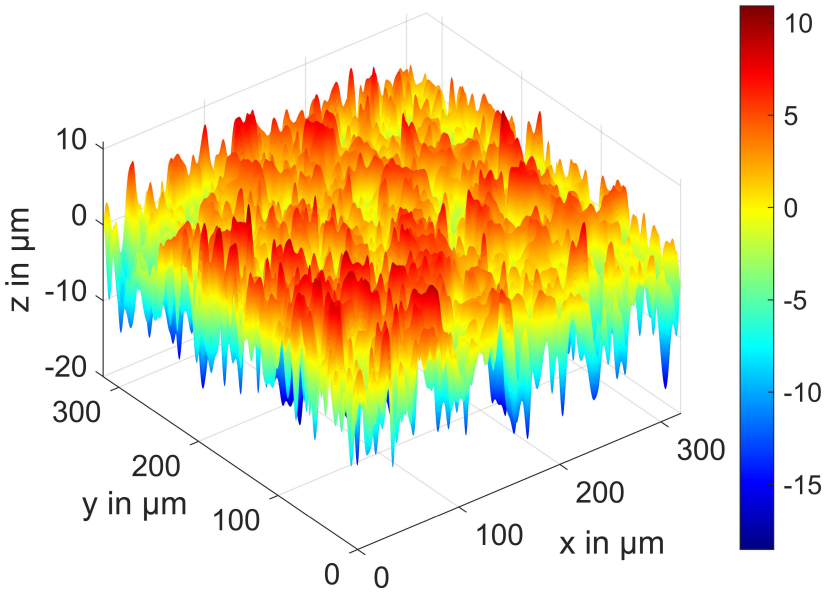

Figure 10.2: Test setup 2: 3D surface plot (lowpass filtered)

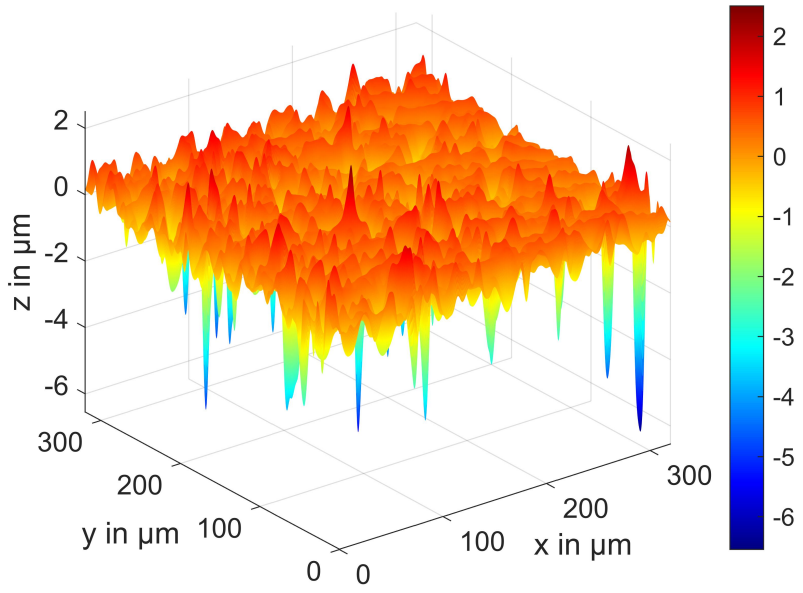

Figure 10.3: Test setup 3: 3D surface plot (lowpass filtered)

10.2 Measurement equipment details

The thermal measurement system includes type k sheath thermocouples with a diameter of 0.25 mm that are attached to the test setups. To measure the thermocouple temperatures, two National Instruments 9214 modules are used in the data acquisition rack system. The modules have each a cold-junction temperature measurement. Errors can be caused in the thermal measurement system by the modules and data acquisition, thermocouples, the cables, and the cable connections. To minimize the measurement error, the full measurement system is calibrated directly before the experiments. Therefore, all the possible measurement errors mentioned are eliminated and the measurement error will be as small as the error of the reference sensor used during the calibration and the procedure errors that can occur during the calibration. For the calibration process, the block calibrator Isotech Europa Venus Calisto is used. Next to the measurement error of the reference sensor (which is almost negligible), the possible error in the calibration procedure has to be considered. Therefore, a precise accredited calibration procedure with

detailed instructions was followed. The procedure is well tested and has a certified maximum error. After the calibration, the error of a thermocouple is equal to the error of the certified calibration procedure. This error depends on the measurement temperature. In the relevant temperature range from zero to one hundred degrees Celsius, the error is ± 0.08 K according to the calibration certificate. Figure 10.4 shows the calibration curve of two example sensors.

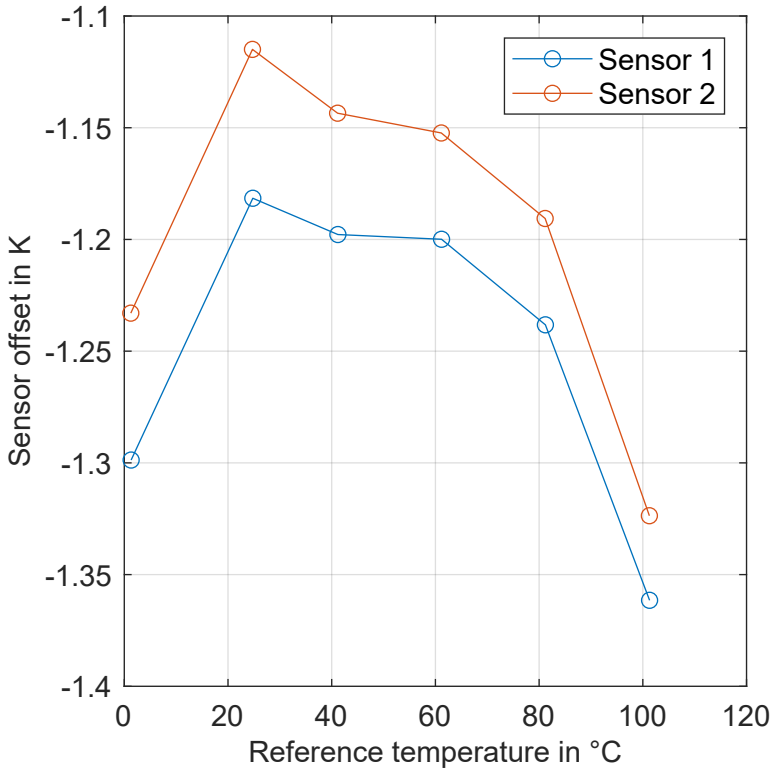

Figure 10.4: Thermocouple calibration example

The sensor offset is calculated by subtracting the sensor reading from the reference sensor reading. In this case, the sensors showed higher values than the reference sensor. The measurement values of the sensors in the experiments, therefore, need to be corrected by adding the offset value detected in the calibration process. For all temperature values between two calibration points, a linear interpolation of the offset value is done. In addition to the uncertainty of the calibration process, an interpolation error is added. The worst interpolation error is equal to the maximum

difference between two neighboring calibration offset values, which is approximately 0.08 K. The interpolation error of ±0.08K added to the calibration error of also ±0.08K yields a total uncertainty of ±0.16 K for each thermocouple.

The electrical power measurement consists of a voltage and a current measurement. The voltage measurement is done with a parallel circuit to the heater to avoid measuring the voltage drop in the cables. Therefore, the voltage measuring circuit is attached directly at the positive and negative poles of the heater. The actual voltage reading is done with a NI 9219 universal measurement module, programmed to voltage measurement in the range of ±65 V.

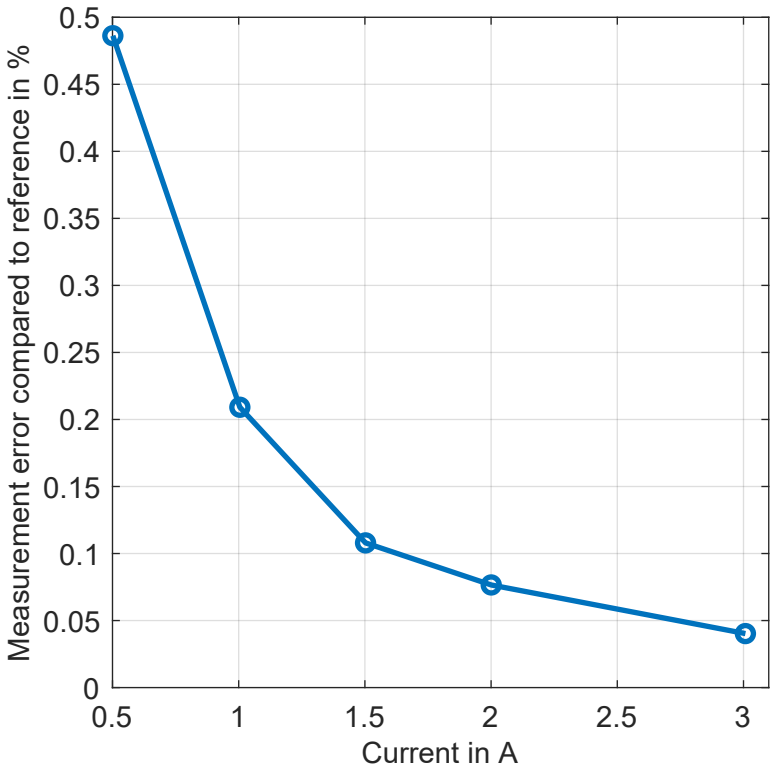

Figure 10.5: Error of current measurement

The current measurement is done via a shunt resistor of 0.01 Ω in series to the heater. The shunt resistor causes a voltage drop that is proportional to the current through the heater. The voltage drop across the shunt resistor is measured with

a parallel circuit and an NI 9219 module, programmed to voltage measurement with a range of ±15 V. The error of the current measurement is analyzed using a Keysight technologies U1280 Series multimeter as a reference sensor. The results are displayed in figure 10.5. The multimeter has an accuracy of ±0.05% ([67]). At a minimum current of 0.6 A in the experiments, the maximum error compared to the multimeter reading is 0.44%. Added to the fixed error of the multimeter of 0.05% this results in a maximum current error of 0.49% in the measurement range.

10.3 Aditional measurement results

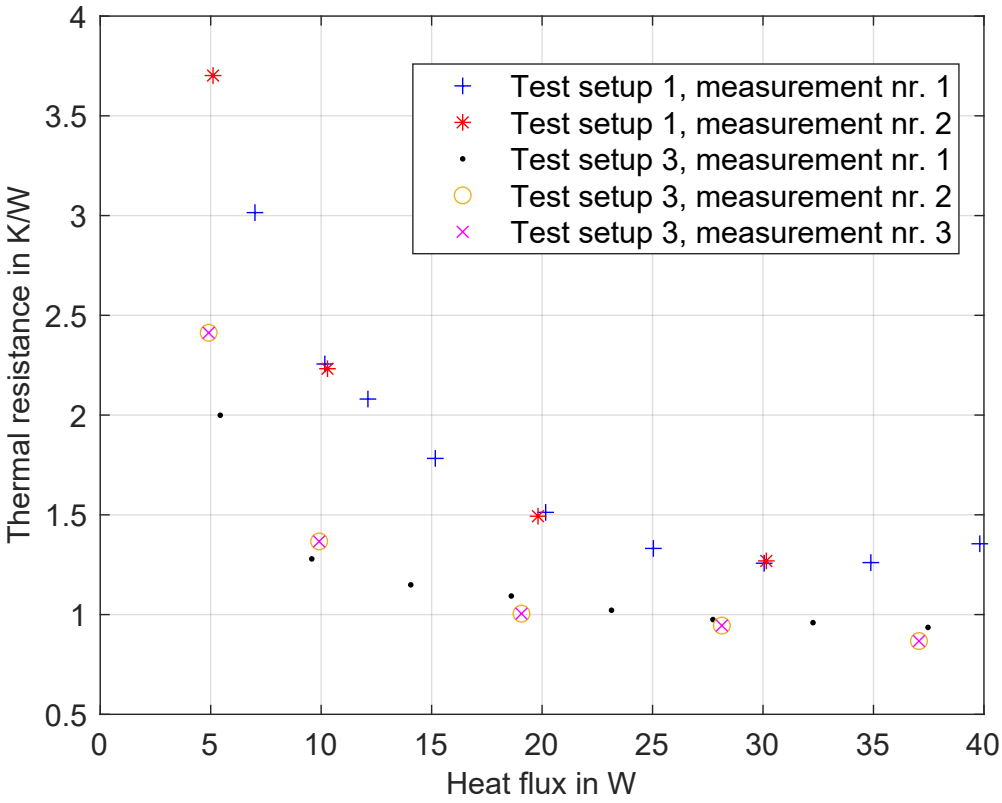

Figure 10.6: Thermal resistance repeatability for test setup 1 and 3 at 70% filling ratio and 20◦C condenser temperature

10.4 Setup of numerical simulations

Parameter	Unit	Value
Channel type		rectangular
Channel height	mm	1
Channel width	mm	1
Wall thickness	mm	0.5
Wall material		Aluminum pure
Wall roughness		According to boundary conditions
Evaporator length	mm	10
Condenser length	mm	100
Adiabatic length	mm	60
Condenser loop	mm	6
Turn width	mm	2
Adiabatic evaporator turns		yes
Adiabatic condenser turns		yes
Fluid type		R1233zdE
Pitch		Vertical
Roll	°	0
Yaw	°	0
Filling ratio		According to boundary conditions
Condenser temperature	°C	According to boundary conditions
Ambient temperature	°C	20
Initial temperature	°C	Equal to condenser temperature
Heated/cooled channel fraction		0.75
FFM Straight parts		1
FFM Turns parts		3
Constant heat rate	W	According to boundary conditions
External resistance condensor part	mK/W	0.3
External resistance evaporator part	mK/W	0
External resistance adiabatic part	mK/W	10000
Simulation time	s	100
Courant number		0.1
Writing interval	s	0.1
Element size	mm	1

Table 10.1: Overview on simulation parameters

10.5 Liquid mass fractions

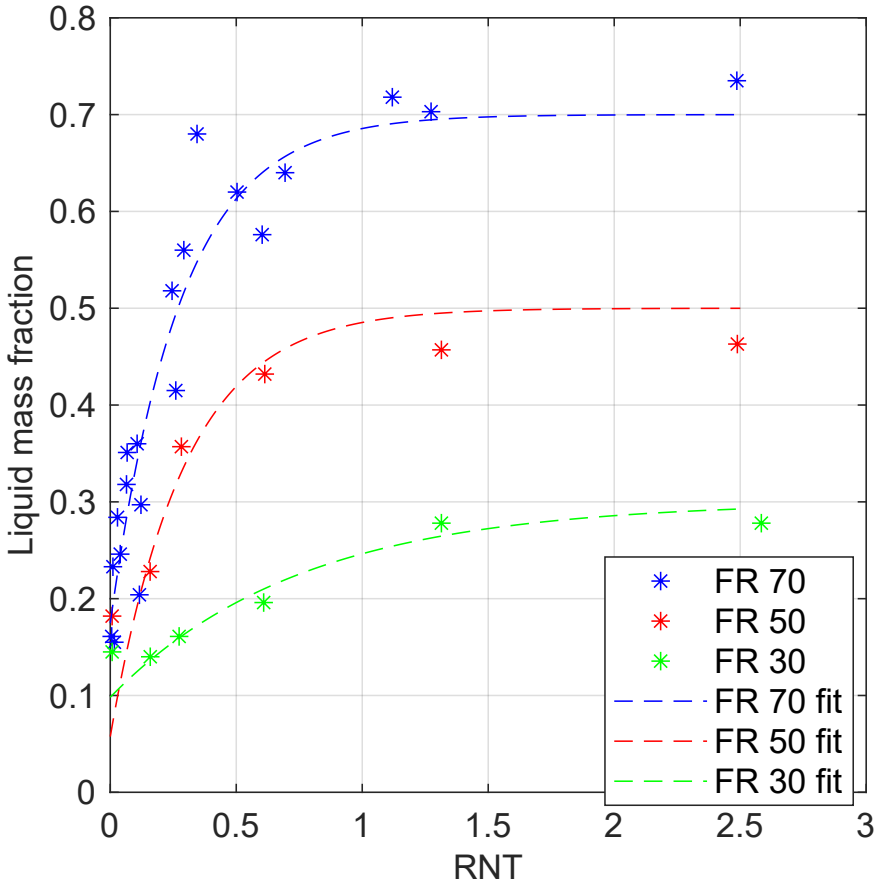

Figure 10.7: Liquid mass fractions in simulations with different filling ratios with respect to relative nucleation threshold

10.6 Technical drawings

Technical drawing located on next page

Figure 10.8: Baseplate: complete technical drawings

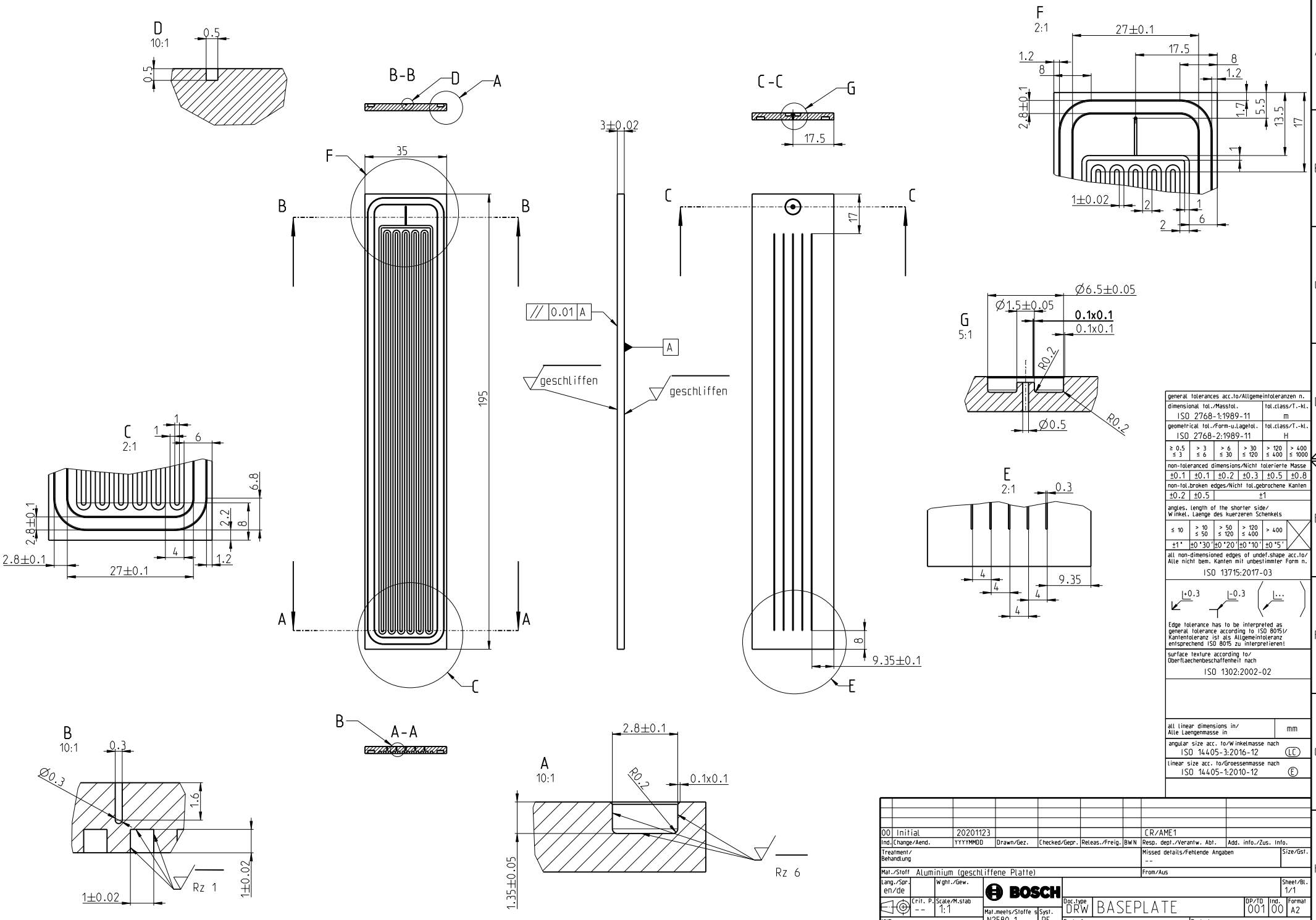

general tolerances acc.to/Allgemeintoleranzen n.	
dimensional tol./Masstol. ISO 2768-1:1989-11	tol.class/T.-kl. m
geometrical tol./Form-u.Lagetol. ISO 2768-2:1989-11	tol.class/T.-kl. H

≥ 0.5 ≤ 3	> 3 ≤ 6	> 6 ≤ 30	> 30 ≤ 120	> 120 ≤ 400	> 400 ≤ 1000
non-toleranced dimensions/Nicht tolerierte Masse					
±0.1	±0.1	±0.2	±0.3	±0.5	±0.8
non-tol.broken edges/Nicht tol.gebrochene Kanten					
±0.2	±0.5	±1			

angles, length of the shorter side/ Winkel, Laenge des kuerzeren Schenkels

≤ 10	> 10 ≤ 50	> 50 ≤ 120	> 120 ≤ 400	> 400
±1°	±0°30'	±0°20'	±0°10'	±0°5'

all non-dimensioned edges of undef.shape acc.to/ Alle nicht bem. Kanten mit unbestimmter Form n. ISO 13715:2017-03

Edge tolerance has to be interpreted as general tolerance according to ISO 8015/ Kantentoleranz ist als Allgemeintoleranz entsprechend ISO 8015 zu interpretieren!

surface texture according to/ Oberflaechenbeschaffenheit nach ISO 1302:2002-02

all linear dimensions in/ Alle Laengenmasse in: mm

angular size acc. to/Winkelmasse nach ISO 14405-3:2016-12 (LC)

linear size acc. to/Groessenmasse nach ISO 14405-1:2010-12 (E)

Ind.	Change/Aend.	YYYYMMDD	Drawn/Gez.	Checked/Gepr.	Releas./Freig.	BWN	Resp. dept./Verantw. Abt.	Add. info./Zus. Info.
00	Initial	20201123					CR/AME1	

Treatment/ Behandlung

Missed details/Fehlende Angaben: --

Size/Gst.

Mat./Stoff: Aluminium (geschliffene Platte)

From/Aus

Lang./Spr.: en/de

Wght./Gew.

Crit. P.: --

Scale/M.stab: 1:1

Mat.meets/Stoffe s: N2580-1

Syst.: PE

Sheet/Bl.: 1/1

Doc.type: DRW

BASEPLATE

DP/TD: 001

Ind.: 00

Format: A2

MNR

Repl. for

Repl. by